Coherent frequency conversion towards ultrashort VUV pulses enhanced by dressed states and adiabatic quantum dynamics

Cipura, Fabian

(2020)

Coherent frequency conversion towards ultrashort VUV pulses enhanced by dressed states and adiabatic quantum dynamics

Kohärente Frequenzkonversion von ultrakurzen Laserpulsen in den VUV Spektralbereich, überhöht durch adiabatische Quantendynamik

Dissertation von Fabian Cipura, Juni 2020

TECHNISCHE UNIVERSITÄT DARMSTADT

Fachbereich Physik
Institut für Angewandte Physik
Nichtlineare Optik
und Quantenoptik

Coherent frequency conversion towards ultrashort VUV pulses enhanced by dressed states and adiabatic quantum dynamics

Dem Fachbereich Physik

der Technischen Universität Darmstadt

zur Erlangung des Grades

eines Doktors der Naturwissenschaften (Dr. rer. nat.)

genehmigte Dissertation von

M.Sc. Fabian Cipura

aus Hamburg

Referent: Prof. Dr. Thomas Halfmann

Korreferent: Prof. Dr. Thomas Walther

Tag der Einreichung: 15.06.2020

Tag der Prüfung: 20.07.2020

Darmstadt 2020

D17

Cipura, Fabian:
Coherent frequency conversion towards ultrashort VUV pulses enhanced by dressed states and adiabatic quantum dynamics
Darmstadt, Technische Universität Darmstadt,
Jahr der Veröffentlichung der Dissertation auf TUprints: 2020
Tag der mündlichen Prüfung: 20.07.2020

„Ein Gelehrter in einem Laboratorium ist nicht nur ein Techniker, er steht auch vor den Naturvorgängen wie ein Kind vor einer Märchenwelt.“ – Marie Curie

Contents

Introduction

The generation of vacuum-ultraviolet (VUV) radiation is of interest for many applications, which exploit, e.g., the short wavelength ($10 - 200$ nm) of the VUV radiation for imaging and lithography [1–3], the high frequency for generating ultrashort pulses down to tens of attoseconds [3,4] and the high photon energy for spectroscopy [3,5–9]. Depending on the application, different sources of VUV radiation are suitable, such as, e.g., synchrotrons [6,8,9], free electron lasers [10,11], VUV lasers [2], discharge lamps [6], laser plasma [1], or coherent radiation in the visible regime converted by nonlinear optical processes [5,6,12,13]. In the following work, we investigate for nonlinear optical frequency conversion of ultrashort laser pulses (picoseconds, ps) at high intensities (TW/cm²) methods of resonance enhancement and coherently-driven quantum systems to increase the VUV yield. Thereby we investigate the applicability of coherent light-matter interactions and adiabatic quantum dynamics at high intensities.

Nonlinear optical frequency conversion: Nonlinear optical frequency conversion is a powerful tool to increase the accessible spectral range of laser radiation, which is limited, e.g., by the availability of appropriate media [13–15]. Nonlinear optics provides access to the spectrum from soft X-rays to mid-infrared and enables tuning of the frequency in large intervals. Particularly in the ultraviolet, visible and infrared spectral regime, there are commercial systems based on frequency conversion in nonlinear optical crystals available. However, aiming at frequencies in the VUV spectral regime, crystals suffer from absorption. Hence, other nonlinear materials such as gases are utilized to generate VUV radiation, e.g., rare gases due to their high ionization threshold. While rare gases offer high transparency in the VUV, the nonlinear susceptibilities and, hence, conversion efficiencies are naturally much smaller compared to crystals. Enhancements of the nonlinear susceptibility via atomic resonances (e.g., by tuning the laser to a multi-photon resonance) are a straightforward approach to improve conversion efficiencies. The conversion efficiency of a nonlinear optical process is dependent on the nonlinear optical susceptibility, laser intensity, interaction length and phase matching. In this work, we investigate for a high intensity (TW/cm²) and a short fixed interaction length (gas jet), how the nonlinear susceptibility and the frequency conversion efficiency can be increased via atomic resonances and adiabatic quantum dynamics.

Adiabatic quantum dynamics applied to nonlinear optics: Adiabatic quantum dynamics rely on coherent light-matter interaction, which modifies the "bare" eigenstates of a quantum system to "dressed" states and exploits slow (i.e., adiabatic) population evolutions via such dressed states. This also enables enhancement of low-order, low-intensity nonlinear optics (at MW/cm², GW/cm²), where the light field perturbs the atomic level structure only weakly [16–18]. On the other hand, aiming at nonlinear optics at higher orders, e.g., high-harmonic generation [19], strong light fields are applied (100 TW/cm², PW/cm²). These modify the Coulomb potential of the atom strongly and change the atomic level structure, which may lead to a suppression of resonance enhancement. The strength of light-matter interaction can be determined, e.g., by the Keldysh parameter $\gamma = \sqrt{W_I/2\phi}$ [20,21],

which is depending on the ratio of the ionization potential W_I of the interaction medium ($W_I = 12.1$ eV to 24.6 eV for rare gases, xenon to helium) and the ponderomotive energy ϕ, i.e., the quivering (kinetic) energy of a free electron in an ac electric field (proportional to the driving laser intensity). For low intensities (MW/cm², GW/cm²), the ionization potential dominates the ponderomotive energy, hence, we obtain a Keldysh parameter $\gamma \gg 1$. This is the regime of perturbative nonlinear optics and multi-photon effects, such as multi-photon ionization. The atomic level structure is only weakly perturbed. For very high intensities (PW/cm²), the ponderomotive energy is larger than the ionization potential, yielding $\gamma \ll 1$. Thus, the Coulomb potential of the atom is strongly perturbed and tunnel ionization dominates. In this case, resonances play no role anymore and adiabatic quantum dynamics via atomic resonances will not work.

We aim now at the implementation of adiabatic quantum dynamics for nonlinear optics in an intermediate intensity regime (TW/cm²), i.e., at Keldysh parameters approaching $\gamma \approx 1$. The fundamental question is, whether the already large intensities in this regime still permit us to drive and exploit coherent-adiabatic dynamics via dressed states for enhancement of frequency conversion efficiencies. Previous experiments already demonstrated resonance enhancements up to intensities of $I = 60$ TW/cm² in argon corresponding to a Keldysh parameter of $\gamma \approx 2$ [22,23]. Further, adiabatic quantum dynamics (coherent control) were successfully implemented up to an intensity of $I = 1.4$ TW/cm² [24] and down to a Keldysh parameter of $\gamma \approx 3$ [25]. In this work, we transfer techniques of adiabatic quantum dynamics (dressed states and coherent population return) towards high intensities, where the Keldysh parameter approaches $\gamma \approx 1$. We implement our experiments with (ps) laser pulses, which combine sufficiently high intensities up to several TW/cm², with still moderate bandwidth in the range of $\delta\omega_P/2\pi = 1$ THz to selectively address atomic resonances. The pulse durations (or bandwidths) and intensities are between the regime of ultra-short (fs) pulses, which are typically applied for higher-order nonlinear optics, and longer (ns, μs) laser pulses, which are typically applied for coherent-adiabatic interactions. With the intense, but still sufficiently narrowband (ps) pulses we aim at implementations of adiabatic quantum dynamics at higher intensities and, potentially, higher-order frequency conversion.

Resonantly enhanced harmonic generation via dressed states with large Autler-Townes splittings: In a first set of experiments, we investigate harmonic generation of pump laser pulses, enhanced by preparation of dressed states. A control laser, with appropriately matched frequency and/or peak intensity serves to generate dressed states with large, tunable Autler–Townes splittings [26] in the THz range. The energetic position of the dressed states is laser-controlled to match multiple pump laser photons. This enables resonance enhancement of harmonic generation also for typically utilized fixed-frequency and off-resonant pump laser pulses. Autler-Townes splittings for frequency conversion already attracted attention before, but the aim of early work [27] was to explain some features of rather low-intensity VUV generation [28] by improved phase matching conditions between dressed states. Recent theory work gave some evidence for the role of dressed states in high-harmonic generation also in the strong field regime [29]. Other related work

exploited dressed states to drive electromagnetically-induced transparency (EIT), i.e., to suppress linear re-absorption of VUV radiation between dressed states [17,30–32]. In our work, we aim at preparation of dressed states with large tunability of their energetic position and resonantly enhanced harmonic generation via these laser controlled states. In particular, we focus at applications in the regime of high intensities (TW/cm²), large Autler-Townes splittings of many THz, and higher-order frequency conversion processes. We also show how to compensate or exploit the unavoidable large ac Stark shifts, which occur in this intensity regime. We provide convincing experimental data to demonstrate the concept in argon and xenon, yielding enhancements of harmonic generation by 1-2 orders of magnitude.

Frequency conversion enhanced by coherent population return: In a second set of experiments, we demonstrate frequency conversion, enhanced by coherent population return and preparation of maximal atomic coherences at high intensities (TW/cm²). We generate the sum frequency of an intense pump pulse and a probe pulse via a two-photon resonance in xenon. When we slightly detune the pump laser from two-photon resonance, the atomic populations are adiabatically driven forth and back from the atomic ground state to an excited state. This coherent population return (CPR) prepares the medium in a transient state of maximal atomic coherence, which enhances frequency mixing with a probe laser. There are several approaches towards temporally stable and maximal coherence for frequency conversion, e.g., EIT [17,30–32], Stark-chirped rapid adiabatic passage (SCRAP) [16,33] or coherent population return (CPR) [16,18]. These techniques aim at adiabatic light-matter interaction rather than diabatic interaction, which inevitably leads to Rabi oscillations. While EIT and SCRAP require two pump fields, CPR exploits adiabatic dynamics driven by a single laser field only. With our experiment on CPR, we demonstrate the applicability of methods of coherently prepared media also at high intensities.

The thesis is structured as follows: The first chapter describes the basics of frequency conversion via nonlinear optics, resonance enhancements and ac Stark shifts. Further, we discuss the basic theory of nonlinear optics in coherently-driven quantum systems. The second chapter presents the experimental setup, i.e., the (ps) laser system, the nonlinear optical medium and the detection setup. Chapter 3 discusses the experimental results on resonantly enhanced harmonic generation via dressed states with large Autler-Townes splittings. We demonstrate the concept in argon and xenon, yielding enhancements of harmonic generation by 1-2 orders of magnitude and yielding Autler-Townes splittings of up to 100 THz. Chapter 4 presents the investigations on coherent population return and delayed frequency conversion in the high intensity regime. We find that ac Stark shifts induce an asymmetry in the spectral characteristics of CPR, which nevertheless permits enhanced frequency conversion. For the case of resonantly enhanced frequency conversion we show, that the atomic coherences are maintained for several ten picoseconds after the pump pulse, which permits time-delayed frequency conversion. The findings of this work shall push applications of adiabatic light-matter interactions now also to the regime of nonlinear optics, driven by high intensity laser pulses.

1 Theory of frequency conversion in coherently driven media

This chapter gives a brief introduction into frequency conversion via nonlinear optics. Starting with the nonlinear wave equation, we see that the source of new frequency components is the nonlinear polarization of the interaction medium. Consequently, we show that atomic resonances can enhance the nonlinear polarization by orders of magnitude. However, inevitable ac Stark shifts reduce the resonance enhancement of frequency conversion in the high-intensity regime by dynamically changing the transition frequency. For the description of strong couplings and coherent quantum dynamics, we express the macroscopic polarization by the microscopic polarization of each atom (via the quantum mechanical expectation value of the dipole moment). This enables calculations of nonlinear optics in coherently-driven quantum systems, showing coherent effects like Autler-Townes splittings (see chapter 3) and coherent population return (see chapter 4).

Please note, that this chapter is just a brief introduction in the theory needed for the discussion of the experiments of this work. A more general treatment can be found in textbooks of, e.g., Boyd [14], Reintjes [13] or Shore [34,35].

1.1 Nonlinear wave equation – frequency conversion

The electromagnetic wave equation describes the propagation of light (electromagnetic radiation) through a medium or vacuum, and is derived from Maxwell´s equations. In order to generate new frequency components, the interaction with the medium, i.e., the induced polarization, has to be nonlinear and thus we obtain the nonlinear wave equation. For our discussions we consider the light field moving in z-direction as the time dependent electric field $E_\omega(z,t) = E_{0,\omega}(z)/2 \cdot e^{i(\omega t - kz)} + c.c.$, with the amplitude of the electric field E_0, the angular frequency ω and the wave vector k. Hence, we assume plane-waves for our calculation. We neglect the magnetic field, as its force on electrons is much smaller for intensities well below $I = 10^{17}$ W/cm².

We start with the wave equation for electromagnetic radiation assuming no free charges and currents in scalar form, as we are dealing with isotropic media (gas atoms):

$$\Delta E(z,t) - \frac{1}{c^2}\frac{\partial^2}{\partial t^2}E(z,t) = \mu_0 \frac{\partial^2}{\partial t^2}P(z,t) \tag{1.1}$$

with speed of light c, vacuum permeability μ_0 and polarization P. In linear optics, the polarization is given by $P = P^{(L)} = \varepsilon_0 \chi^{(1)} E$ with the vacuum permittivity ε_0 and linear susceptibility $\chi^{(1)}$. However, to describe the light-matter interaction correctly and to describe nonlinear interactions we need a nonlinear polarization $P^{(NL)}$. A simple, didactical expression is given by a Taylor series ansatz [14][1]:

$$P = \varepsilon_0 \cdot \left(\chi^{(1)}E + \chi^{(2)}E^2 + \chi^{(3)}E^3 + \cdots\right) = P^{(L)} + P^{(NL)} \tag{1.2}$$

[1] Note that in general, e.g., the second order polarization is given by: $P_i^{(2)}(\omega_3) = \varepsilon_0 \sum_{jk}\sum_{nm}\chi^{(2)}(\omega_3,\omega_n,\omega_m)E_j(\omega_n)E_k(\omega_m)$ with the Cartesian coordinates ijk and the sum over all frequencies ω_n, ω_m.

with the higher-order susceptibilities $\chi^{(2)}$ (second order) and $\chi^{(3)}$ (third order). Here, we neglected the frequency dependence of the susceptibilities for simplicity (compare subsection 1.2). We obtain the nonlinear wave equation:

$$\Delta E(z,t) - \frac{n^2}{c^2}\frac{\partial^2}{\partial t^2}E(z,t) = \mu_0 \frac{\partial^2}{\partial t^2}P^{(NL)}(z,t) \tag{1.3}$$

with the refractive index n ($n^2 = 1 + \chi^{(1)}$). The induced nonlinear polarization is the source of new frequency components. Note that for centrosymmetric media like rare gases only odd orders of the nonlinear susceptibility do not vanish. Hence, we observe odd order processes (like THG), but no even order processes like second-harmonic generation (SHG) in rare gases. For example, we discuss now the nonlinear process of third-harmonic generation (THG). All other processes, e.g., higher-order harmonic generation or sum/difference frequency generation, can be treated in an analogue way and can be found in textbooks [13,14].

The electric field of the third-harmonic $E_{3\omega}$ is generated (mainly) by the part of the third order polarization which is oscillating at frequency 3ω:

$$P_{3\omega}^{(3)}(z,t) = \varepsilon_0 \chi^{(3)} E_\omega^3 = \varepsilon_0 \chi^{(3)} \left(\frac{E_{0,\omega}^3}{2} \cdot e^{i(3\omega t - 3k_\omega z)} + c.c. \right) \tag{1.4}$$

First, we simplify the nonlinear wave equation by just taking into account the components oscillating at frequency 3ω:

$$\Delta E_{3\omega}(z,t) - \frac{n_{3\omega}^2}{c^2}\frac{\partial^2}{\partial t^2}E_{3\omega}(z,t) = \mu_0 \frac{\partial^2}{\partial t^2}P_{3\omega}^{(3)}(z,t) \tag{1.5}$$

with the index of refraction of the third-harmonic $n_{3\omega}$. Then, we apply the slowly-varying envelope approximation (SVEA) [14], obtaining a first order differential equation:

$$\frac{\partial}{\partial z}E_{0,3\omega}(\mathrm{z}) = i\frac{3\omega}{2c\varepsilon_0 n_{3\omega}}\varepsilon_0 \chi^{(3)} E_{0,\omega}^3 e^{i\Delta k z} \tag{1.6}$$

with the wave vector mismatch $\Delta k = (k_{3\omega} - 3k_\omega)$. For the main experiments in this work, we utilized a gas jet of rare gas atoms as interaction medium (interaction length in the range of $L \approx 1$ mm, particle density in the range of $N = 10^{17}$ cm^{-3}). Hence, calculations yield that the phase mismatch remains small, i.e., $\Delta k L \ll 1$ and we can neglect the phase matching term. Finally, we get a simple differential equation for the calculation of the electric field of the third-harmonic:

$$\frac{\partial}{\partial z}E_{0,3\omega}(\mathrm{z}) = i\frac{3\omega\chi^{(3)}E_{0,\omega}^3}{2cn_{3\omega}} = i\frac{3\omega}{2c\varepsilon_0 n_{3\omega}}P_{0,3\omega}^{(3)} \tag{1.7}$$

We integrate the equation over the interaction length L and get for the THG intensity:

$$I_{3\omega} \sim \left(\chi^{(3)} L\right)^2 I_\omega^3 \tag{1.8}$$

This equation reveals three possibilities for enhancing frequency conversion processes: High nonlinear susceptibilities, long interaction length (caution: phase mis-

match) and high intensities. This work deals with enhancements of nonlinear susceptibilities via atomic resonances at high intensities (see following section and chapter 3). Further, we show that for strong couplings the Taylor series ansatz for the polarization collapses and we have to express the macroscopic polarization via the microscopic polarization for each atom (section 1.3 and chapter 4).

1.2 Resonance enhancement

The efficiency of frequency conversion in rare gases suffers from low nonlinear susceptibilities. Hence, it is a straightforward approach to exploit atomic resonances to enhance these. For simplicity, we continue with our example of THG and estimate resonance enhancements and its reduction by ac Stark shifts.

The level scheme for THG is depicted in Fig. 1.1. The detunings are defined as $\Delta_{12}^{(1p)} = \omega - \omega_{12}$, $\Delta_{13}^{(2p)} = 2\omega - \omega_{13}$, $\Delta_{14}^{(3p)} = 3\omega - \omega_{14}$ with the transition frequencies ω_{ij}. The superscript $1p, 2p, 3p$ describes, whether it is a one-, two- or three-photon detuning. Note that using atomic resonances (vanishing detunings) requires (widely) tunable lasers to match the laser frequency ω to the atomic resonance frequency ω_{ij}. There are three choices for resonant THG, i.e., via state $|2\rangle$, $|3\rangle$ or $|4\rangle$. A two-photon resonance $\Delta_{13}^{(2p)} = 0$ is superior, because for the one- and three-photon resonance ($\Delta_{12}^{(1p)} = 0, \Delta_{14}^{(3p)} = 0$) absorption of either the pump or THG perturbs frequency conversion. Further, phase matching becomes more challenging for the latter cases. However, we discuss now the resonance enhancement via a three-photon resonance ($\Delta_{14}^{(3p)} \ll \Delta_{12}^{(1p)}, \Delta_{13}^{(2p)}$), because we have the latter case in chapter 3.

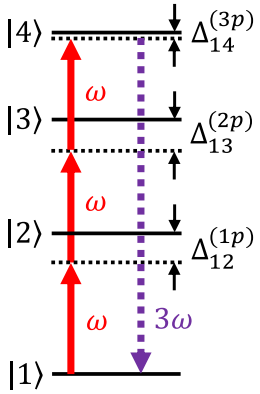

Figure 1.1: Coupling scheme for THG.

The nonlinear susceptibility can be calculated using the density matrix approach and yields (we only consider the path shown in Fig. 1.1, the usually appearing permutations vanish, because we have only one driving field) [14]:

$$\chi^{(3)}(\omega) = \frac{N\mu_{12}\mu_{23}\mu_{34}\mu_{14}}{\varepsilon_0\hbar^3\left(\Delta_{12}^{(1p)} - i\gamma_2\right)\left(\Delta_{13}^{(2p)} - i\gamma_3\right)\left(\Delta_{14}^{(3p)} - i\gamma_4\right)} \tag{1.9}$$

with the number density N, the transition dipole moments μ_{ij} and damping constants γ_i. Assuming large one- and two-photon detunings ($\Delta_{12}^{(1p)} \gg \gamma_2, \Delta_{13}^{(2p)} \gg \gamma_3$), we can simplify the expression to:

$$\chi^{(3)}(\omega) \approx \frac{N\mu_{12}\mu_{23}\mu_{34}\mu_{14}}{\varepsilon_0\hbar^3\Delta_{12}^{(1p)}\Delta_{13}^{(2p)}\left(\Delta_{14}^{(3p)} - i\gamma_4\right)} \tag{1.10}$$

Now, we are just interested in the resonance enhancement. Therefore, we neglect all constants and almost constant detunings and get:

$$\chi^{(3)}(\omega) \sim \frac{1}{\Delta_{14}^{(3p)} - i\gamma_4} \tag{1.11}$$

In our experiments, we deal with laser pulses in the picosecond domain, with typical pulse energies of $E_P = 10\,\mu$J to 1 mJ and intensities of TW/cm². We apply pulses with wavelength from the UV to the near-infrared, with a bandwidth of roughly $\delta\omega_p/2\pi \approx 1$ THz, which is larger than the Doppler broadening of the interaction medium (rare gas) with roughly 1 GHz. Thus, the minimal effective three-photon detuning is limited by the laser pulse bandwidth and we can neglect the damping constant γ_4. We obtain for the nonlinear susceptibility $\chi^{(3)}(\omega) \sim 1/\delta\omega_P$. Consequently, for a typical off-resonant detuning of $\Delta_{14}^{(3p)}/2\pi = 100$ THz the nonlinear susceptibility can be enhanced by $\Delta_{14}^{(3p)}/\delta\omega_P = 100$ [36]. The generated frequency conversion intensity depends quadratically on the nonlinear susceptibility (eqn. 1.8), hence, we obtain a substantial enhancement of 10^4. Comparing that to an increase of the pump intensity, e.g., for a third-harmonic ($I_{3\omega} \sim I_\omega^3$), this corresponds to a 20-times higher intensity. This increase of intensity usually increases the experimental effort and costs drastically. The enhancement of the nonlinear susceptibility for THG effects other frequency conversion channels as well, which are using the same three-photon resonance. An example, which we will observe in chapter 3, is the fifth-harmonic generation.

1.2.1 ac Stark shift and ponderomotive potential

The above discussion of resonance enhancements of nonlinear susceptibilities neglected atomic level shifts, which can strongly reduce the possible enhancement. For the experimental parameters in this work, the ac Stark shift is the dominant atomic level shift (in comparison to, e.g., Zeeman shift). The ac Stark shift is a level shift caused by an oscillating electric field (here the light field). In the low intensity regime, the ac Stark shift of level n can be calculated applying perturbation theory and yields [37–39]:

$$\Delta E_n = \frac{1}{4}\sum_m \left(\frac{\left|\vec{\mu}_{nm}\cdot\vec{E}_0\right|^2}{E_n - E_m - \hbar\omega} + \frac{\left|\vec{\mu}_{nm}\cdot\vec{E}_0\right|^2}{E_n - E_m + \hbar\omega} \right) \tag{1.12}$$

$$= \frac{1}{4}\sum_m \left(\frac{\left|\vec{\mu}_{nm}\cdot\vec{E}_0\right|^2}{\hbar\omega_{nm} - \hbar\omega} + \frac{\left|\vec{\mu}_{nm}\cdot\vec{E}_0\right|^2}{\hbar\omega_{nm} + \hbar\omega} \right) \tag{1.13}$$

with the reduced Planck`s constant $\hbar$, the sum over all levels m (except level n), the corresponding level energy E_m and transition frequency ω_{nm}. Although we sum over all atomic states, usually only one or a few near resonant levels dominate the level shift.

Let us now discuss the ac Stark shifts calculated from the above formula for our experimental parameters. For an intensity of $I = 1$ TW/cm², a typical dipole moment of $\mu = 10^{-29}$ Cm and a detuning $\omega_{nm} - \omega = \delta\omega_p = 2\pi \cdot 1$ THz we obtain an ac Stark shift of more than $\Delta E/h = 1000$ THz (with Planck`s constant h). This is above the light frequency and well above observed ac Stark shifts in experiments at TW/cm², which are in the range of some tens of terahertz [22]. In simple terms,

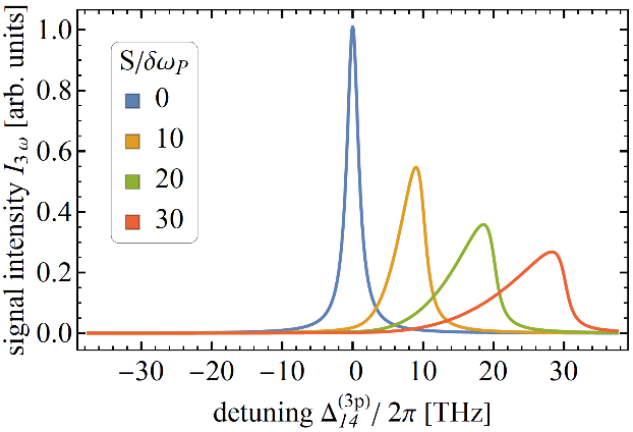

Figure 1.2: THG signal intensity versus three photon detuning for different ratios of ac Stark shift S to laser bandwidth ($\delta\omega_p/2\pi = 1$ THz). The simulation takes the temporal pulse shape into account, but neglects the transverse spatial profile.

the ac Stark shift model based on perturbation theory fails at high intensities and strong couplings. Hence, it is necessary to search for another approach, which applies for the high intensity regime.

For this work, we utilize the concept of the ponderomotive potential, which is the quivering energy of a free electron in an oscillating electric field. This was found to be a good rough estimation of the ac Stark shift of highly excited states, both theoretically [40] and experimentally [22,41,42], although it fully neglects the specific atomic level structure (see Appendix A). The ponderomotive potential is given by:

$$\phi(t) = \frac{e^2 E_0^2(t)}{4 m_e \omega^2} = \frac{e^2 E_0^2(t) \lambda_0^2}{16 \pi^2 m_e c^2} \equiv \hbar S(t) \sim I_P \lambda_0^2 \tag{1.14}$$

with elementary charge e, electron mass m_e, laser wavelength in vacuum λ_0 and ac Stark shift S. The ponderomotive potential is linearly dependent on the laser intensity, as the ac Stark shift from perturbation theory. Further, it has a quadratic dependency on the laser wavelength. For an intensity of $I = 1$ TW/cm² and a wavelength of $\lambda = 800$ nm (fundamental of a titanium-sapphire laser), we obtain a ponderomotive shift of $S/2\pi = 14.4$ THz. In comparison, the second-harmonic with a wavelength of 400 nm causes a four times smaller shift of $S/2\pi = 3.6$ THz. First, we see that choice of wavelength strongly effects the ponderomotive shift. Second, we see that the shift exceeds the bandwidth of a picosecond pulse ($\delta\omega_p/2\pi \approx 1$ THz) even for a still moderate intensity of $I = 1$ TW/cm².

Let us now discuss the effect of the ac Stark shift on the resonance enhancement in our example of THG. The THG intensity depends on the detuning plus the ac Stark shift:

$$I_{3\omega} \sim \frac{1}{\left(\Delta_{14}^{(3p)} + S(t)\right)^2 + (\delta\omega_P)^2} \tag{1.15}$$

First, this means that the resonance shifts to another frequency. If it is possible to tune the laser wavelength to the Stark shifted resonance, the resonance enhancement is not perturbed. Further, the ac Stark shift can change an atomic transition frequency such, that an originally detuned, fixed-frequency laser is tuned into resonance with the Stark shifted transition. In this case, the ac Stark shift can enhance the frequency conversion yield. However, as we are using pulses with a temporal

and spatial intensity dependence, the enhancement is reduced (see Fig. 1.2). For different intensities, we obtain different ac Stark shifts, which cause different resonance conditions and reduce the conversion efficiency. This effects the possible resonance enhancement depending on the specific temporal and spatial pulse shape. Consequently, the compensation of ac Stark shifts is a goal for resonantly enhanced harmonic generation in the high intensity regime, which we address in chapter 3.

1.3 Nonlinear optics in coherently-driven quantum systems

This section describes nonlinear optical effects via coherent light-matter interaction. The fundamental step is to express the macroscopic polarization via the microscopic polarization for each atom. This enables a full quantum mechanical treatment of the atom and gives rise to coherent effects and techniques, which we apply in this work to enhance and control light-matter interaction for nonlinear optics (see chapter 3 and 4). The light field will still be treated classically, as we are dealing with quite large photon numbers (as a rough estimation, we apply pulses with an energy of $E_p = 1\ \mu$J and a photon energy of $E_{ph} = 1$ eV. This yields a number of photons in the range of 10^{13}. Even for moderate frequency conversion efficiencies of 10^{-10} we expect 10^3 photons).

We start again with the nonlinear wave equation in SVEA (eqn. 1.7). For simplicity, we discuss again THG. The third order polarization for THG between ground state $|1\rangle$ and excited state $|4\rangle$ (for our level scheme in Fig. 1.1) can be calculated from the induced, microscopic dipole moment in the quantum system as:

$$P^{(3)}(t) = N\langle\hat{\mu}\rangle(t) = N\mu_{14}\rho_{14}(t) \tag{1.16}$$

with the expectation value of the electric dipole operator $\langle\hat{\mu}\rangle$, the transition dipole moment μ_{14} of the THG transition and the atomic coherence ρ_{14} between ground state $|1\rangle$ and excited state $|4\rangle$. The atomic coherence is defined as $\rho_{14} = c_1^* c_4$, with the probability amplitudes of the ground state $|1\rangle$ and the excited state $|4\rangle$ on the three-photon transition. Neglecting constant prefactors, and assuming small conversion efficiencies (i.e., undepleted pump field), we get now from the THG wave equation the simple relation:

$$\frac{\partial}{\partial z} E_{0,3\omega}(t) \sim N\rho_{14}(t) \tag{1.17}$$

After integration over a propagation distance L, we obtain for the THG intensity:

$$I_{3\omega}(t) \sim (NL)^2 |\rho_{14}(t)|^2 \tag{1.18}$$

Obviously, the THG intensity grows quadratically with the induced atomic coherence. Also, the temporal dependence of the generated field will follow the dynamics of the atomic coherence.

We calculate the coherence ρ_{14} by solving the Liouville-von Neumann equation:

$$\frac{\partial}{\partial t}\hat{\rho}(t) = \frac{i}{\hbar}\left[\hat{\rho}(t), \hat{\mathrm{H}}(t)\right] - \hat{\Gamma}(t) \tag{1.19}$$

with the density operator $\hat{\rho}$ and the Hamiltonian $\hat{\mathrm{H}}$. The loss operator $\hat{\Gamma}$ may include ionization losses of excited states, radiative population decay or dephasing processes.

The basic description of THG requires theoretical treatment in a four-level system (compare Fig. 1.1). Thus, the Hamiltonian in Dirac representation with dipole and rotating wave approximation reads [34]:

$$\hat{\mathrm{H}}(t) = \frac{\hbar}{2}\begin{pmatrix} 0 & \Omega_{12}(t) & 0 & 0 \\ \Omega_{12}^{*}(t) & 2\Delta_{12}^{(1p)} & \Omega_{23}(t) & 0 \\ 0 & \Omega_{23}^{*}(t) & 2\Delta_{23}^{(2p)} & \Omega_{34}(t) \\ 0 & 0 & \Omega_{34}^{*}(t) & 2\Delta_{34}^{(3p)} \end{pmatrix} \tag{1.20}$$

with the single-photon Rabi frequencies Ω_{ij}, which are given by $\Omega_{ij} = \mu_{ij}E_{0,\omega}/\hbar$. The Rabi frequency describes the frequency of population oscillations in a quantum system. Note, that in the Hamiltonian we have the resonant Rabi frequency, meanwhile we get for a detuning Δ faster population oscillations with the effective Rabi frequency $\overline{\Omega} = \sqrt{\Omega^2 + \Delta^2}$. The amplitude of the Rabi oscillations depends as well on the detuning and is given by:

$$A = \frac{\Omega^2}{\overline{\Omega}^2} = \frac{\Omega^2}{\Omega^2 + \Delta^2} \tag{1.21}$$

Let us now discuss how large the Rabi frequencies and the amplitude of the Rabi oscillations are for our experimental parameters and compare that to typical detunings. For an intensity of $I = 1$ TW/cm² ($E_{0,\omega} = 2.7 \cdot 10^9$ V/m) and a typical transition moment of $\mu = 10^{-29}$ Cm, we get a Rabi frequency of $\Omega/2\pi = 40$ THz. Hence, even for relatively far detuned resonances (e.g., $\Delta = 10$ THz), we expect large amplitudes of Rabi oscillations.

For a more general treatment and our experiments at high laser intensity, we add the time dependent ac Stark shift S to the detunings in the Hamiltonian. For the numerical simulations, we approximate the ac Stark shift S by the ponderomotive energy (compare subsection 1.2.1).

2 Experimental setup

The experimental setup contains three major parts: A laser system to generate the required laser pulses, an interaction chamber with an atomic gas jet of rare gas atoms as nonlinear optical medium, and a vacuum spectrometer for detection of radiation in the VUV spectral regime. In this chapter, we explain in general the experimental setup used for both experiments of this work (chapter 3 and 4). We describe specific changes, wavelengths and parameters in these chapters. More details on each part of the experimental setup can be found in the referenced thesis projects, as these are beyond the aim of this work.

2.1 Laser system and pulse generation

We implement our experiments with (ps) laser pulses. These combine sufficiently high intensities up to several TW/cm² to efficiently drive frequency conversion, with still moderate bandwidth in the range of $\delta\omega_P/2\pi = 1$ THz to selectively address atomic resonances. With our (ps) setup we aim at the regime between typical implementations of high-order nonlinear optics with broadband, ultrashort femtosecond (fs) pulses at very high intensities (100 TW/cm², PW/cm²) and typical implementations of nonlinear optics in coherently-driven quantum systems with narrowband, long (μs, ns) pulses at low intensities (MW/cm², GW/cm²).

For the experiments, we need two individual tunable laser pulses, e.g., pump and control/probe, with a peak intensity of roughly $I \approx 1$ TW/cm². These intensities enable Autler-Townes splittings in the range of several THz (larger than the laser bandwidth of roughly $\delta\omega_P/2\pi \approx 1$ THz) as we will see in chapter 3 and enable strong couplings on two-photon transitions, which are required for frequency conversion enhanced by coherent population return (chapter 4). Furthermore, such intensities are required to obtain sufficient signal levels for frequency conversion into the VUV spectral regime (with (ps) pulses in rare gases).

The laser system provides two individual widely tunable beamlines with (ps) laser pulses. The required intensities of about $I \approx 1$ TW/cm² are not directly achievable from lasers, so we implement a setup consisting of oscillators and following pulsed amplifiers. The basic setup is shown in Fig. 2.1 and is explained in the following subsections.

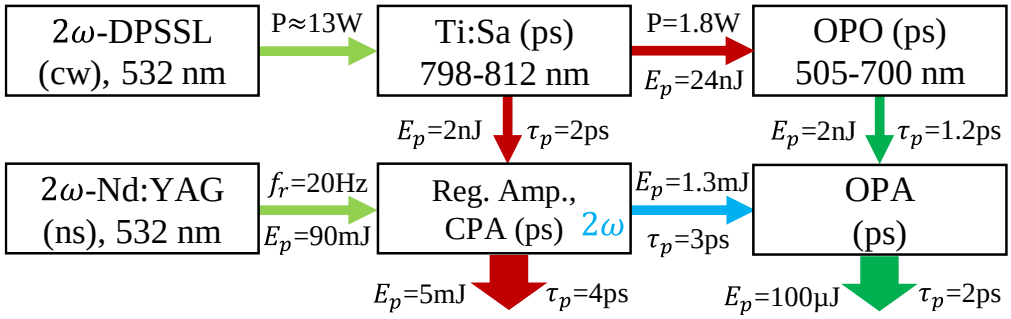

Figure 2.1: Schematic overview of the (ps) laser system. 2ω: second-harmonic; DPSSL: diode-pumped solid state laser; cw: continuous wave; Ti:Sa: titanium:sapphire oscillator; OPO: optical parametric oscillator; Reg. Amp.: regenerative amplifier; CPA: chirped pulse amplification; OPA: optical parametric amplifier; P: pump power; E_p: pulse energy; τ_p: pulse duration; f_r: repetition rate.

2.1.1 Titanium:sapphire oscillator and optical parametric amplifier

The (ps) laser pulses are generated in a commercial Kerr lens mode-locked Ti:Sa oscillator (Mira 900P, Coherent), pumped by a frequency-doubled diode pumped solid state laser (Finesse 14 W, Laser Quantum). The output pulses of the Ti:Sa have a pulse duration of $\tau_p = 1.4 - 2.1$ ps (full width at half maximum (FWHM), measured with a home-made autocorrelator [43]), depending on the settings of the group delay dispersion control (piezo voltage of a Gires-Tournois interferometer in the resonator). We reached the most stable operation for a pulse duration of $\tau_p = 2$ ps and applied that for all experiments. The bandwidth of the (ps) pulses is $\Delta\lambda = 0.3$ nm (FWHM, measured by a Czerny-Turner Spectrometer [44]), corresponding to a time bandwidth product of 0.3. This fits quite well to the Fourier limit of 0.315 for sech²-shaped pulses. The wavelength is tuned with a Lyot-Filter in the Ti:Sa oscillator. With the installed short wave optics set in the Ti:Sa oscillator the tuning range is between $\lambda = 710 - 812$ nm. Due to further installed optics behind the oscillator the tuning range is effectively limited to $\lambda = 760 - 812$ nm. The wavelength tunability of $\lambda = 798 - 812$ nm shown in Fig. 2.1 is restricted by the current stretcher/compressor setup of the regenerative amplifier. Mode-locking of the Ti:Sa oscillator is achieved without utilizing the internal aperture (typically applied for Kerr lens magic mode-locking). This allows us to obtain higher (average) output powers of about $P \approx 2$ W for continuous wave and mode-locked operation (typically $P = 1.8$ W with the aperture). This enables the maximal pump power of $P = 1.8$ W for the OPO with a residual seed energy for the regenerative amplifier in the range of $P = 0.2$ W. The repetition rate of the Ti:Sa oscillator is $f_r = 76$ MHz, corresponding to pulse energies of $E_p = 26$ nJ.

The modified commercial OPO (OPO FAN, APE Angewandte Physik & Elektronik GmbH) is a synchronously-pumped signal-resonant oscillator based on a periodically poled lithium niobate crystal (PPLN) with fan-out structure. The OPO generates intracavity the second-harmonic of the signal wave in a lithium triborate crystal (LBO). The SHG output is tunable between $\lambda = 505 - 740$ nm (505 – 700 nm utilized for this work) and has a power of $\bar{P} = 150$ mW corresponding to

a pulse energy of $E_p = 2$ nJ. The pulse duration of the second-harmonic is about 1.2 ps measured by an home-made autocorrelator [43]. The phase matching for the SHG is achieved by changing the crystal temperature between $T = 0$ °C to $T = 210$°C[1].

2.1.2 Regenerative amplifier

The residual pulse energy of the Ti:Sa oscillator not utilized for pumping the OPO is amplified in a regenerative amplifier (see Fig. 2.1). The pulse energy is increased from $E_p = 2$ nJ by a factor of roughly 10^6 to up to $E_p = 5$ mJ in a chirped pulse amplification system. The author developed and built the setup during the preceding master thesis [44] and finished the optimization and the characterization during this work. Setup and characterization will be subject of a publication in preparation.

The most commonly applied techniques for amplifying ultrashort pulses are chirped pulse amplification (CPA) [45,46] via stimulated emission and optical parametric CPA (OPCPA) [47–50] via nonlinear optics, both involving a pulse stretcher and compressor. These are typically implemented with surface gratings. However, for picosecond laser pulses, due to their small bandwidth compared to femtosecond laser pulses, we require a very high dispersion. In setups with surface gratings, this leads to large dimensions of the stretcher/compressor. Chirped fiber Bragg grating based setups offer in principle an alternative, but due to their rather small mode volume the recompressed pulse energy is strongly limited. In recent years another alternative, chirped volume Bragg gratings (CVBG), became commercially available for multiple wavelengths and bandwidths [51]. A CVBG can be understood as either a long chirped mirror or a large aperture fiber Bragg grating. There are several recent reports on implementations of amplifiers based on CVBGs, either in single-pass or double-pass configuration [52–55]. According to our knowledge, no wavelength tunable system has been implemented yet. In the following, we describe and characterize our compact, tunable CVBG based regenerative amplifier for (ps) laser pulses.

Figure 2.2 shows the ring regenerative amplifier with two curved mirrors (Laseroptik, radius of curvature $R = -3$ m) and a total cavity length of three meters. A Pockels cell (QX-1020, Gooch & Housego, KD*P) with a fast switching differential driver (ds11b, BME, 3.5 ns rise/fall time) allows 29 passes through the amplifier. The gain medium is a Ti:Sa crystal, as it naturally supports the full tuning range of the Ti:Sa oscillator. The single pass small signal gain is roughly two. The pump source of the amplifier is a frequency doubled Nd:YAG laser (Pro Lab 230, Spectra Physics) with a repetition rate of $f_r = 20$ Hz[2]. The total pump energy for the regenerative amplifier of $E_{pump} = 90$ mJ is divided in two pump arms. The

[1] Note that for temperatures below 20°C purging by dry air or nitrogen is necessary to prevent condensation on the LBO crystal. To achieve phase matching around 640 nm with a temperature of 0°C the alignment of the LBO is critical and might be adjusted in order to obtain the maximal SHG power. The LBO crystal is cooled with a Peltier element, which has to be moved by hand to the crystal holder (malfunction of the automation).

[2] We operated the pump laser without injection seeding, as we suffered from abruptly higher pulse energies, when the injection seeding failed.

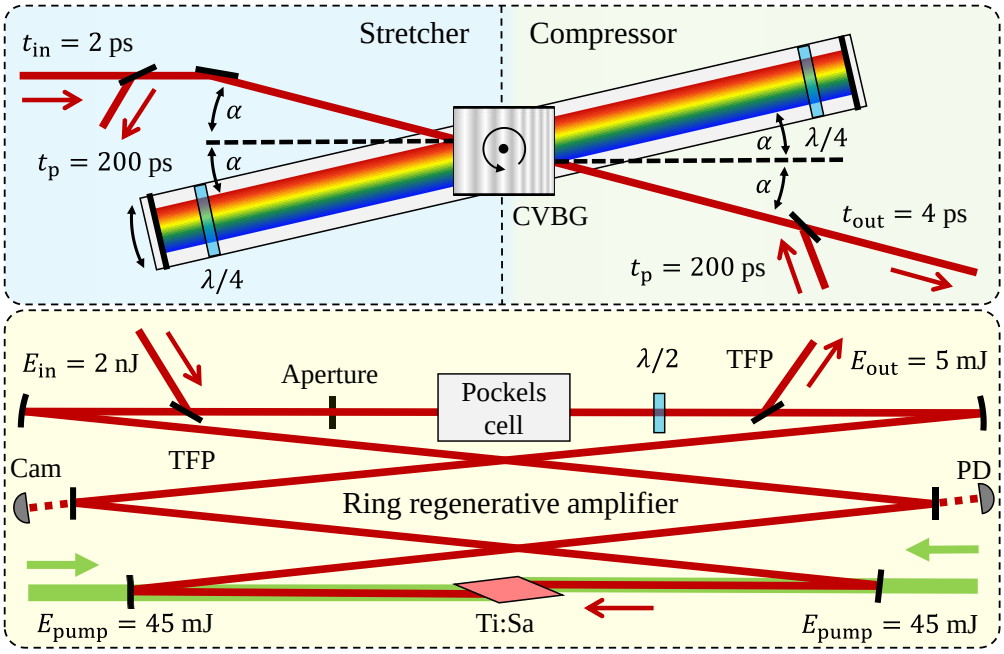

Figure 2.2: Experimental setup for the stretcher, the ring regenerative amplifier and the compressor. $\lambda/4$: quarter-wave plate; $\lambda/2$: half-wave plate; TFP: thin-film polarizer, PD: photodiode, Cam: camera.

pump beam diameter at the Ti:Sa crystal is $d = 2$ mm (FWHM), with a super Gaussian beam profile. Note that we apply only about 20 % of the $E_{pump} = 500$ mJ output energy of the frequency doubled Nd:YAG laser. So, from this perspective a power amplifier aiming at (ps) laser pulse energies up to $E_p = 100$ mJ is possible.

The tunable stretcher/compressor uses a CVBG (OptiGrate, size: 6.4 x 12 x 35 mm, anti-reflection coated) in double-pass configuration (Fig. 2.3 a). We have two different CVBGs, to cover the tuning range from $\lambda = 798 - 805$ nm (CBG-805-90-M) and from $\lambda = 805 - 812$ nm (CBG-812-90-M). A CVBG enables continuously tuning of the diffracted wavelengths by changing the incidence angle

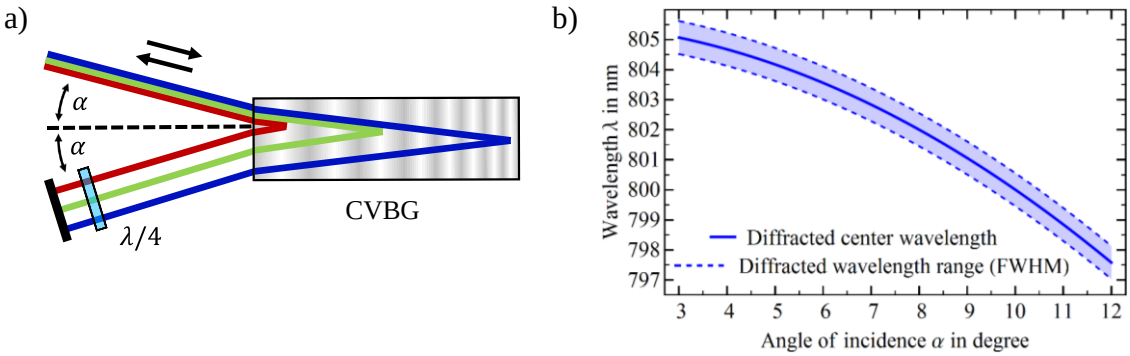

Figure 2.3: a) Sketch of the double-pass configuration for the CVBG based stretcher. Red spectral components are diffracted in the front section of the CVBG, green spectral components in the middle and blue spectral components in the back section of the CVBG thereby inducing a temporal chirp. b) Calculated tuning curve for the wavelength over the incident angle (for CBG-805-90-M). The shaded area shows the diffracted wavelength range (FWHM).

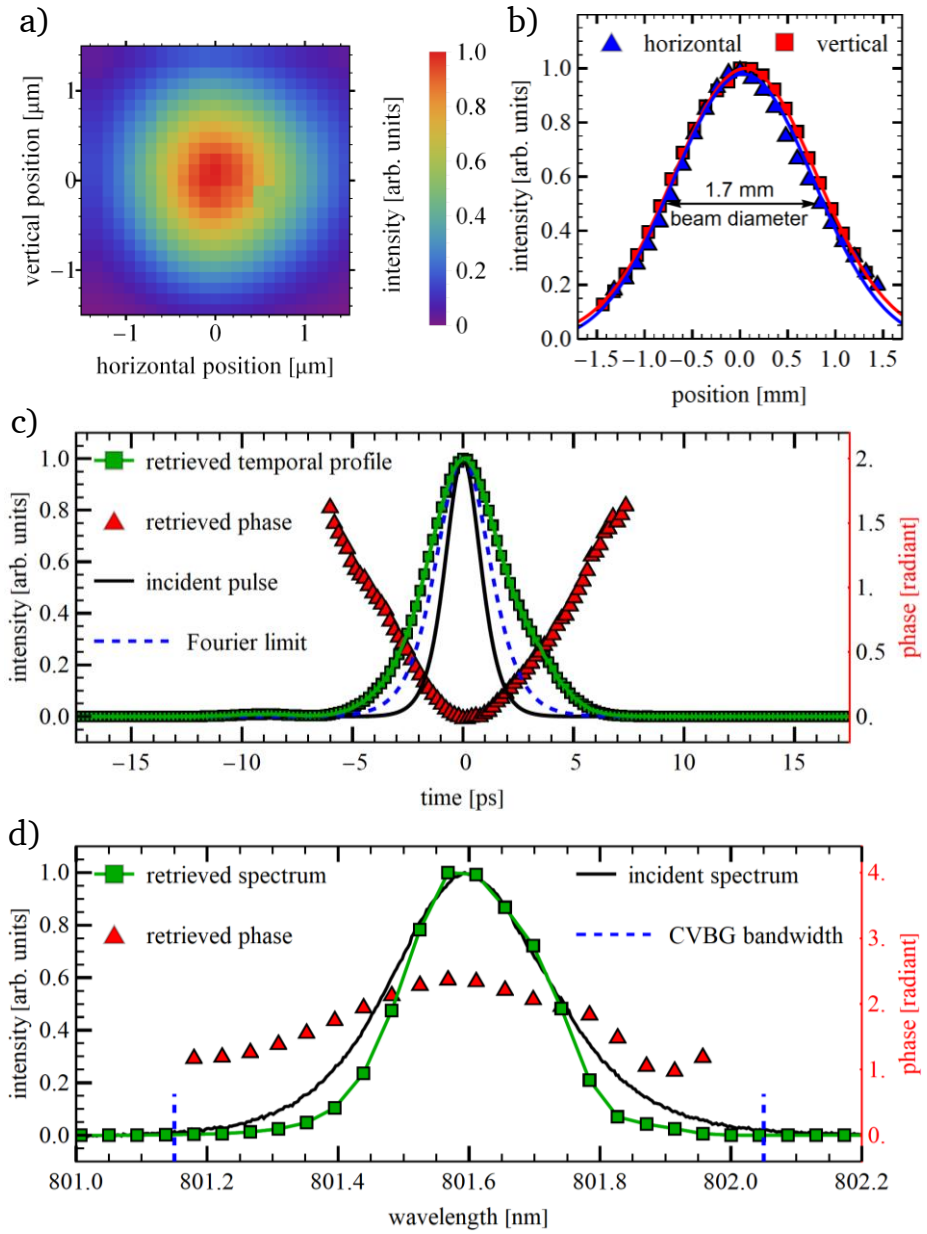

Figure 2.4: a) Beam intensity profile. b) Vertical and horizontal beam profiles and Gaussian fits. c) Reconstructed shape and phase of the amplified, compressed pulses. For comparison shapes of the incident pulse and of the Fourier limit of unamplified, recompressed pulses are shown. d) Reconstructed spectrum and phase of the amplified, compressed pulses. For comparison the incident spectrum and the CVBG bandwidth (FWHM) are shown.

α and, hence, the Bragg condition (Fig. 2.3 b)). The bandwidth of the CVBGs is 1.1 nm (FWHM) giving a stretching factor of 648 ps/nm for double-pass configuration and a stretched pulse duration of about $\tau_p = 200$ ps. After four passes through the CVBG the bandwidth is reduced to $\Delta\lambda_{CBG} = 0.9$ nm (FWHM). We note that the limited bandwidth causes a spectral clipping of the laser pulses, which leads to an increased Fourier limited pulse duration of $\tau_p = 3$ ps (FWHM). Here, we have to make a compromise between the stretched pulse duration and the transmitted bandwidth. Note that only one CVBG is necessary for both, the

stretcher and the compressor, as we invert the chirp by a propagation in opposite direction (see Fig. 2.2 stretcher and compressor).

The diffraction efficiency of the CVBG is 94 % and we measured a total transmission in double-pass configuration of 89 % including spectral losses due to the limited diffraction bandwidth. The losses are mainly caused by scattering in the CVBG [51], but are in the same range as for surface gratings (or even lower).

The total size of the ring regenerative amplifier with stretcher and compressor (without the pump laser, see Fig. 2.2) is 60 cm x 70 cm = 0.42 m², i.e., roughly half the area of commercially available surface grating based systems.

The CVBG based regenerative amplifier delivers output pulses with an energy of up to $E_p = 5$ mJ (standard deviation below 5 % in saturation), at a pulse duration of $\tau_p = 4$ ps (FWHM), a bandwidth of $\Delta\lambda = 0.26$ nm (FWHM), and a beam diameter of $d = 1.7$ mm (FWHM) with an almost Gaussian shape (Fig. 2.4 a) and b)). Pulse characterization was done by a polarization gated frequency resolved optical gating (FROG) measurement and two-dimensional phase-retrieval (Fig. 2.4 c) and d)), giving a residual chirp of -0.02 THz/ps, which is irrelevant for the experiments. The time bandwidth product is 0.5. The amplifier can deliver even higher output pulse energies above $E_p = 5$ mJ, but we restricted our measurements, as the damage threshold of the CVBG for (ps) laser pulses at $\lambda = 800$ nm is not well-known. At a pulse energy of $E_p = 5$ mJ, the maximum intensity at the CVBG was $I = 75$ GW/cm² corresponding to a fluence of $F = 0.3$ J/cm² without causing visible optical damage. We measured the pulse duration after the stretcher to be about $\tau_p = 200$ ps (FWHM), corresponding to a stretching factor of 580 ps/nm. We determined the unamplified, recompressed pulse duration to $\tau_p = 3$ ps (FWHM), which fits to the Fourier limited pulse duration. Thus, this increase of the pulse duration is caused by the spectral clipping at the CVBG. We checked the tunability from $\lambda = 798$ nm to $\lambda = 812$ nm, so the amplifier setup works for the designed wavelength range.

2.1.3 Optical parametric amplifier (OPA)

In this subsection, we describe the OPA (see Fig. 2.1) and its design criteria, as we developed, built and characterized it during this work.

In order to perform experiments with two high-intensity (ps) laser pulses and/or to reach other spectral regions, we amplify the tunable visible output of the OPO. In the range between $\lambda = 505 - 700$ nm there are in principle two main options for an amplifier: pulsed dye amplifier (PDA) or OPA. The PDA needs an optical pump source, which has to be well timed in respect to the seed pulses. This is due to the short excited laser level lifetime for laser dyes in the range of one nanosecond [2]. Further, a PDA requires regularly maintenance work, especially the exchange of the dye solution due to degradation and to enable the large tuning range. In comparison, an optical parametric amplifier needs an even more precise timing, as the energy transfer from the pump to the seed pulse only happens, if the two pulses overlap. As we work with (ps) laser pulses, the timing precision should be below a picosecond. On the other hand, an OPA, which simply requires overlapping beams in an optical nonlinear crystal, does not require any maintenance. For

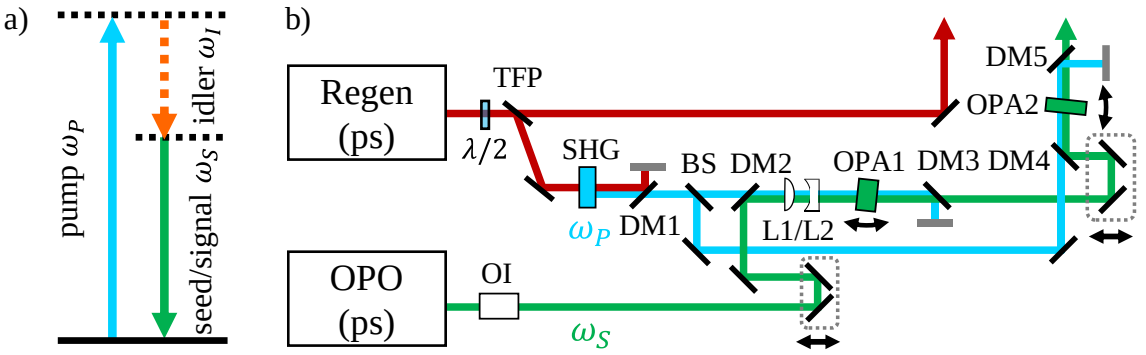

Figure 2.5: a) difference frequency-mixing scheme for OPA. b) Setup of the two-stage OPA: SHG, second-harmonic generation; DM, dichroic mirror; BS, beam splitter; L, lens; OI, optical isolator, OPA1/2: BBO crystals of stage 1 and 2. The idler is not shown for simplicity.

tuning the wavelength, only the critical phase matching has to be optimized by turning the nonlinear optical crystal.

In our specific laser system there was already a PDA installed, which enabled the amplification of (ps) laser pulses of the OPO ($\lambda = 505 - 540$ nm with Coumarin 307) up to an energy of $E_p = 1 - 2$ mJ [23,56]. This would enable pump probe experiments with two high intensity (ps) laser pulses (together with the regenerative amplifier), but there are two severe problems: First, the PDA requires a pump pulse in the UV, which is the third-harmonic of the Nd:YAG laser ($\lambda = 355$ nm). The generation of the third-harmonic changes the beam profile of the second-harmonic of the Nd:YAG laser (pump radiation of the regenerative amplifier) in such way, that we cannot use it directly for pumping the regenerative amplifier (intensity fluctuation in the transverse beam profile (hot spot), a spatial filter was not tested) [44]. Second, the amplified pulse after the PDA precede the pulse of the regenerative amplifier by about $t_D = 300$ ns (duration of the amplification in the regenerative amplifier). This would correspond to a delay line of $L = 100$ m length, which is cumbersome and can affect, e.g., the beam pointing stability. Consequently, we decided to build an OPA, which offers us a faster tunability (no exchange of dye, mirrors, pump radiation) and less maintenance on the cost of lower pulse energies. In addition an OPA offers the idler radiation at no additional costs, which we utilized for instance for a master thesis project as a Stark laser [57].

The difference frequency-mixing scheme for optical parametric amplification is shown in Fig. 2.5 a). The idea is to transfer energy from the pump to the seed beam, hence, the pump wavelength has to be shorter than the seed wavelength. Further, the idler is generated to fulfill energy conservation $\hbar\omega_P = \hbar\omega_S + \hbar\omega_I$. Momentum conservation requires $\hbar\vec{k}_P = \hbar\vec{k}_S + \hbar\vec{k}_I$ with the wave vectors $\vec{k}_i$, which we enable by critical phase matching in nonlinear crystals.

The OPA, which has been set up and utilized during this work, is shown in Fig. 2.5 b). It is a two-stage OPA for the OPO pulses pumped by the second-harmonic of the regenerative amplifier [58] (the referenced bachelor thesis describes the first stage only).

The pump pulses of the OPA at 400 nm are generated via SHG in a beta barium borate crystal (BBO, dimensions: 10 mm x 10 mm x 2 mm, cut angle 29.2°, antireflection coating 400/800 nm). The pulse energy of the regenerative amplifier

utilized for SHG is adjusted by a variable attenuator consisting of a half-wave plate and a polarizer. For laser pulses from the regenerative amplifier (wavelength $\lambda =$ 800 nm) with an energy of $E_p = 2.5$ mJ (beam radius $1/e^2$ w =1.25 mm) we obtained with a conversion efficiency of roughly 50 % SHG pulses with an energy of $E_p = 1.3$ mJ at $\lambda = 400$ nm (standard deviation depending on the stability of the regenerative amplifier, typically <5 %). We separate the $\lambda = 400$ nm pump beam of the OPA from the residual $\lambda = 800$ nm by a dichroic mirror (DM1, 1-OS-2-0254-5-[4D45], Altechna) and split the pulse energy by a partial reflective mirror (BS, BST10, Thorlabs). For parallel polarization we measured a splitting of $E_p = 450\,\mu$J transmission to the first stage and of $E_p = 850\,\mu$J reflection to the second stage. The pump and seed pulses (from the OPO) are overlapped in space with a dichroic mirror (DM2, DMSP425, Thorlabs). Both OPAs are in collinear geometry, because it is easy to align and the increase of the phase matching bandwidth by a non-collinear geometry is not necessary for picosecond pulses [48,59]. The pulses are overlapped in time utilizing an adjustable delay stage (2.5 cm traveling range with differential drive, 50 cm with a rail, times a factor of two for the delay, because of the reflection geometry). The maximal possible delay in this setup of one meter corresponds to a delay time of $t_D = 3$ ns, which is below the cycle time in the regenerative amplifier (10 ns) and with that not all roundtrip number changes are easy to implement for the OPA. However, there is no need to adjust the number of roundtrips frequently. Before the first OPA, we have a Galilean telescope with a $f = 75$ mm lens (L1, LA1608-A, Thorlabs) and a $f = -50$ mm lens (L2, LC1715-A, Thorlabs), resulting in 1.5 times smaller beam diameters and with that a factor of 2.25 higher intensities. The amplification in the BBO of the first OPA (BBO, dimensions: 5 mm x 5 mm x 5 mm, cut angle 29.2°, anti-reflection coating 400/800 nm, other coating would be beneficial for the seed/signal) is in the range of a factor 10^4, leading to signal pulse energies of $E_p = 10\,\mu$J. Note that for slightly higher pump intensities we observe a strong broadband (blue-green to red) optical parametric generation (OPG) yield. The weakly depleted pump is separated by a dichroic mirror (DM3, DMLP425, Thorlabs). The temporal overlap for the second OPA is adjusted again in the beam path of the seed/signal radiation utilizing a delay stage (2.5 cm traveling range with differential drive). The pump and the seed pulses (from the first OPA) are overlapped again with a dichroic mirror (DM4, DMSP425, Thorlabs). The amplification in the BBO (dimensions: 9 mm x 9 mm x 3 mm, cut angle 29.2°, p-coating) of the second OPA is in the range of a factor 10, leading to signal pulse energies of up to 100 μJ. The slightly depleted pump is sort out by a dichroic mirror (DM5, DMLP425, Thorlabs). The idler is as well separated using dichroic mirrors. The whole setup (mirrors and crystals) is suited for the full visible tuning range of the OPO $\lambda = 505 - 700$ nm and delivers pulse energies of up to $E_p = 100\,\mu$J with a pulse duration of $\tau = 2.0(3)$ ps (FWHM, measured by FROG) with a bandwidth of $\Delta\lambda = 0.6(2)$ nm. The transversal beam profile is close to a Gaussian.

The output pulse energy of the two-stage OPA in the range of $E_p = 100\,\mu$J is sufficient for the experiments shown in chapter 3 and 4. Nevertheless, the intensity regime above $I = 10$ TW/cm² can only be analyzed in detail for energies of roughly $E_p = 1$ mJ. Hence, a power amplifier for the OPA output would be beneficial. In

principle, there are two options: First, a power amplifier for the regenerative amplifier, enabling higher pump pulse energies in the range of several millijoules ($\lambda = 400$ nm) for pumping a third OPA stage. Second, a dye power amplifier for the two-stage OPA radiation with a second frequency doubled/tripled Nd:YAG laser as a pump source (for independent timing).

2.1.4 Frequency conversion to ultraviolet

To further increase the available spectrum of the laser system, nonlinear frequency conversion in crystals (BBO) is used to reach the ultraviolet (UV) spectral regime. The UV pulses enable lower-order multi-photon transitions in rare gases for efficient low-order frequency conversion into the VUV spectral regime. A straightforward option to generate UV pulses in our laser system, utilized for the experiments in chapter 3, is second-harmonic generation of the OPA output. This enables tunable UV picosecond pulses with a wavelength of $\lambda = 252.5 - 350$ nm (OPA $\lambda = 505 - 700$ nm) with pulse energies of roughly $E_p = 10\,\mu$J. Another option utilized in chapter 4 is the sum frequency generation of the second-harmonic of the regenerative amplifier with the OPA output. For the combination of $\lambda = 400$ nm plus $\lambda = 505 - 700$ nm we obtain tunable UV with a wavelength of $\lambda = 223 - 255$ nm with a pulse energy of about $E_p = 25\,\mu$J.

Another simple option, not applied for the experiments of this work, are sum frequency generation (SFG) of $\lambda = 800$ nm and $\lambda = 505 - 700$ nm, leading to an output of $\lambda = 312 - 375$ nm. Or, aiming close to the absorption edge of BBO, SFG of the output of the regenerative amplifier with the second-harmonic of the OPA, so SFG of $\lambda = 800$ nm and $\lambda = 252.5 - 350$ nm, obtaining a wavelength of $\lambda = 192 - 244$ nm. Obviously, there are many other options to combine the two amplified, tunable pulses (and as well the idler of the OPA), but herewith we already demonstrated that we have the possibility to generate picosecond pulses with energies of several micro joules in the UV from $\lambda = 192 - 375$ nm. This enables a nearly arbitrary choice of level schemes for the experiments on nonlinear optics in coherently-driven media.

2.1.5 Pulse characterization

Characterization of ultrashort laser pulses is a requirement for precise investigations of spectral and intensity dependencies. For ultrashort laser pulses it is in general necessary to fully reconstruct the electric field, e.g., with frequency resolved optical gating (FROG) [60,61].

The laser system includes three types of laser pulse characterization devices: simple spectrometers to determine the wavelength and the bandwidth of the pulses, autocorrelators to get a quick estimate for the pulse duration and an homemade FROG setup for a full reconstruction of the amplified laser pulses [23,62,63]. Note, that our FROG setup does not provide single shot data, but needs some thousands of shots for a measurement. In order to reduce averaging effects, we apply a narrow pulse energy filtering ($1 - 5$ %).

Further, we utilized cross correlations via off-resonant sum frequency mixing in crystals and gases to determine the pulse durations in the UV.

2.1.6 Overlap of pulses in the experiment

Overlap of pulses of the regenerative amplifier and the OPA in the interaction medium (gas jet) is a crucial requirement for the experiments presented in chapters 3 and 4. Spatial overlap is simply achieved using dichroic mirrors and a camera at the focus position (using either a reflex from the input window to the vacuum chamber or a flip mirror, see Fig. 2.6). The temporal overlap is more demanding, as we do not have a direct possibility to achieve sub-picosecond timing precision (corresponds to $l = 300\,\mu$m optical pathway, same situation as for the OPA). We adjust the temporal overlap of the two pulses utilizing a delay stage (with micrometer drive, $10\,\mu$m precision) and measure roughly the timing by an ultrafast photodiode (e.g., UPD-200, Alphalas, $t = 200$ ps rise time) and a fast oscilloscope (Waverunner Xi104, Le Croy, 1 GHz bandwidth). The temporal uncertainty of the rising edge of the photodiode signal is below $\Delta t < 100$ ps corresponding to an optical pathway uncertainty of $l = 3$ cm. To further improve the temporal overlap, it is beneficial to drive a nonlinear effect, which is sensitive to the overlap on (sub-) picosecond timescale. Therefore, there are different options like optical gating, sum/difference frequency generation in the gas jet, or sum/difference frequency generation in a nonlinear crystal (like OPA). The simplest setup is the sum/difference frequency generation in a nonlinear crystal, as it does not require the running interaction chamber and VUV spectrometer, does not need additional polarizers (optical gating), works with rather low intensities and is less sensitive to the alignment of the beams. Phase matching is still critical, but it is easily possible to turn the crystal, while changing the delay between the pulses and wait for a UV flash. Because of the group delay dispersion in all following optics (especially for low wavelength), final adjustments have to be done in the gas jet.

2.2 Interaction chamber and nonlinear optical medium

The interaction chamber (see Fig. 2.6) consists of an entrance window, a gas nozzle, which creates the gas jet, and a turbomolecular pump to generate the vacuum ($10^{-4} - 10^{-3}$ mbar depending on the stagnation pressure of the operating nozzle). In general, there are different interaction region designs for frequency conversion into the VUV. The gas jet is a simple approach, with a rather short interaction length and particle density, but it offers low reabsorption and a low phase mismatch. Other approaches like gas cells or capillaries offer much longer interaction length and particle densities yielding much higher NL products [13,41]. This causes typically much higher conversion efficiencies. During this work, we improved our gas jet with a modification, which confines the gas (see Appendix B). Although the experiments with the modified gas jet were successful, we performed the measurements in chapters 3 and 4 with the simple gas jet, because the signal levels were sufficient with the lower NL product and we did not want perturbing phase-matching effects.

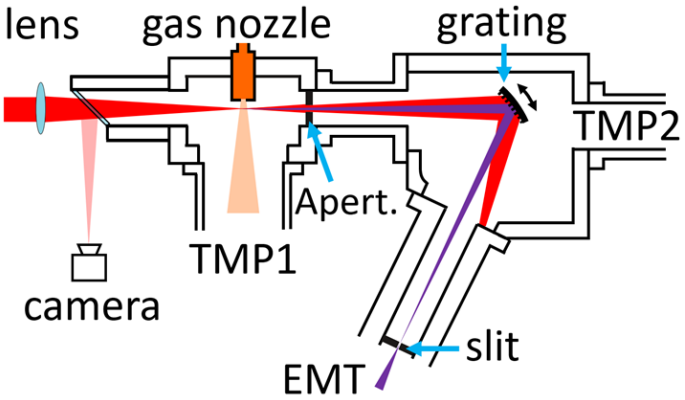

Figure 2.6: Experimental setup of the interaction chamber (left part) and the VUV spectrometer (right part). The aperture between the interaction chamber and the VUV spectrometer enables differential pumping and is not the entrance aperture of the spectrometer, which is the laser focus itself. TMP: turbomolecular pump, EMT: electron multiplier tube.

The entrance window of the interaction chamber is a 2 mm thick UV-grade fused silica window (UVFS, PW-S-000918, Laseroptik) with an angle of incidence of 45°. This enables a high transmission for linear, p-polarized radiation. We utilize one of the reflexes of the entrance window for beam diagnostics, either with a camera for focus profile measurements or with a photodiode for pulse energy measurements. For experiments with circular polarized light, we replaced the entrance window with a flat, antireflection coated window to maintain the polarization [57]. The gas jet is generated by a pulsed nozzle (9S1-A1-P1-9B08, General Valve, orifice diameter 0.8 mm, 45° cone). We adjust the stagnation pressure with a pressure regulator. Typically stagnation pressures are between $p = 200 - 700$ mbar, obtaining particle densities in the focus of roughly $N = 10^{17}\mathrm{cm}^{-3}$ [64]. Thus, the amount of atoms in the focus is roughly 10^{10} ($d = 10\,\mu$m focus diameter, $L = 1$ mm interaction length). For each experiment, we checked for a quadratic pressure/particle density dependence of the frequency conversion signal. Phase matching and especially for xenon cluster generation at higher pressures can perturb this dependency [13,65].

The nozzle can be aligned by micrometer drives in three dimensions (x,y,z), which enable a perfect overlap with the focus of the laser beam [66]. The distance between the nozzle and the laser beam was minimized such, that there was no overlap between the nozzle and the laser beam. We apply voltage pulses from a home-made nozzle driver to open the pulsed nozzle with a repetition rate of $f_r = 20$ Hz (same repetition rate as the amplified laser pulses). The timing of the voltage pulse is relatively uncritical, because we observed a broad plateau region ($\Delta t = 400\,\mu$s), when we changed the delay between the laser pulse and the voltage pulse.

2.3 Detection setup - VUV spectrometer

For the detection of the generated radiation in the VUV spectral regime we utilize a home-made Seya-Namioka spectrometer [23,66,67] (see Fig. 2.6). There is no entrance slit, as the laser focus with a diameter of $d < 100\,\mu$m in the gas jet itself

operates as a slit. The beam passes afterwards an aperture, which enables differential pumping and pressures of down to 10^{-5} mbar in the VUV spectrometer. That enables near lossless propagation for the VUV radiation. The central element of the spectrometer is the concave grating (52200250, HORIBA Jobin Yvon) with a focal length of $f = 100$ mm. The spectrometer has a fixed deviation angle of 64° (the grating has to be turned by 32° for zero-order diffraction), so we turn the grating to select the wavelength. Typically we select the minus first diffraction order (at 35° for the grating), although the plus first has a similar strength. Note that also higher diffraction orders appear (roughly up to 5^{th} order), but with a significantly reduced intensity. The exit slit of the spectrometer has an adjustable width, to decide between maximal detection efficiency and maximal spectral resolution. The slit is not moveable in longitudinal direction, so the focus position in the interaction chamber has to be optimized for the best spectral resolution. We detect the VUV radiation with an electron multiplier tube (R595, Hamamatsu). The time resolution of the EMT is in the range of 10 ns. More details on the detection system can be found in the PhD thesis of Ackermann [23]. Note that the grating diffraction efficiency depends on the input polarization (horizontal/vertical).

2.4 Data collection

For every amplified laser pulse (repetition rate $f_r = 20$ Hz), we measure single shot data with a digital oscilloscope (PicoScope 4824, Pico Technology) and data acquisition cards (PCI-6221/PCI-6229, National Instruments). The full collection of data enables filtering and binning afterwards regarding, e.g., pulse energies (monitored by calibrated photodiodes (PDI-400, Becker&Hickl), wavelength and/or stagnation pressure.

3 Resonantly enhanced harmonic generation via dressed states with large Autler-Townes splittings

In this chapter, we investigate harmonic generation (HG) of ultrashort pump laser pulses enhanced by preparation of dressed states. A control laser pulse with appropriately matched frequency and/or peak intensity (TW/cm²) serves to generate the dressed states with large, tunable Autler-Townes (AT) splittings in the THz range. The energetic position of the dressed states is laser-controlled to match with a multiple number of pump laser photons. This enables resonance enhancement of the nonlinear susceptibility and of harmonic generation also for fixed-frequency and off-resonant pump laser pulses. Moreover, the tunable Autler-Townes splittings serve to compensate and even exploit inevitable ac Stark shifts of atomic resonances, which otherwise reduce the nonlinear response of the medium. The fundamental question of this chapter is, whether the high intensities (TW/cm², Keldysh parameter $\gamma \approx 1$) still permit us to drive and exploit dressed states for enhancement of harmonic generation.

Resonantly enhanced frequency conversion: Frequency conversion and harmonic generation into the VUV spectral regime in media of rare gas atoms suffers from low conversion efficiencies due to small nonlinear susceptibilities. Hence, it is a straightforward approach to use atomic resonances to enhance the nonlinear susceptibilities (see section 1.2). The investigations of the effect of (bare) atomic resonances in high intensity nonlinear optics started with studies on above threshold ionization [68–70], which later also lead to theoretical [29,71–73] and experimental studies [74–76] on applications in high-harmonic generation. Recent work extended the investigations towards autoionizing states [77,78] and giant autoionizing resonances [79,80], e.g., leading to large resonance enhancements in laser produced plasma plumes [76,81,82]. However, there are two fundamental problems, which limit the applicability of resonance enhancements (at high intensities): availability of resonances, especially for typically fixed-frequency pump lasers, and perturbing, inevitable ac Stark shifts. In this chapter, we show that both problems can be addressed by nonlinear optics in quantum systems, coherently-driven by a control laser, i.e., by dressed states with large Autler-Townes splittings.

Autler Townes splittings for frequency conversion: As mentioned in the introduction, Autler-Townes splittings for frequency conversion were already studied in a rather low-intensity regime [27,28], exploiting the improved phase matching conditions between dressed states. Recently, a theoretical study gave some evidence of the role of dressed states in high-harmonic generation also in the strong field regime [29]. Here, we aim at preparation of dressed states with large tunability of their energetic position and resonantly enhanced harmonic generation via these states. In particular, we focus at applications in the regime of high intensities (i.e., many TW/cm²), large Autler-Townes splittings of many THz, and higher-order frequency conversion processes.

The chapter is structured as follows: In a first set of experiments, we spectroscopically investigate the features of resonantly enhanced THG via dressed states in

argon for high control intensities ($I_C = 7$ TW/cm²) and a Keldysh parameter of down to $\gamma \approx 4$. We study the dependency of the Autler-Townes splitting on control intensity and control detuning. For an initially detuned pump wavelength, we are able to enhance the THG by almost two orders of magnitude. In addition, we show the compensation of inevitable ac Stark shifts for one of the dressed states.

In a second set of experiments, we demonstrate an application of resonantly enhanced harmonic generation via dressed states in xenon. For a large initial pump detuning of $\Delta_P^{(3p)}/2\pi = 69$ THz we observe a control laser induced resonance enhancement of more than one order of magnitude. This enhancement is not restricted to THG, but observable also for a higher-order process (e.g., FHG) as well. We applied high control intensities ($I_C = 4$ TW/cm²) corresponding to a Keldysh parameter of down to $\gamma \approx 7$.

In a third set of experiments, we show that also in a single laser approach, i.e., with the pump laser alone, large Autler-Townes splittings occur, which strongly modify the atomic level structure at high intensities ($I_C = 7$ TW/cm², Keldysh parameter $\gamma \approx 5$). This approach is much simpler, as only one intense laser pulse is required, but suffers from a reduced flexibility. We observe resonance enhancements for originally far detuned wavelengths and investigate the strongly modified level structure.

The main research results of this chapter were published in "Journal of the Optical Society B" [76].

3.1 Basic concept

The idea of resonantly enhanced harmonic generation via dressed states is depicted in the coupling scheme in Fig. 3.1 a): We consider the typical situation of (high-) harmonic generation, i.e., a pump laser is far off any atomic resonance in the medium. In our example, we discuss the lowest-order frequency conversion process in a gaseous medium, i.e., third-harmonic generation (THG), though our concept is not limited to this case. In our example, the large three-photon detuning $\Delta_P^{(3p)} = 3\omega_P - \omega_{12}$ with regard to the transition between the ground state $|1\rangle$ and the lowest excited state $|2\rangle$ (angular transition frequency ω_{12}) limits the conversion efficiency. To prepare a three-photon resonance and enhance the THG yield, we apply a control laser pulse, tuned close to a single-photon resonance between some excited atomic states (see states $|2\rangle$ and $|3\rangle$ in Fig. 3.1 a)). As it is well-known from coherent light-matter interaction [34], the control laser modifies the level structure of the "bare" atomic states $|2\rangle$ and $|3\rangle$ to generate "dressed" states $|a^{\pm}\rangle = |2\rangle \pm |3\rangle$ with dressed energies $\omega^{\pm}(I_C)$. The dressed states are energetically arranged below and above the energy of the initial bare state $|2\rangle$ (see Fig. 3.1 b), same for dressed states around the initial bare state $|3\rangle$, which do not matter for the following discussion). The energy difference between the dressed states is the Autler-Townes splitting, which is given (in units of angular frequency) by the effective Rabi frequency $\overline{\Omega}_C = \sqrt{\Omega_C^2 + \Delta_C^2}$, with the control Rabi frequency $\Omega_C = \mu_C \cdot E_C/\hbar$, involving the transition dipole moment μ_C on the transition $|2\rangle \leftrightarrow |3\rangle$ (angular transition frequency ω_{23}), the electric field amplitude E_C of the control laser, and the detuning $\Delta_C = \omega_C - \omega_{23}$ of the control laser from the single-

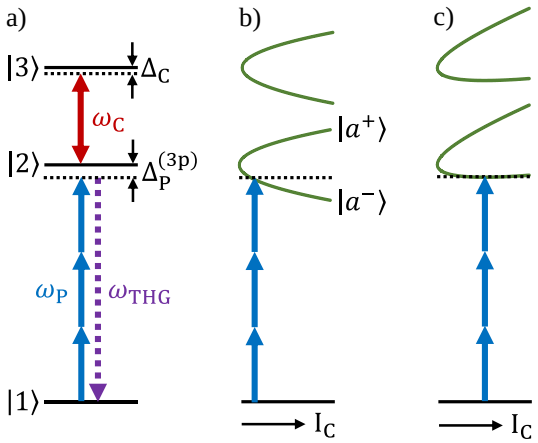

Figure 3.1: Coupling schemes for THG, resonantly enhanced via laser-controlled dressed states. a) Bare state couplings with the angular frequency of the pump laser ω_P, of the THG ω_{THG} and of the control ω_C. b) Variation of the dressed energies $\omega^{\pm}(I_C)$, depicted in green color, with the control intensity I_C. c) Effect of additional ac Stark shifts upon the dressed states. Note that we changed the nomenclature for the bare states in regard to Fig. 1.1. The former state $|4\rangle$ is now state $|2\rangle$, in order to simplify the three-photon transition.

photon resonance. On resonance ($\Delta_C = 0$) the Autler-Townes splitting simply varies with the control intensity as $\overline{\Omega}_C \sim \mu_C\sqrt{I_C}$. As the control pulse drives a single-photon transition (i.e., with large transition moment), already moderate control laser intensities permit large Autler-Townes splittings. Their magnitude can reach 100 THz, as recent investigations in transient absorption spectroscopy [83–85] and harmonic generation [29] demonstrated. Hence, we approach a regime, where the Autler-Townes splittings become similar to the laser frequency. Figure 3.1 b) schematically indicates this variation of the dressed states with the control intensity. We choose the latter now such, that one of the dressed states is driven into multi-photon resonance with the pump laser (see, as an example, the three-photon transition $|1\rangle \leftrightarrow |a^-\rangle$ in Fig. 3.1 b)). Hence, rather than tuning the pump laser to a resonance (which is not possible for intense, fixed-frequency pump pulses and/or atomic resonances very far away) we generate an appropriate resonance and tune it to the pump laser. This resonance will enhance any frequency conversion process, e.g., THG as in our example, but also fifth-harmonic generation (FHG) or higher-order processes.

We note that for intense laser fields, all atomic states experience significant ac Stark shifts. For highly excited states, the ac Stark shifts are in good approximation similar to the ponderomotive energy, i.e., the quivering energy of a free electron in a dynamic electric field [22,41] (see subsection 1.2.1 and Appendix A). The approximation is suited to all excited states in rare gas atoms, where only the ground state is far from the ionization continuum. In this case, the direction of the ac Stark shift is mostly towards higher energy. This is also the reason, why the compensation of ac Stark shifts, driven by visible or infrared radiation, is hard to achieve in rare gas atoms [57]. The ac Stark shift effects the highly excited dressed states by pushing them upwards with increasing laser intensity and modifies the variation of the dressed energies $\omega^{\pm}(I_C)$ with the control laser intensity (see Fig. 3.1 c)). The variations of the two dressed energies are no longer symmetric. Nevertheless, the

concept to provide a laser-controlled resonance with the pump laser still works also in the presence of additional ac Stark shifts.

We note that the Autler-Townes splittings dynamically change, as the control pulse intensity varies in time. Hence, in the situation depicted in Fig. 3.1 b), the resonance condition with the pump pulse will only be maintained during a short time interval (indicated in Fig. 3.1 b) by the sharp crossing of the dashed line representing $3\omega_P$ with the variation of the dressed energy $\omega^-(I_C)$ vs. control intensity). The ac Stark shift improves this situation. As the shift depends linearly upon the control intensity and is directed upwards, it changes the steady drop of $\omega^-(I_C)$ towards a smoother, flat variation. Thus, the dressed state remains much longer close to three-photon resonance with the pump pulses. This is a quite interesting feature, as in conventional resonantly enhanced harmonic generation with a single tunable pump laser, the ac Stark effect strongly reduces the conversion efficiency by dynamically driving the excited state away from resonance by orders of magnitude. In our approach, the ac Stark shift serves to maintain a near-resonance condition for a longer interval. Hence, we expect to even benefit from the ac Stark shift with our dressed state concept.

3.2 Theoretical description

The theoretical considerations of this chapter follow the approach of nonlinear optics in coherently-driven quantum systems shown in section 1.3. The relevant parameter for THG is the coherence ρ_{12} on the three-photon transition between the ground state $|1\rangle$ and the excited state $|2\rangle$ (compare Fig. 3.1). In order to simplify our Hamiltonian, we describe the interaction on the three-photon pump transition via the three-photon Rabi frequency of the pump laser $\Omega_P^{(3p)}$. A three-photon Rabi frequency includes excitation pathways over all intermediate states $|i\rangle$ and $|j\rangle$ and is given by:

$$\Omega^{(3p)} = \sum_{i,j} \frac{\mu_{1i}\mu_{ij}\mu_{j2}}{2\hbar^3\Delta_{1i}\Delta_{ij}} E_{0,\omega}^3 = \sum_{i,j} \frac{\Omega_{1i}\Omega_{ij}\Omega_{j2}}{2\Delta_{1i}\Delta_{ij}} \tag{3.1}$$

with the single-photon detunings Δ_{ij}. Here, we assume the three-photon Rabi frequency to be small, i.e., we suppose that the pulse area (product of Rabi frequency and pulse duration) is small $\Omega_P^{(3p)}\tau_P \ll 1$. That means that the variation of THG with the pump detuning is relatively independent on the specific pulse area. In simple terms, the THG is just a probe for the control laser induced Autler-Townes splitting. The basic Hamiltonian in Dirac representation with dipole and rotating wave approximation is given by [34]:

$$\hat{\mathrm{H}}(t) = \frac{\hbar}{2}\begin{pmatrix} -2\Delta_P^{(3p)} - 2S(t) & \Omega_P^{(3p)}(t) & 0 \\ \Omega_P^{(3p)^*}(t) & 0 & \Omega_C(t) \\ 0 & \Omega_C^*(t) & 2\Delta_C \end{pmatrix} \tag{3.2}$$

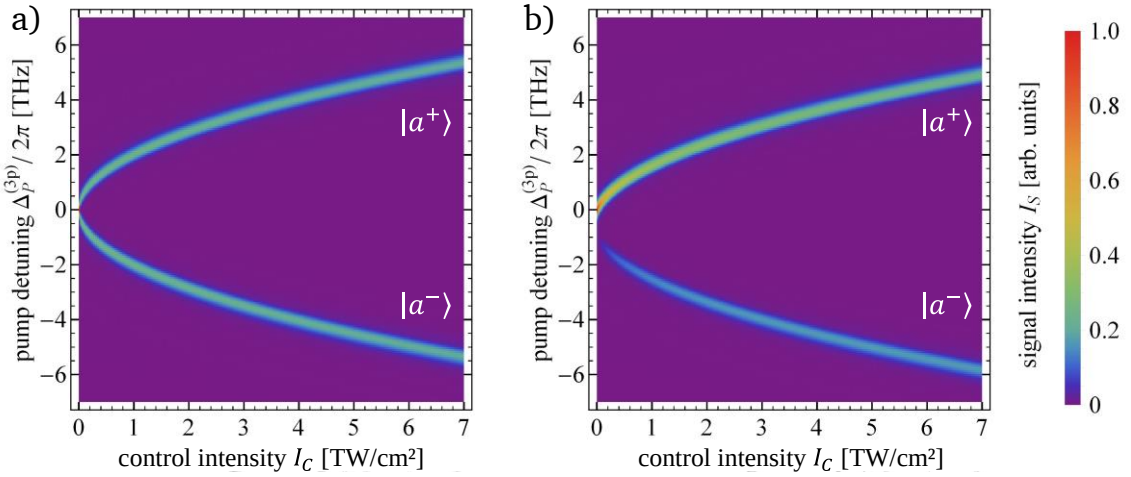

Figure 3.2: Numerical simulation of THG signal intensity vs. control intensity and pump detuning. We assume a control transition dipole moment of $\mu_C = 10^{-30}$ Cm. a) on resonance $\Delta_C = 0$. b) off resonance $\Delta_C/2\pi = 1$ THz. We neglect additional ac Stark shifts.

We added the ac Stark shift S to the three-photon detuning. Hence, we assume that the ac Stark shift is the same for both excited states $|2\rangle$ and $|3\rangle$.

Let us now have a look at the dependency of Autler-Townes splittings on control intensity and detuning, and how both effect the strength of the two dressed states. Figure 3.2 shows a numerical simulation of THG signal intensity versus control intensity and pump detuning. For the resonant case (Fig. 3.2 a), $\Delta_C = 0$) we observe a symmetric splitting of the two dressed states $|a^{\pm}\rangle$ with the Rabi frequency $\Omega_C \sim \sqrt{I_C}$. Note that due to the level splitting the THG signal intensity via the dressed states is lower than via the unperturbed resonance. However, for originally off-resonant pump wavelengths one can choose the control intensity such, that there is a strong dressed state resonance enhancement.

The dressed states energies and strengths change with a control laser detuning (see Fig. 3.2 b)). The splitting of the dressed states is now asymmetric and is described by the effective Rabi frequency $\bar{\Omega}_C = \sqrt{\Omega_C^2 + \Delta_C^2}$. Hence, we see without the control laser (i.e., $I_C = 0$) a splitting of Δ_C. The splitting is completely asymmetric, so the dressed state $|a^+\rangle$ is exactly on the unperturbed resonance position, meanwhile dressed state $|a^-\rangle$ is detuned by $\Delta_P^{(3p)} = -\Delta_C$. The strength of the dressed states differs accordingly, so we actually do not observe dressed state $|a^-\rangle$ at $I_C = 0$. For an increasing control intensity we see, that the Autler-Townes splitting becomes more symmetric around the unperturbed resonance and the strength of the two dressed states becomes more similar.

Figure 3.3 shows the THG signal intensity versus pump and control detuning for two different control intensities. For both intensities we observe for a resonant control laser a symmetric Autler-Townes splitting (compare Fig. 3.2 a)). Off resonance, the situation is quite different. In the case of a low control intensity, low control Rabi frequency (Fig. 3.3 a)), we see that only one dressed state is dominant at $|\Delta_C/2\pi| > 2$. The stronger dressed state for each control detuning is located almost at the unperturbed resonance position. Hence, the modification of the level scheme by the control laser vanishes. However, it is still possible to calculate the

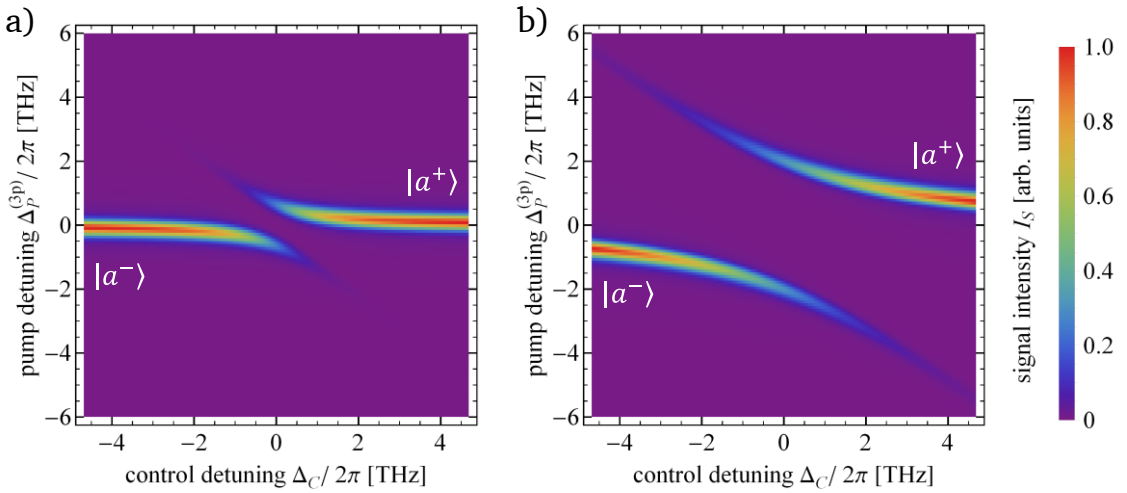

Figure 3.3: Numerical simulation of THG signal intensity vs. control and pump detuning. We assume a control transition dipole moment of $\mu_C = 10^{-30}$ Cm. a) Low intensity $I_C = 0.1$ TW/cm². b) High intensity $I_C = 1$ TW/cm². We neglect additional ac Stark shifts.

energetic position of both dressed states. The weaker dressed state is then detuned from the resonance by the negative control detuning ($\bar{\Omega}_C(\Omega_C \to 0) = \Delta_C$) and the Autler-Townes splitting is completely asymmetric.

If we require a dressed resonance at a large pump detuning, e.g., $\Delta_P^{(3p)}/2\pi = 4$ THz, then it is beneficial to use a high control intensity. For a high control intensity, we see in Fig. 3.3 b) that the dressed state $|a^+\rangle$, e.g., at $\Delta_P^{(3p)}/2\pi = 4$ THz, is much stronger than in the low intensity case. Hence, under conditions of large pump detuning high control intensities and Rabi frequencies are necessary. Another important finding of Fig. 3.3 is, that the relative strength between the dressed states varies with the control detuning, and can even be easily inverted by a change of sign in the latter parameter.

3.3 Spectroscopic investigation

We start our experimental studies with the spectroscopic investigation of the Autler-Townes splittings. We address the following questions experimentally: How large are the Autler-Townes splittings and up to which intensity or Keldysh parameter can we utilize or observe them? What is the resonance enhancement via the two dressed states and how does the enhancement and the energetic positions of the dressed states vary for different detunings? We compare the experimental results to a numerical simulation, which can be used to predict optimal enhancements for future experiments.

3.3.1 Level scheme

We performed a first experiment on resonantly enhanced THG via dressed states in argon. The pump laser is tunable in the vicinity of the three-photon resonance from the ground state $|1\rangle = 3p^6\ (^1S_0)$ to the excited, intermediate state $|2\rangle = 3p^5\ 4s\ ^2[3/2]_1$ (see Fig. 3.4). The control laser drives a single-photon resonance between the intermediate state $|2\rangle$ and two closely spaced higher excited states $|3\rangle = 3p^5\ 4p\ ^2[3/2]_{1,2}$, which under our experimental conditions of large control Rabi frequencies can be considered as a single state $|3\rangle$ (transition wavelength $\lambda_{23} = 805.5$ nm). The control laser induces Autler-Townes splittings in the strongly-driven two-level sub-system of states $|2\rangle$ and $|3\rangle$. As we will see later, we observe some perturbing effects due to a coupling to a fourth state by the control laser. This leads to an additional dressed state $|a^0\rangle$ (see Fig. 3.4). Further, from state $|4\rangle$ one-photon ionization is possible.

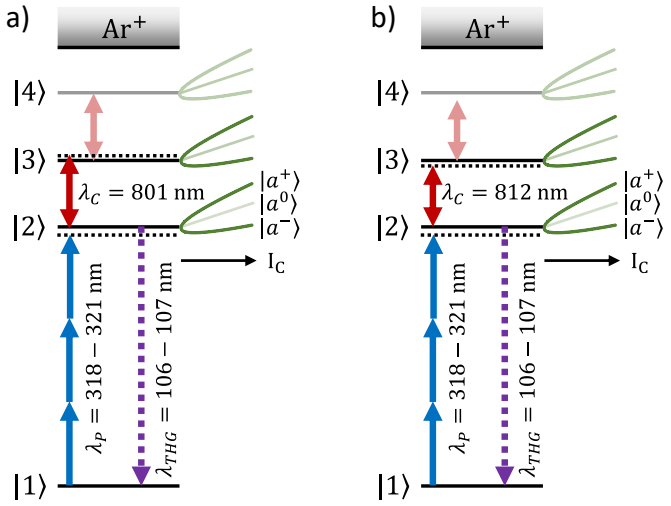

Figure 3.4: Coupling schemes in argon for two different control detunings. a) blue detuning. b) red detuning.

3.3.2 Experimental setup

For the experiment in argon, we apply the near-infrared radiation from the first beamline with the regenerative amplifier as fixed-frequency control beam ($\lambda_C = 801.25$ nm or 811.9 nm), and the frequency-doubled ultraviolet output of the second beamline with the OPO/OPA as a frequency-tunable pump beam ($\lambda_P = 318 - 321$ nm). We generate the second-harmonic of the OPA in a critical phase-matched nonlinear crystal (BBO, dimensions: 7 mm x 7 mm x 5 mm, cut angle 45°, polished) and separate it from the fundamental radiation by a colored glass filter (FGUG 5-UV, Thorlabs, UG5 glass). We generate UV pulses with an energy of $E_P = 10\,\mu$J, which we overlap with the control beam (pulse energy up to $E_C = 300\,\mu$J) by a dichroic mirror and focus both by a lens (here $f = 200$ mm) to beam diameters of $d_P = 36\,\mu$m and $d_C = 40\,\mu$m (1/e² of intensity). We chose the beam diameter of the control slightly larger, so that we obtained a more homogeneous control field for the pump radiation. The pulse duration of the control of $t_C = 4$ ps (FWHM) was longer than the pump pulse duration $t_P = 2$ ps. The stagnation pressure at the pulsed gas nozzle, which generated the gas jet, was $p = 200$ mbar of argon. The pressure dependence of THG signal was still quadratically in this stagnation pressure regime.

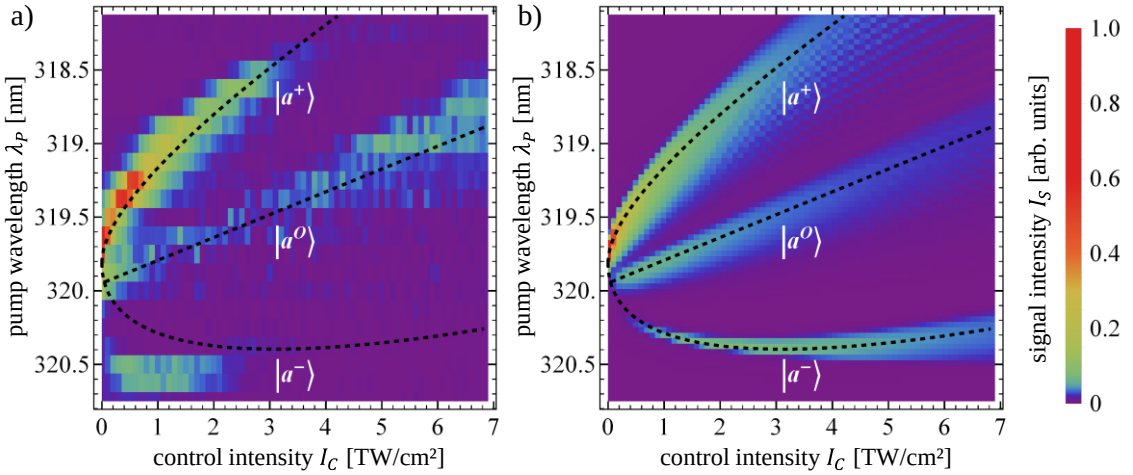

Figure 3.5: a) THG signal intensity in argon versus control intensity and pump wavelength. The pump intensity is set to $I_P = 1$ TW/cm², the control laser is blue detuned with a wavelength of $\lambda_C = 801.25$ nm. The peak control intensity of $I_C = 7$ TW/cm² corresponds to a Keldysh parameter of $\gamma \approx 4$. Black dashed lines indicate numerically simulated dressed state energies. Pump and control polarization are perpendicular to each other. b) Numerical simulation of the THG signal intensity, based on the theoretical treatment presented above. For details see subsection 3.3.4. We neglected ionization for simplicity.

3.3.3 Experimental results

Blue detuned control laser: We first studied the modified level structure for a blue detuned control laser ($\lambda_C = 801.25$ nm) by observing the THG signal intensity versus pump laser wavelength and control intensity (see Fig. 3.5 a)). We compare the experimental data to a numerical simulation of THG in a coherently-driven four-level scheme, also involving ac Stark shifts (see Fig. 3.5 b)). Without the control field (i.e., at zero control intensity) we experimentally detect maximal THG yield, when the pump laser wavelength is tuned to $\lambda_C = 319.75$ nm, i.e., close to the unperturbed three-photon resonance at $\lambda_{12} = 320/3$ nm. The small wavelength shift is due to a pump laser induced ac Stark shift, with a magnitude well approximated by the ponderomotive energy of the pump. When we switch on the control pulses, we observe pronounced level splittings. In the regime of lower control intensities up to $I_C \approx 3$ TW/cm² the spectrum clearly reveals two dressed states $|a^{\pm}\rangle$. A weaker branch $|a^0\rangle$ appears in between, which we will discuss later. The Autler-Townes splitting, i.e., the separation between branches $|a^{\pm}\rangle$, increases with the control intensity, as expected. The data show large Autler-Townes splittings of up to $\overline{\Omega}_C \triangleq 2$ nm in the pump wavelength, corresponding to $\overline{\Omega}_C/2\pi = 18$ THz in units of frequency for the three-photon transition. The branches $|a^{\pm}\rangle$ also show an asymmetric behavior in their slopes, which indicates the role of additional ac Stark shifts in the process (compare Fig. 3.1 c)). As an interesting feature of the interplay between ac Stark shift and dressed energies, branch $|a^-\rangle$ remains at an almost constant resonance position when the control intensity is varied. We note, that the THG signal intensity is different via the two dressed states, i.e., THG via branch $|a^+\rangle$ is stronger compared to branch $|a^-\rangle$. As it is well-known from the theory of coherent light-matter interactions, the relative excitation probabilities to different

dressed states vary with the control detuning [86], like we presented it in section 3.2. Only on resonance $\Delta_C = 0$ the weight of both dressed states is equal. Hence, the data indicate that the control laser is tuned close to, but not exactly on the effective control transition with angular frequency ω_{23}. We confirm later experimentally, that the ratio of the THG signal intensity via different dressed states can be changed and even inverted, when we vary the control laser detuning.

We consider now the data for higher control intensities beyond $I_C = 3$ TW/cm² up to $I_C = 7$ TW/cm² (Keldysh parameter $\gamma \approx 4$). Branch $|a^0\rangle$ dominates now the spectrum. The branch emerges due to an additional near resonant coupling induced by the control laser in our specific excitation scheme in argon, i.e., between state $|3\rangle$ and the highly excited manifold of states $|4\rangle = \{3p^5\ 4d\ ^2[1/2]_1; 3p^5\ 4d\ ^2[3/2]_2\}$ (see Fig. 3.4). At higher control laser intensity, i.e., at larger saturation broadening, state $|4\rangle$ also becomes coupled to the system. In the sub-system of three bare states $|2\rangle$, $|3\rangle$, and $|4\rangle$ with two near-resonant couplings by the control laser, we get three dressed states, usually termed "bright" states $|a^\pm\rangle$, and "dark" state $|a^0\rangle$. In general, the dressed states are linear combinations of the three bare states $|2\rangle$, $|3\rangle$, and $|4\rangle$ [87]. We clearly identify these three dressed states in the spectrum. However, for increasing control intensities the THG yield in branch $|a^0\rangle$ dominates compared to the other dressed states – while the numerical simulation does not show this effect (compare Fig. 3.5 b)). We suspect that this is due to closing of an ionization channel via state $|4\rangle$. Strong ionization occurs by (5+1) resonantly enhanced multi-photon ionization via state $|4\rangle$ with three pump photons and three control photons. At higher control intensities, the ionization threshold changes due to the ponderomotive shift. Thus, the (5+1) ionization channel closes. This changes the effective contribution of state $|4\rangle$ in the coupling scheme, and, hence, the relative strength of the dressed states. We note that a similar behavior was predicted in related simulations of a coherently-driven three-level atom in double resonance [88]. Further, we see that the dressed states $|a^\pm\rangle$ become much weaker at different control intensities. State $|a^-\rangle$ vanishes at a control intensity of about $I_C \approx 2$ TW/cm², meanwhile state $|a^+\rangle$ vanishes at about $I_C \approx 3$ TW/cm². This is due to the fact, that the ionization channel closes later for state $|a^+\rangle$, because we have a higher pump photon energy and reach for a higher energy above the unperturbed ionization threshold. The energy difference between the two pathways corresponds to a frequency of roughly $\bar{\Omega}_C/2\pi = 18$ THz, what is close to the ponderomotive energy change of the control ($\Delta I_C = 1$ TW/cm²) of $S = 14.4$ THz.

We note that without ac Stark shifts the energy of the dark state $|a^0\rangle$ would not change with the laser intensity. For a resonant control laser, i.e., at $\Delta_C = 0$ the dressed state $|a^0\rangle$ is always located in the middle between $|a^\pm\rangle$. With additional ac Stark shifts, state $|a^0\rangle$ precisely follows the dynamic shifts. Hence, the position of branch $|a^0\rangle$ serves as a measure for the ac Stark shifts in our system. The black, dashed lines in Figs. 3.5 a) and b) show the calculated variations of the dressed energies in the four-level scheme, taking ac Stark shifts by pump and control laser into account. In our model, we assumed the ac Stark shift of the excited states in argon to be similar to the ponderomotive energy (see subsection 3.3.4). The calculation confirms the experimental findings. The small deviation of the dressed

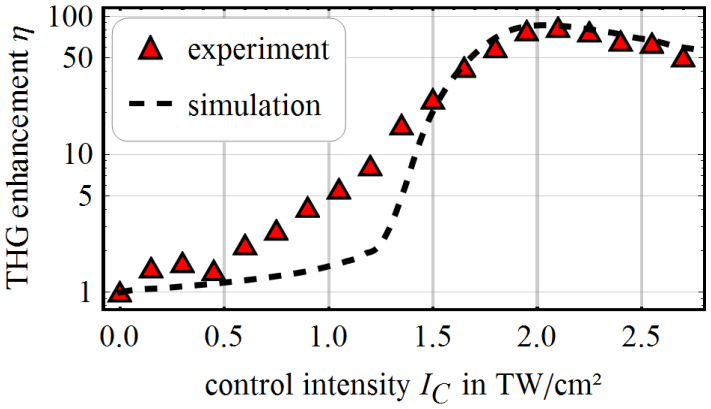

Figure 3.6: Cut along the data from Fig. 3.5 at a pump wavelength $\lambda_P = 318.75$ nm, i.e., THG signal intensity (enhancement) vs. control laser intensity. The enhancement is defined as the THG signal intensity compared to the case without control laser. The black dashed line shows a simulation. The overall line shape obtained from the simulation fits very well with the experimental data. To match the simulation with the experimentally measured maximal enhancement, we modified the simulated enhancement η_{sim} to $\bar{\eta}_{sim}(I_C) = 1 + a \cdot (\eta_{sim}(I_C) - 1)$. The correction factor a is 1/3. We attribute this correction factor to the opening of loss channels, e.g., ionization by the control laser.

energy along $|a^-\rangle$ is most probably due to additional ac Stark shifts via excited states not included in the simulation.

We confirmed for all dressed states a quadratic pressure dependence of THG signal (up to a stagnation pressure of $p = 1000$ mbar). So, we did not observe and need the possibility to phase match inbetween the dressed states [27]. However, this situation would change with a higher NL product, e.g., with the modified gas target shown in Appendix B.

We chose the polarizations of the pump and control laser to be perpendicular, because we reached higher THG signal intensities and therewith higher dressed state resonance enhancements. However, this is not always the case and depends on the specific coupling scheme, as we will see in section 3.4.

THG enhancement: As the experimental data in Fig. 3.5 a) clearly show, for (at least in principle) any arbitrary pump laser wavelength we can find a control intensity such, that a dressed state is tuned into resonance with the pump radiation. As an example, Fig. 3.6 shows a cut along the data of Fig. 3.5 a) in horizontal direction (i.e., increasing control intensity), when the pump laser wavelength is kept fixed at $\lambda_P = 318.75$ nm, i.e., well off the resonance $|1\rangle \rightarrow |2\rangle$. Without the control laser, the off-resonant pump laser alone generates a very weak THG signal intensity only. When the control laser intensity increases to $I_C \approx 2$ TW/cm², the THG signal intensity is enhanced via the dressed state by a factor of $\eta = 80$, i.e., almost two orders of magnitude. Note that this enhancement is almost as high, as tuning the pump laser directly on resonance. The difference between the experimental data and the simulation at about 1 TW/cm² is most probable due to some residual pump frequency jittering not included in the simulation.

Red detuned control laser: We consider now a red detuned control laser ($\lambda_C = 811.9$ nm, see Fig. 3.7 a)). We compare the experimental data to numerical

simulations of THG (see Fig. 3.7 b)). Roughly, we observe similar structures for experiment and simulation as in the blue detuned case (Fig. 3.5). However, there are the expected changes in both, the energetic positions and strengths of the dressed states. First, dressed state $|a^-\rangle$ is now stronger than dressed state $|a^+\rangle$ in both, experiment and simulation. Second, the energetic positions of the dressed states are shifted, which is especially visible for dressed state $|a^-\rangle$, where we observe now the constant resonance position for a control intensity of $I_C > 0.5$ TW/cm² around a pump wavelength of $\lambda_P = 320$ nm (instead of $\lambda_P = 320.5$ nm in Fig. 3.5). Note that the resonance enhancement for an initially off-resonant wavelength is in this case (red detuning) not as high as in the case of blue detuning, where we observed an enhancement of $\eta = 80$. Again we observe a feature/peak in between the two dressed states, which we identify as dressed state $|a^0\rangle$. Interestingly the dressed state $|a^-\rangle$ vanishes above a control intensity of roughly $I_C > 4$ TW/cm². This intensity is twice as large as in the case of blue detuning. Unfortunately we did not measure the vanishing of dressed state $|a^+\rangle$, to check the ionization channel closing idea. However, one would expect that the ionization channel closes at lower control intensities in the red detuned case, due to the lower control photon energy. On the other hand, the ponderomotive energy is slightly higher for the red detuned case ($\phi \sim \lambda^2$).

Conclusion: The spectroscopic investigation clearly revealed the possibility to apply dressed states with large Autler-Townes splittings for resonantly enhanced harmonic generation in the high intensity regime. We applied control intensities of up to $I_C \approx 7$ TW/cm² corresponding to a Keldysh parameter of $\gamma \approx 4$. The experi-

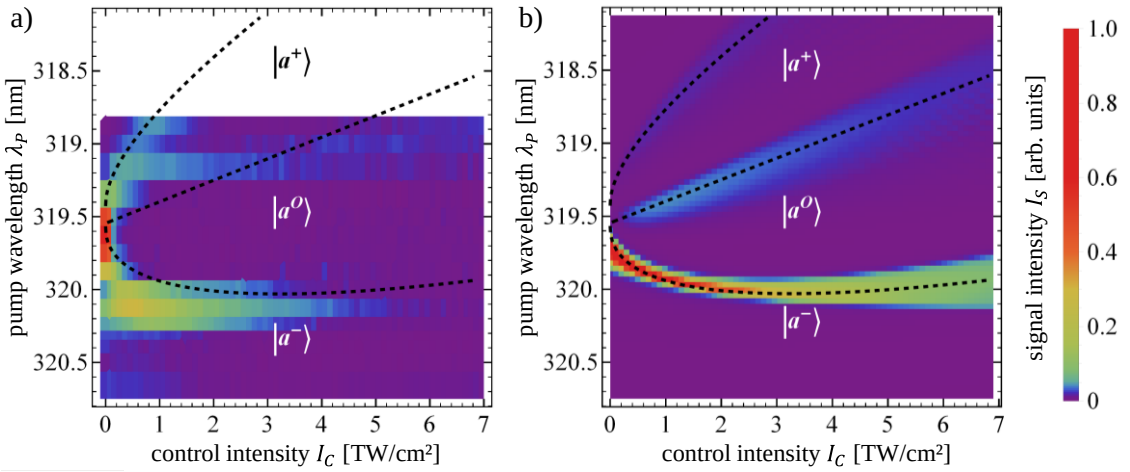

Figure 3.7 a) THG signal intensity in argon versus control intensity and pump wavelength. The pump intensity is set to $I_P = 1$ TW/cm², the control laser is red detuned with a wavelength of $\lambda_C = 811.9$ nm. Black dashed lines indicate numerically simulated dressed state energies. Pump and control polarization are perpendicular to each other. b) Numerical simulation of the THG signal intensity, based on the theoretical treatment presented above. For details see subsection 3.3.4. We neglected ionization for simplicity. The main goal of the measurement was to show that we can invert the strength of the dressed states and to check, whether we can achieve a total enhancement via the dressed state. That is why we unfortunately did not cover the complete spectral region in the experimental data.

mental data are still well described at such high intensities by the numerical simulation based on nonlinear optics in coherently-driven quantum systems. Further, we verified the possibility to control the strength and energetic position of the dressed states by the control laser detuning and intensity. For an originally off-resonant wavelength, we demonstrated an enhancement via a dressed state resonance of 80. Moreover, we studied a more complicated level structure with three dressed states, which is quite likely in other level schemes at these high Rabi frequencies (off-resonant couplings of some THz detunings are coupled strongly at Rabi frequencies of some tens of THz).

3.3.4 Numerical simulation

The basic concept of THG via dressed states (see Fig. 3.1), requires a three-state Hamiltonian only. However, we include in our simulation another fourth, highly excited, state to account for the additional coupling (see Fig. 3.4). Thus, for the four-level scheme, the Hamiltonian in Dirac representation with dipole and rotating wave approximation reads [34]:

$$\hat{\mathrm{H}}(t) = \frac{\hbar}{2}\begin{pmatrix} -2\Delta_P^{(3p)} - 2S(t) & \Omega_P^{(3p)}(t) & 0 & 0 \\ \Omega_P^{(3p)^*}(t) & 0 & \Omega_C(t) & 0 \\ 0 & \Omega_C^*(t) & 2\Delta_C & \Omega_{\tilde{C}}(t) \\ 0 & 0 & \Omega_{\tilde{C}}^*(t) & 2\Delta_C + 2\Delta_{\tilde{C}} \end{pmatrix} \tag{3.3}$$

with the three-photon pump Rabi frequency $\Omega_P^{(3p)}$, the single-photon control Rabi frequency Ω_C, the three-photon pump detuning $\Delta_P^{(3p)}$, the single-photon control detuning Δ_C, and the time dependent ac Stark shift S. In the lower right corner the Hamiltonian includes the additional coupling to the fourth level, with the Rabi frequency $\Omega_{\tilde{C}}$ and the detuning offset $\Delta_{\tilde{C}}$,. For an ideal three-level scheme $\Omega_{\tilde{C}}$ and $\Delta_{\tilde{C}}$ would be both zero (compare section 3.2).

In the simulations, we used the following measured laser pulse parameters: pulse durations (FWHM) $t_P = 2$ ps, $t_C = 4$ ps and beam diameters ($1/e^2$ of intensity) $d_P = 36\,\mu$m and $d_C = 40\,\mu$m. The Hamiltonian involves a larger number of parameters, e.g., transition moments that occur in Rabi frequencies, which are only partly available from literature. Hence, we required some reasonable estimations and fits of parameters. The three-photon pump Rabi frequency is expected to be very small, i.e., we estimated $\Omega_P^{(3p)}\tau_P \ll 1$, due to the huge detunings of the pump laser from any single-photon resonance between the ground state and excited states. Hence, exact choice of $\Omega_P^{(3p)}$ only changes the peak value of the THG signal, but does not effect the line shapes obtained from the simulation. For the control Rabi frequencies, we fitted transition dipole moments to match with the experimentally observed Autler-Townes splittings. We found $\mu_C = 2.125 \cdot 10^{-30}$ Cm and $\mu_{\tilde{C}} = 1.446 \cdot 10^{-30}$ Cm. The fit of the transition moment differs roughly by an order of magnitude from literature values [89]. The control wavelength is $\lambda_C = 801.25$ nm or $\lambda_C = 811.9$ nm, the transition wavelengths are $\lambda_{23} = 805.5$ nm and $\lambda_{34} = 803.7$ nm. The ac Stark shift S varies proportional to the pump and control intensity, with a peak value approximated by the ponderomotive energy ϕ. For

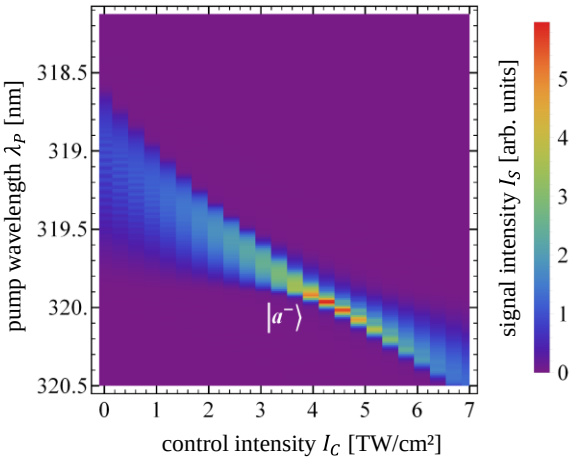

Figure 3.8: Numerical simulation of THG signal intensity to demonstrate the possible enhancement via the dressed state approach. The THG signal intensity is normalized to the maximal signal without the control laser. We applied a pump intensity of $I_P = 5\ TW/cm^2$, so five times larger than in the above cases. Hence, the pump induced ac Stark shift is as well five times larger. The control transition moment is assumed to be $\mu_C = 6 \cdot 10^{-30}\ Cm$. We neglected the control ac Stark shift and the coupling to state $|4\rangle$, but we included spatial and temporal averaging effects.

the total ac Stark shift, we add the ponderomotive energy induced by the pump and the control laser. We used the approximation $\hbar S = \phi$ for the pump-induced shift. As an exception, by comparison of the experimental data with our simulation, we found that the control-induced shift was only 12 % of the calculated ponderomotive shift (which we attribute to contributions of other excited states to the net ac Stark shift).

3.3.5 THG enhancement with regard to resonant excitation

So far, we discussed the possible dressed state resonance enhancement with a control laser for an originally off-resonant pump laser. However, we want to stress from our findings with the numerical simulation that it is possible to enhance the third-harmonic above the originally resonant case without the control laser. Key parameters for an enhancement are, first, that the ac Stark shift of the pump is perturbing harmonic generation strongly, and second, a large red detuning for the control laser, so the ac Stark shift compensated dressed state $|a^-\rangle$ is strong. Figure 3.8 shows a simulation for a far red detuned control wavelength of $\lambda_C = 912$ nm. We observe only one dressed state ($|a^-\rangle$) in the depicted spectral pump regime, as dressed state $|a^+\rangle$ appears at about $\lambda_P = 314$ nm. The enhancement via dressed state $|a^-\rangle$ above the resonant case without the control laser reveals that the control laser induced Autler-Townes splitting can compensate for the inevitable ac Stark shift of the pump laser. The ac Stark shifts cause broadening of the resonance enhancement structure due to temporal and spatial averaging and consequently a reduced THG signal. Comparing the width of the dressed state $|a^-\rangle$ without and with the control laser (at $I_C \approx 4$ TW/cm²), we see that it is much narrower with the control laser. Hence, the control laser compensates for the broadening of the resonance enhancement due to the ac Stark shift. The compensation enables a five times higher harmonic signal. Note that we observe the highest enhancement with the control laser, when the dressed state $|a^-\rangle$ crosses the unperturbed three-photon resonance at $\lambda_P = 320$ nm. The simulation demonstrates that a dressed state resonance enhancement outperforms the bare state resonance enhancement, which is perturbed by ac Stark shifts. However, it will be difficult to implement this experimentally due to much more complicated coupling schemes and loss channels induced by the control laser.

3.4 Higher-order far-off-resonant harmonic generation

The THG spectroscopy experiments in argon with a tunable pump laser mainly served to confirm the formation of dressed states, and to verify control of their energetic positions by the control laser intensity and detuning, even if large ac Stark shifts occur. It already demonstrated the potential of the dressed state approach to enhance THG of high intensity, ultrafast laser pulses. We performed experiments in a second coupling scheme with a more typical setup for higher-order harmonic generation, i.e., with a fixed-frequency pump laser to drive frequency conversion and towards multiple harmonic orders. We apply now a tunable control laser to push one of the dressed states into resonance. We address the following questions experimentally: How large is the resonance enhancement via dressed states with large Autler-Townes splittings for a far detuned pump laser and how large are the Autler-Townes splittings at multiple TW/cm²? Do the dressed states effect harmonic generation at higher orders?

3.4.1 Level scheme

We implemented the experiments in xenon and detected THG and FHG. Figure 3.9 shows the coupling scheme: We apply fixed-frequency pump laser pulses at the second-harmonic of our amplified Ti:Sa laser ($\lambda_P = 400.6$ nm, later $\lambda_P = 399.1$ nm). The pump laser is far red detuned from the nearest three-photon resonance, which occurs between the ground state $|1\rangle = 5p^6\,(^1S_0)$ and the excited state $|2\rangle = 5p^5\,6s'\,^2[1/2]_1$ ($\lambda_{12} = 388.7/3$ nm). The three-photon pump detuning is $\Delta_P^{(3p)}/2\pi = -69$ THz, hence much larger than the picosecond laser pulse bandwidth of roughly 1 THz. The control laser, which is the amplified pulse of the OPO/OPA setup, is broadly tuned in the vicinity of single-photon resonances between state $|2\rangle$ and the manifold of higher excited states $|3\rangle$ in the interval between $\lambda_{23} = 618 - 789$ nm[1]. As discussed above, when the control laser hits a resonance $|2\rangle \rightarrow |3\rangle$ in the latter manifold, dressed states $|a^{\pm}\rangle$ appear below and above the initial bare state $|2\rangle$. Appropriate choice of the control intensity and wavelength (detuning) shifts the dressed state $|a^-\rangle$ into three-photon resonance with the pump laser (initially far red detuned with respect to the bare state $|2\rangle$, compare also Fig. 3.1 b)) and enhances the harmonic generation signal. Here it is beneficial to use a far blue detuned control laser, so that the dressed state $|a^-\rangle$ appears at the three pump photon energy, i.e., $\Delta_P^{(3p)} = -\Delta_C$. With that we conclude, that the main excited states are state $|3\rangle = 5p^5\,4f\,^2[3/2,5/2]_{1,2}$ at $\lambda_{23} = 728 - 732$ nm.

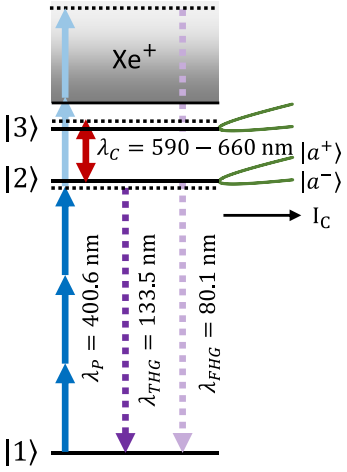

Figure 3.9: Coupling scheme in xenon.

[1] $|3\rangle = \{5p^5\,5f\,^2[3,5/2]_{1,2}; 5p^5\,8p\,^2[1,3,5/2]_{0,1,2}; 5p^5\,4f\,^2[3,5/2]_{1,2}; 5p^5\,6p'\,^2[1/2]_0\}$

3.4.2 Experimental setup

We apply the frequency-doubled output of the first beamline with the regenerative amplifier as fixed-frequency pump beam ($\lambda_P = 400.6$ nm or 399.1 nm), and the visible radiation from the second beamline with the OPO/OPA as frequency-tunable control beam ($\lambda_C = 590 - 665$ nm). We generate the second-harmonic of the pulses from the regenerative amplifier in a nonlinear crystal (BBO, dimensions: 6 mm x 6 mm x 1.6 mm, cut angle 30°, protective coating) and separate it from the fundamental radiation by a dichroic mirror. We apply pump laser pulses with an energy of up to 40 μJ, which we overlap with the control beam (pulse energy up to 60 μJ) by a dichroic mirror and focus both by a lens (here $f = 200$ mm) to beam diameters of $d_P = 50\,\mu$m and $d_C = 50\,\mu$m ($1/e^2$ of intensity). We chose the beam diameter of the control similar to the pump beam diameter, so that we obtain a relatively homogeneous control field for the pump radiation. We had to make a compromise between homogeneity of the control field and its maximum intensity. Note that here the pump pulse is with $\tau_P = 3$ ps longer than the control pulse with $\tau_C = 2$ ps. The stagnation pressure at the pulsed gas nozzle, which generates the gas jet, was $p = 200$ mbar xenon. The pressure dependence was quadratically in this stagnation pressure regime.

3.4.3 Experimental results

THG enhancement for a far-off-resonant pump laser via dressed states: Figure 3.10 a) shows the experimental enhancement of the THG signal intensity versus the control intensity and wavelength or detuning. We observe two peaks (labelled by indices A, B), which indicate dressed states $|a^-\rangle$ emerging due to couplings of state $|2\rangle$ with two separate bare states (or closely spaced triplet) in the manifold $|3\rangle$. The strongest feature $|a_A^-\rangle$ corresponds to the formation of a dressed state $|a^-\rangle$ via interaction with the closely spaced triplet of bare states $5p^5\,4f\;{}^2[3/2,5/2]_{1,2}$. The bare state resonances of the triplet are expected (without ac Stark shifts) in the wavelengths interval $\lambda_{23} = 728 - 732$ nm. The intersection of $|a_A^-\rangle$ with the wavelength axis in Fig. 3.10 a) (i.e., for the control laser switched off) is at $\lambda_C = 620$ nm. Hence, the control laser is far blue detuned with $\Delta_C/2\pi = 70$ THz. The Autler-Townes splitting is asymmetric in this case. The detuning matches very well with the three-photon pump detuning ($\Delta_P^{(3p)} \approx -\Delta_C$), i.e., the dressed state $|a^-\rangle$ is in multi-photon resonance with the pump laser. At small control intensity (i.e., small Rabi frequency), the dressed resonance is weak. For increasing control intensity the relative strength and, hence, the third-harmonic enhancement significantly increases, as the ratio between the control Rabi frequency and the control detuning changes. We also observe with increasing control intensity a clearly linear ac Stark shift of the THG maxima along $|a_A^-\rangle$. The magnitude of the shift is roughly 6 THz per TW/cm². This is, as expected for the highly excited states, close to the ponderomotive energy, which yields roughly

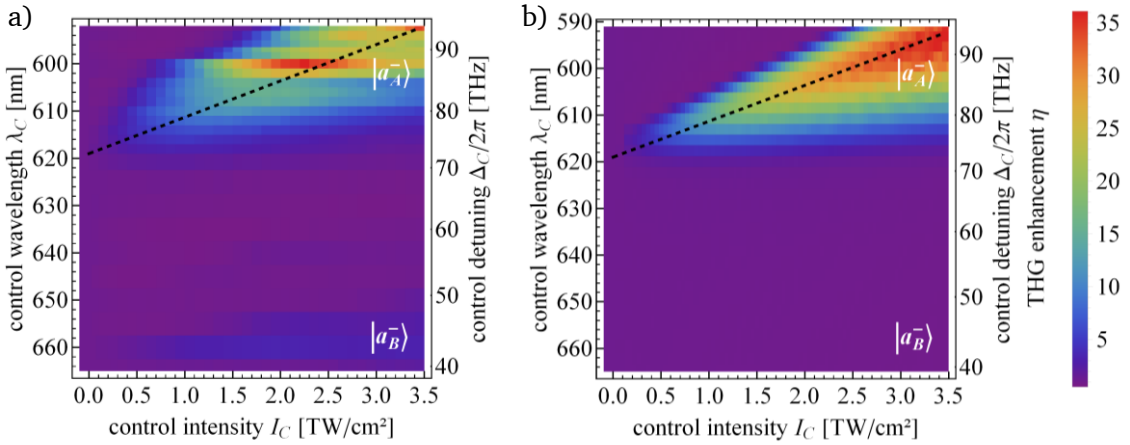

Figure 3.10: a) THG enhancement versus control intensity and control wavelength (left axis) or control detuning (right axis). The THG enhancement η is defined as the ratio of the THG yield with and without control laser. The pump intensity is set to $I_P = 1.4$ TW/cm², the pump wavelength is $\lambda_P = 400.6$ nm. The maximal control intensity corresponds to a Keldysh parameter of $\gamma = 7$. The black dashed line indicates the numerically simulated dressed state energy. b) Numerical simulation of the third-harmonic enhancement, based on the theoretical treatment presented above. For simplicity we neglected ionization and dressed state $|a_B^-\rangle$. For details on the simulation see Appendix C. Note the same color scale for both plots.

$S/2\pi = 8$ THz per TW/cm² (for the control laser). The ac Stark shift effectively increases the three-photon pump detuning. Therefore, the control detuning must increase to push dressed state $|a_A^-\rangle$ into three-photon resonance with the pump laser. At $\lambda_C = 592$ nm and $I_C = 3.5$ TW/cm² this corresponds to an Autler-Townes splitting of roughly $\bar{\Omega}_C/2\pi = 100$ THz. Thus, the Autler-Townes splittings in xenon are much larger compared to our spectroscopic investigation in argon. This offers a large wavelength range for an application of the dressed state approach to enhance harmonic generation in xenon. The extension of the region of large enhancement is in the order of 10 nm, which corresponds to a spectral bandwidth of roughly 10 THz in the visible regime. This covers the bandwidth also of shorter (fs) pulses, which are typically applied for harmonic generation at higher orders. Hence, the dressed resonance approach will also work for (fs) lasers, though somewhat smaller enhancements will be expected for very short pulses with very large bandwidth. The maximal THG enhancement, which we obtain from Fig. 3.10 a), is roughly $\eta \approx 37$. Hence, preparation and intensity-control of the dressed state enables a substantial gain in THG. We note, that the faint peak $|a_B^-\rangle$ in Fig. 3.10 a) is due to a weaker transition from the intermediate state $|2\rangle$ to state $5p^5\ 6p'\ ^2[1/2]_0$. The behavior is similar to $|a_A^-\rangle$, but yields smaller enhancement by a factor of 3, which is due to weaker transition moment and nonlinear susceptibility.

We now compare the experimental results to a numerical simulation shown in Fig. 3.10 b). We observe in the simulation only one peak, which indicates dressed state $|a_A^-\rangle$ emerging due to the coupling of state $|2\rangle$ with the closely spaced triplet in the manifold $|3\rangle$. The simulation is based on a simple three-level system, hence we can only observe dressed state $|a_A^-\rangle$ and not dressed state $|a_B^-\rangle$. We see that the energetic position of the dressed state $|a_A^-\rangle$ fits quite well to the experimental data. The width of the dressed state $|a_A^-\rangle$ is similar in both plots. The enhancement of THG is almost the same in experiment and simulation (note that we apply the same scale of the enhancement). Hence, the simulation is in very good agreement with the experimental data. We see that the theoretical description of THG enhanced by coherent preparation of dressed states works well for large detunings ($\Delta_P^{(3p)}/2\pi = -69$ THz), large effective Rabi frequencies ($\bar{\Omega}_C/2\pi = 100$ THz) at intensities in the TW/cm² regime (corresponding to Keldysh parameter $\gamma \approx 7$).

In the following, we vary experimental parameters, e.g., the polarization, pump intensity and pump detuning in order to get a better understanding of THG via dressed states.

Polarization dependence: We start with a comparison of the THG enhancement for parallel and perpendicular linear polarization of the pump and the control laser. Figure 3.11 a) shows the experimental results for perpendicular polarizations, the experimental results for parallel polarizations are shown in Fig. 3.11 b). First, we notice the different maximal THG enhancements of $\eta = 35$ (parallel polarizations, $\lambda_C = 592$ nm at $I_C = 3.5$ TW/cm²) and $\eta = 7$ (perpendicular polarizations, $\lambda_C = 592$ nm at $I_C = 3.5$ TW/cm² and $\lambda_C = 600$ nm at $I_C = 2.7$ TW/cm²). This difference in enhancement of roughly a factor of five can be seen at almost the whole enhancement structure. Second, we observe, that the enhancement structures itself are similar and the energetic position and the width of the structure fit quite well. The ac Stark shift of the dressed states $|a_A^-\rangle$ in the experimental data is not affected by the change of polarization. Hence, the change from parallel to perpendicular polarization seems to mainly change the enhancement of the THG, without strongly changing the atomic level structure. In the following, we will use parallel polarizations for our experiments in xenon to reach higher enhancements. We have

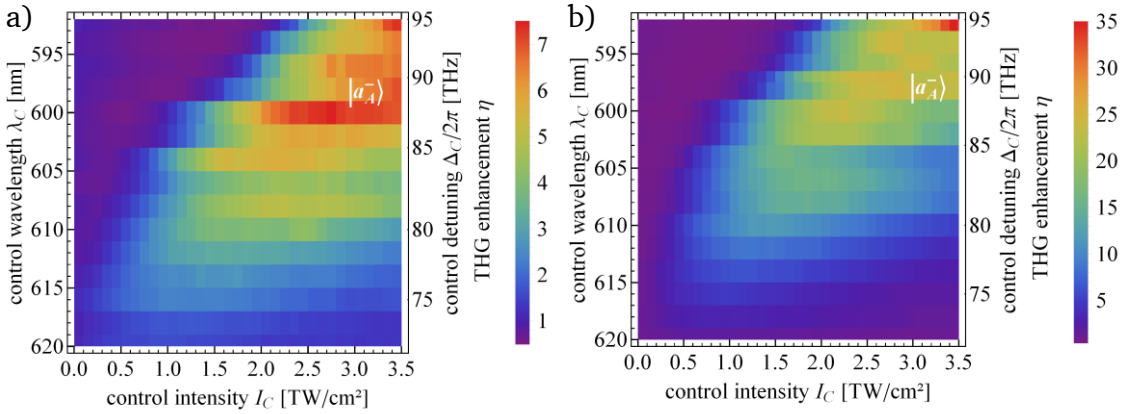

Figure 3.11: Comparison of THG enhancement for a) perpendicular and b) parallel pump and control polarizations. Note the different color scales. We performed the measurements successively with exactly the same alignment and laser pulse parameters.

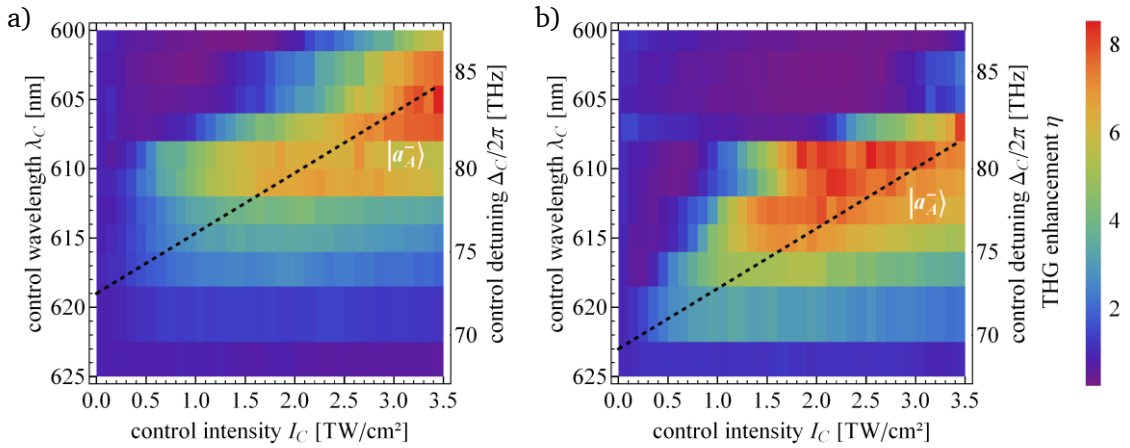

Figure 3.12: Comparison of the THG enhancement structure for different pump laser intensities, a) $I_P = 2$ TW/cm², b) $I_P = 1$ TW/cm². Note the lower THG enhancement in comparison to Fig. 3.10 a) due to a worse alignment in the interaction region. We measured the two data sets successively. The black dashed lines indicate the numerically simulated dressed energy.

a closer look at loss channels in Appendix D (especially frequency mixing channels). For parallel polarization, we observe much stronger frequency mixing signals (sum and difference frequencies of pump and control) than with perpendicular polarization. However, it is not yet clear how the change of polarization effects atomic transitions, ionization and frequency conversion in our level scheme in xenon.

Different pump intensities: In the experimental data discussed above, we observe the ac Stark shift of dressed state $|a_A^-\rangle$ with the control intensity, well described by the ponderomotive energy. Now, we perform the same measurement for two different pump intensities, to investigate the ac Stark shift of the pump laser. The experimental results for a high pump intensity of $I_P = 2$ TW/cm² are shown in Fig. 3.12 a), for a low pump intensity of $I_P = 1$ TW/cm² in Fig. 3.12 b). We observe for both pump intensities dressed state $|a_A^-\rangle$, which is Stark shifted with increasing control laser intensity. However, at the intersection of $|a_A^-\rangle$ with the wavelength axis (i.e., $I_C = 0$) we see that for the high pump intensity ($I_P = 2$ TW/cm²) we get $\lambda_C = 619$ nm , and for the low pump intensity ($I_P = 1$ TW/cm²) we get $\lambda_C = 623$ nm. This change of control wavelength corresponds to a change of the control detuning by 3.1 THz. The change of the ponderomotive energy of the pump laser causes a shift of $S/2\pi = 3.6$ THz (for the peak intensity). Hence, the pump ac Stark shift is well described by the ponderomotive energy.

Smaller pump detuning: To investigate resonantly enhanced harmonic generation via dressed states further, we performed another experiment in xenon with a shorter pump laser wavelength. We changed it from $\lambda_P = 400.6$ nm to $\lambda_P = 399.1$ nm, reducing the three-photon pump detuning from $\Delta_P^{(3p)}/2\pi = -69$ THz to $\Delta_P^{(3p)}/2\pi = -60$ THz. Hence, we expect the optimal control detuning to be smaller in regard to the main control transition at $\lambda_{23} = 728 - 732$ nm, as the dressed state $|a_A^-\rangle$ appears at the energy of three pump photons, i.e., at $\Delta_C = -\Delta_P^{(3p)}$ (for $I_C = 0$). Figure 3.13 a) shows the experimental

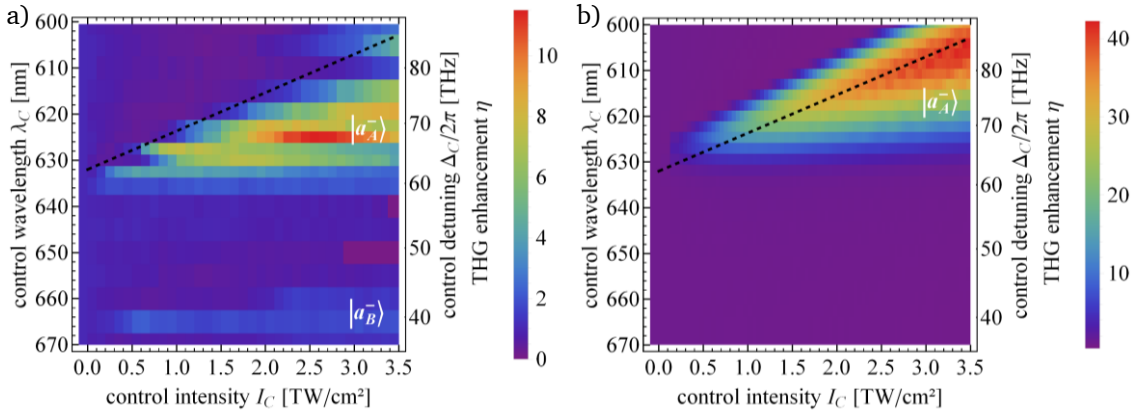

Figure 3.13: a) THG enhancement vs. control intensity and control wavelength (left axis) or control detuning (right axis). The pump intensity is set to $I_P = 0.2$ TW/cm², the pump wavelength is $\lambda_P = 399.1$ nm. The black dashed line indicates the numerically simulated dressed energy. At a control wavelength of $\lambda_C = 650$ nm we only reached a control intensity of up to $I_C = 3$ TW/cm², at $\lambda_C = 640$ nm we were limited to $I_C = 3.4$ TW/cm². b) Numerical simulation of the THG enhancement, based on the theoretical treatment presented above for $I_P = 1.4$ TW/cm². For details on the simulation, see Appendix C. For simplicity we neglected ionization and dressed state $|a_B^-\rangle$. Note the different color scales.

data of the THG enhancement for a pump laser wavelength of $\lambda_P = 399.1$ nm. We observe again two peaks of enhanced THG, which we identify as dressed states $|a_A^-\rangle$ and $|a_B^-\rangle$. In comparison to the above experiment with $\lambda_P = 400.6$ nm (Fig. 3.10 a)), we see that the dressed state $|a_A^-\rangle$ has a constant control detuning offset of roughly 15 THz, as expected, to smaller control detunings and longer control wavelength. However, the magnitude of the shift is slightly larger than one would expect from simple comparisons to the three-photon pump detuning (change of 9 THz). One reason is the change of pump intensity from $I_P = 1.4$ TW/cm² (above case, $\lambda_P = 400.6$ nm) to $I_P = 0.2$ TW/cm² (this case, $\lambda_P = 399.1$ nm). This changes the ponderomotive energy and consequently the ac Stark shift of the pump laser by roughly 4 THz. Further, the increase of the control wavelength itself leads to a higher control ac Stark shift of roughly 1 THz. Hence, the expected shift of dressed state $|a_A^-\rangle$ sums up to 14 THz, and fits well to the observed 15 THz shift. Another difference between the two measurements with the different pump wavelengths and detunings is the THG enhancement (see different scales, maximal enhancement of $\eta = 37$ (Fig. 3.10 a)) versus $\eta = 11$ (Fig. 3.13 a))). Due to a worse beam overlap, we did not achieve similar enhancements as in Fig. 3.10 a).

Figure 3.13 b) shows the numerical simulation for a pump wavelength of $\lambda_P = 399.1$ nm and a pump intensity of $I_P = 1.4$ TW/cm². We observe one peak corresponding to dressed state $|a_A^-\rangle$. Again, we do not observe dressed state $|a_B^-\rangle$ as we only assume a simplified three-level system. The comparison to the experimental data in Fig. 3.13 a) shows that the width and the shift of dressed state $|a_A^-\rangle$ are well described by the simulation, but the energetic position differs slightly. This is mainly due to the different pump intensities between experiment and simulation. We chose for the simulation the same pump intensity as for the simulation

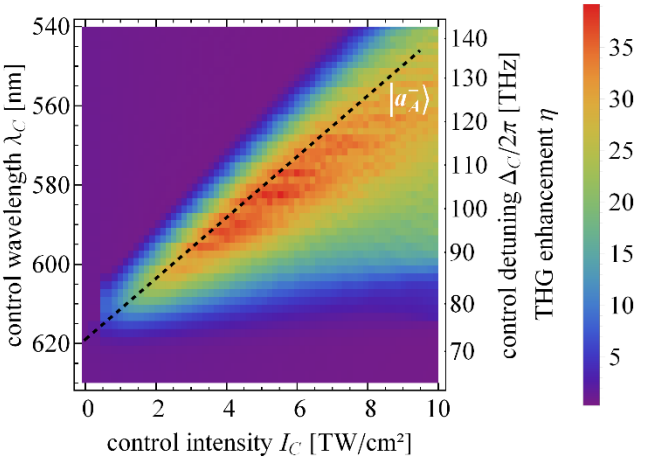

Figure 3.14: Numerical simulation of the THG enhancement vs. the control intensity and wavelength (left axis) or detuning (right axis). Note that we adjusted the control intensity and wavelength range in order to demonstrate the optimal conditions for enhanced THG via dressed state $|a_A^-\rangle$. For details on the simulation see Appendix C. For simplicity we neglected ionization and dressed state $|a_B^-\rangle$.

with a pump wavelength of $\lambda_P = 400.6$ nm (Fig. 3.10 b)), for a better comparison. Hence, the simulation (Fig. 3.13 b)) describes the measurement data (Fig. 3.13 b)) quite well, except for the THG enhancement ($\eta_{sim} = 42$ versus $\eta_{exp} = 11$). The difference in the THG enhancement is caused by a worse beam overlap in the experiment. In contrast, the comparison of the two simulations for the two different pump wavelength (Fig. 3.10 b) and Fig. 3.13 b)) shows that we expect slightly higher enhancements for the lower pump laser detuning ($\eta = 42$ versus $\eta = 37$).

In the following we address two questions with the simulation: What is the maximal enhancement for a far detuned pump laser - which is the typical case, e.g., in a high-harmonic generation experiment? How do the dressed states vary with the pump wavelength for large control detunings?

Simulation of enhancement for higher intensities: We start with the simulation investigating the maximal enhancement for the longer pump wavelength $\lambda_P = 400.6$ nm. As we saw in Fig. 3.10 b), the maximal enhancement is reached at the maximum control intensity of $I_C = 3.5$ TW/cm². Therefore, we performed a simulation to check the enhancement at even higher control intensities ($I_C = 10$ TW/cm², Keldysh parameter $\gamma = 4$). Figure 3.14 shows the results of the numerically simulated THG enhancement versus the control intensity and wavelength. The maximal enhancement is only slightly higher than in Fig. 3.10 b), as the maximum is reached at a control intensity of about $I_C = 4$ TW/cm². However, we can see a change of the width of dressed state $|a_A^-\rangle$. After reaching the maximal enhancement at about $I_C = 3$ TW/cm² with a FWHM of about 10 THz, the width increases to about 40 THz at $I_C = 8$ TW/cm². Even though this is no advantage for our picosecond laser pulses, this broad enhancement structure can even support short femtosecond pulses down to $\tau = 10$ fs (estimation from the time bandwidth product: $\Delta\tau\Delta\nu = 10\text{ fs} \cdot 40\text{ THz} = 0.4$, which is in the range for a Gaussian pulse shape (0.441) or sech² (0.315)). In other words, the perturbing averaging effects become large for higher control intensities, but they enable an almost constant enhancement in a broad spectral regime. However, this enhancement is not uniform across the beam profile because of the intensity dependent Autler-Townes splitting and ac Stark shifts. Consequently, we already observed quite optimal resonantly enhanced harmonic generation via dressed states in the far detuned pump case.

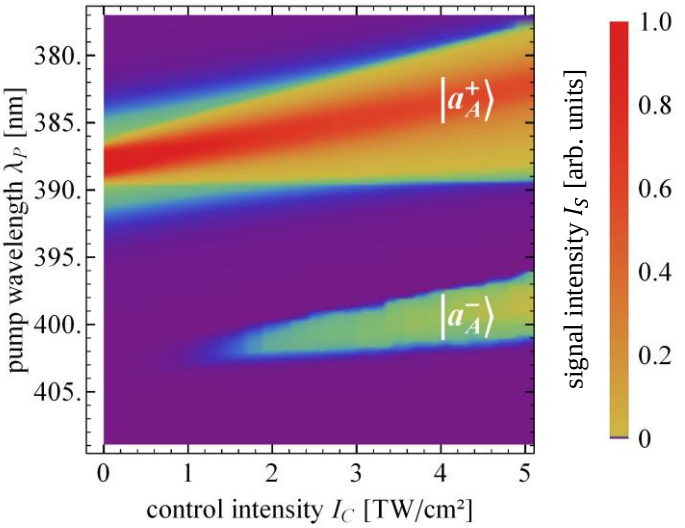

Figure 3.15: Numerical simulation of THG signal intensity versus control intensity and pump wavelength, based on the theoretical treatment presented above for our level scheme in xenon. For details on the simulation see Appendix C. The control wavelength is $\lambda_C = 600$ nm. The yellow section of dressed state $|a_A^-\rangle$ has 1 % strength of the original resonance enhancement at $\lambda_P = 388.7$ nm.

Simulation of THG signal versus pump wavelength at high control detunings: The second simulation to understand the optimal conditions for resonantly enhanced harmonic generation via dressed states with large Autler-Townes splittings is analogous to our spectroscopic investigations in section 3.3. Figure 3.15 shows the results of the numerical simulation for our level scheme in xenon. We can clearly identify two dressed states $|a_A^+\rangle$ and $|a_A^-\rangle$. Due to the large control laser detuning, dressed state $|a_A^+\rangle$ is much stronger than dressed state $|a_A^-\rangle$, even at large control laser intensities of up to $I_C = 5$ TW/cm² (so also in the experiments shown above with a control laser intensity up to $I_C = 3.5$ TW/cm²). Let us now compare the control Rabi frequency with the control detuning of $\Delta_C/2\pi = 88$ THz. At a peak intensity of $I_C = 1$ TW/cm², we have a control Rabi frequency of $\Omega_C = 30$ THz ($\mu_C = 7 \cdot 10^{-30}$ Cm), and at $I_C = 5$ TW/cm², we have a control Rabi frequency $\Omega_C = 65$ THz. Hence, even at high control intensities the control detuning dominates or is roughly equal to the control Rabi frequency. Therefore, dressed state $|a_A^+\rangle$ is much stronger than dressed state $|a_A^-\rangle$. However, a significant enhancement of the THG is still possible via dressed state $|a_A^-\rangle$. The change of the energetic positions of the dressed states is almost linear dependent on the control intensity even up to intensities of $I_C = 5$ TW/cm². Both dressed states shift roughly with the ponderomotive energy to lower pump laser wavelengths and we do not observe a strong increase of the Autler-Townes splitting. The dressed state $|a_A^-\rangle$ is shifted into resonance (at $\lambda_P = 400.6$ nm) at a control intensity of about $I_C = 3$ TW/cm², as we observed it in Fig. 3.10 b). The spectroscopic investigation for our level scheme in xenon revealed the completely asymmetric Autler-Townes splitting, which still enables significant resonance enhancements for a far detuned pump laser.

3.4.4 Enhancement for higher harmonic orders

To study the dressed resonance enhancement in some more detail and also for a higher-order conversion process, we measured the signal intensity of THG and FHG simultaneously, while varying the control intensity for a fixed control wavelength. In principle, we expect a similar behavior of THG and FHG, as both processes are driven via the same dressed three-photon resonance. However, the two

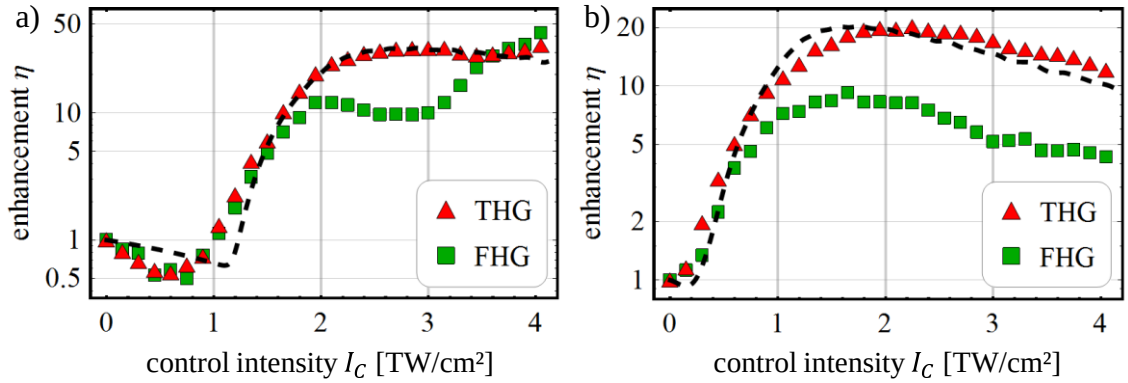

Figure 3.16: Enhancement of the THG and FHG signal intensity vs. control intensity. The control wavelength is kept fixed at a) $\lambda_C = 597$ nm or b) $\lambda_C = 608$ nm. Data points indicate experimental data, black dashed lines show numerical simulations for THG. Note the logarithmic scale for the enhancement.

additional photons in FHG drive additional near resonant couplings to highly excited states, autoionizing states and the ionization continuum, which will cause some modifications compared to THG. Figure 3.16 shows the results of the experiments for two different control wavelengths. Without the control laser (i.e., at $I_C = 0$), we get only weak THG and FHG signals. At an appropriate control intensity (i.e., for $\lambda_C = 597$ nm at $I_C = 3$ TW/cm², for $\lambda_C = 608$ nm at $I_C = 2$ TW/cm²) the dressed state $|a_A^-\rangle$ is driven into three-photon resonance with the pump field. Both THG and FHG yield increase substantially in this case. We get enhancements beyond a factor of 30 for THG, and around an order of magnitude for FHG. Hence, also the higher-order process benefits from the lower order resonance. For THG we performed numerical simulations (see black dashed lines in Fig. 3.16), which fit well to the experimental data. As we had only limited laser power available in the experiment, we could not observe the full rollover across the resonance for higher intensities. FHG shows a similar behavior, although we observed a difference in the enhancements starting at about $I_C = 1 - 2$ TW/cm². We attribute the second maximum of the FHG enhancement at $I_C = 3 - 4$ TW/cm² (Fig. 3.16 a)) to a Stark shifted four-photon resonance with the autoionizing states $5p^5\,7p'$. This further boosts the FHG enhancement towards a total factor of 43. The data clearly demonstrate that the dressed state resonance also works for a higher-order conversion process, i.e., FHG in our case. An interesting feature of Fig. 3.16 a) is the initial decrease of enhancement (attenuation of THG/FHG) for low control intensities. Here we observe that the excited state $|2\rangle$ is Stark shifted away from the three-photon pump energy. Only due to the dressed state $|a_A^-\rangle$ we can achieve a change of the slope. Hence, for a three-photon pump detuning larger than the negative control detuning $\Delta_P^{(3p)} > -\Delta_C$, we only expect an attenuation of the THG/FHG with the control laser.

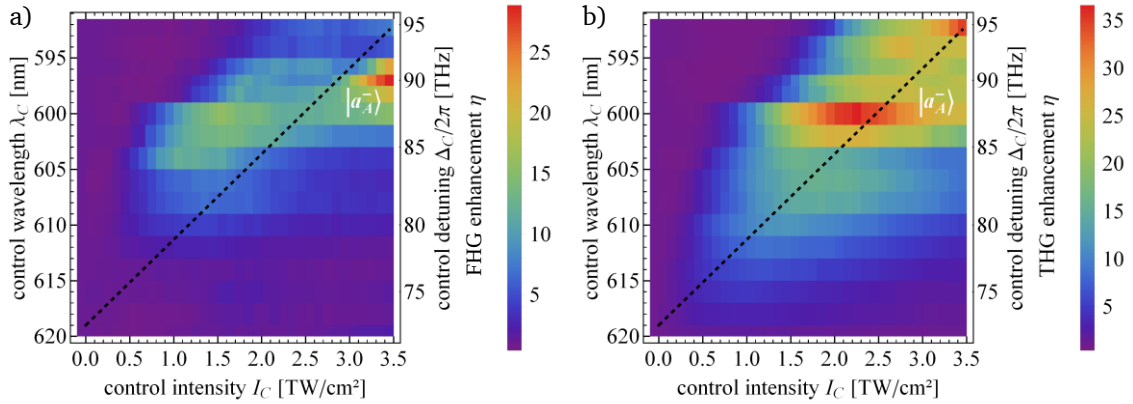

Figure 3.17: a) Fifth-harmonic enhancement vs. control intensity and control wavelength (left axis) or control detuning (right axis). The pump intensity is set to $I_P = 1.4$ TW/cm², the pump wavelength is $\lambda_P = 400.6$ nm. The black dashed line indicates the numerically simulated dressed state energy from Fig. 3.10 b) for THG. b) THG enhancement vs. control intensity and control wavelength (left axis) or control detuning (right axis). Note the different color scales.

To compare THG and FHG in more detail spectroscopically, we show both enhancements versus control wavelength and intensity in Fig. 3.17. The main structure of enhancement for THG (dressed state $|a_A^-\rangle$) is resembled well by the measurement data of FHG. However, as we saw already in Fig. 3.16 a), there is a further enhancement structure at $\lambda_C = 600$ nm and $I_C \geq 3$ TW/cm², which leads to substantial enhancement of FHG. We observed an enhancement of FHG as well in the case of perpendicular polarizations between the pump and the control, but the FHG enhancement was lower. Nevertheless, the spectroscopic data confirm the simultaneous enhancement for higher harmonic orders and demonstrate the applicability of the dressed resonance approach for higher-order harmonic generation at high intensities.

3.5 Dressed state enhanced harmonic generation, driven by a single pump laser

The scheme for dressed state enhanced harmonic generation, as discussed above, requires a control laser in addition to the pump laser, which drives the frequency conversion process. This increases the experimental effort and, depending on the laser setup, reduces the available pulse energy for the pump pulse, which may lead to lower total conversion efficiencies. However, ultrashort laser systems often provide several beam lines at different wavelength anyway, e.g., residual pump or idler radiation from an OPA. Such residual radiation can be applied at no additional costs to provide control pulses and enhancements via dressed states. Moreover, as we present in this section, appropriate level schemes permit the generation and application of dressed states also with a single pump laser alone. In this scheme, the pump laser generates appropriate Autler-Townes splittings itself and shifts them into multi-photon resonance. This has been studied at high intensities theoretically [29], but has not be confirmed yet experimentally.

3.5.1 Level scheme

We performed the single laser experiment on resonantly enhanced harmonic generation via dressed states in xenon. The coupling scheme is shown in Fig. 3.19. The pump laser is tunable in the vicinity of the five-photon resonance from the ground state $|1\rangle = 5p^6\,(^1S_0)$ to the excited, intermediate state $|2\rangle = 5p^5\,6s'\,^2[1/2]_1$ (transition wavelength $\lambda_{12} = 129.6\,\text{nm} = 647.8\,\text{nm}/5$). Note, this is the same transition as in section 3.4, but now driven by five instead of three photons. Further, the five-photon pump detuning is much smaller than the three-photon pump detuning in the above case. The pump laser also induces couplings between the excited state $|2\rangle$ and again a manifold of states $|3\rangle$ in the interval between $\lambda_{23} = 618 - 789\,\text{nm}$[1]. Due to the manifold, the Autler-Townes splittings are complicated. Further, due to the single laser approach the independent investigation of the effect of parameters like the control intensity is not possible. In the experiment, we also observed seventh-harmonic generation (7HG). In this case, we are close to five-, six- and seven-photon resonances (the seventh photon couples to autoionizing states in xenon).

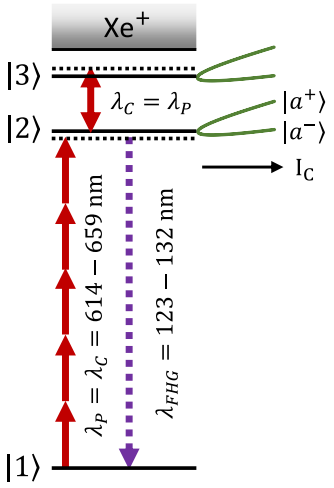

Figure 3.18: Coupling scheme for FHG in xenon, driven by a single pump laser.

3.5.2 Experimental setup

The experimental setup for the single laser experiment requires a single laser pulse only, which we generate from the second beamline with the OPO/OPA of our setup. To emphasize the double aim of the single laser pulse to drive both the frequency conversion via a multi-photon transition and formation of dressed states via single-photon coupling of excited states, we will use the term "pump/control pulse" in this section. The wavelength of the pump/control pulses is $\lambda_{P/C} = 614 - 659\,\text{nm}$. We apply pulse energies of up to $E_{P/C} = 60\,\mu\text{J}$ and focus them by a lens (here $f = 200\,\text{mm}$) to beam diameter of $d_{P/C} = 40\,\mu\text{m}$ ($1/e^2$ of intensity). The stagnation pressure at the pulsed gas nozzle, which generates the gas jet, was $p = 700$ mbar xenon. We applied the high stagnation pressure to generate a higher signal level, because the FHG efficiency with roughly $\lambda_{P/C} = 640\,\text{nm}$ is much smaller than the THG efficiency with roughly $\lambda_P = 400\,\text{nm}$. The pressure dependency of the FHG differs from the quadratic dependency at roughly $p = 350\,\text{mbar}$, but still rises for higher pressures up to $p = 1000\,\text{mbar}$. We confirmed, that phase matching issues play no role, so the discrepancy might come from cluster formation in the gas jet, typical for this pressure regime in xenon [65]. Hence, the higher stagnation pressure is still suitable for a spectroscopic experiment.

[1] $|3\rangle = \{5p^5\,5f\,^2[3,5/2]_{1,2};\ 5p^5\,8p\,^2[1,3,5/2]_{0,1,2};\ 5p^5\,4f\,^2[3,5/2]_{1,2};\ 5p^5\,6p'\,^2[1/2]_0\}$

3.5.3 Experimental results

We start our investigations on the single laser approach with a spectroscopic measurement of FHG, which we compare to a numerical simulation later. The measurement data of the FHG versus the pump/control intensity and the pump/control wavelength are shown in Fig. 3.20 a). First, we observe a variety of peaks at high pump/control intensities of about $I_{P/C} \approx 4$ TW/cm². On the first glance, this seems surprising, as there is only one bare state resonance in this spectral regime for FHG. Due to limited signal-to-noise-ratio, we require intensities beyond $I_{P/C} > 1.5$ TW/cm² for a detectable signal in FHG. Hence, we cannot investigate the spectrum at low pump/control intensities in detail. The expected, unperturbed bare state resonance is at $\lambda_{P/C} = 647.8\,\text{nm}/5$ (indicated by the red arrow). We do not observe any strong resonance enhancement there, also for higher pump/control intensities (i.e., if we consider a Stark shifted resonance with the ponderomotive energy, compare black dashed lines). There is a small peak at the pump/control wavelength of $\lambda_{P/C} \approx 640$ nm at $I_{P/C} \approx 4$ TW/cm², but it is much weaker than the peaks next to it. Hence, we identify the two larger areas of resonance enhancement as dressed states $|a^+\rangle$ and $|a^-\rangle$. The dressed states appear roughly 10 nm detuned of the bare state resonance. This offset of 10 nm in the visible spectral regime corresponds to a frequency offset of roughly 10 THz, which sums up to an offset of 50 THz for a five-photon transition. Thus, we observe huge level shifts, but cannot directly analyze the spectral width of the Autler-Townes splittings due to the single laser experiment.

Due to the manifold of state $|3\rangle$, the Autler-Townes splittings are more complicated and the dressed states show a substructure (especially dressed state $|a^+\rangle$). At dressed state $|a^+\rangle$ we can identify two major structures (indicated by the two black dashed lines) and three smaller peaks. Hence, we conclude, that there are at least five control transitions, which effect the level structure.

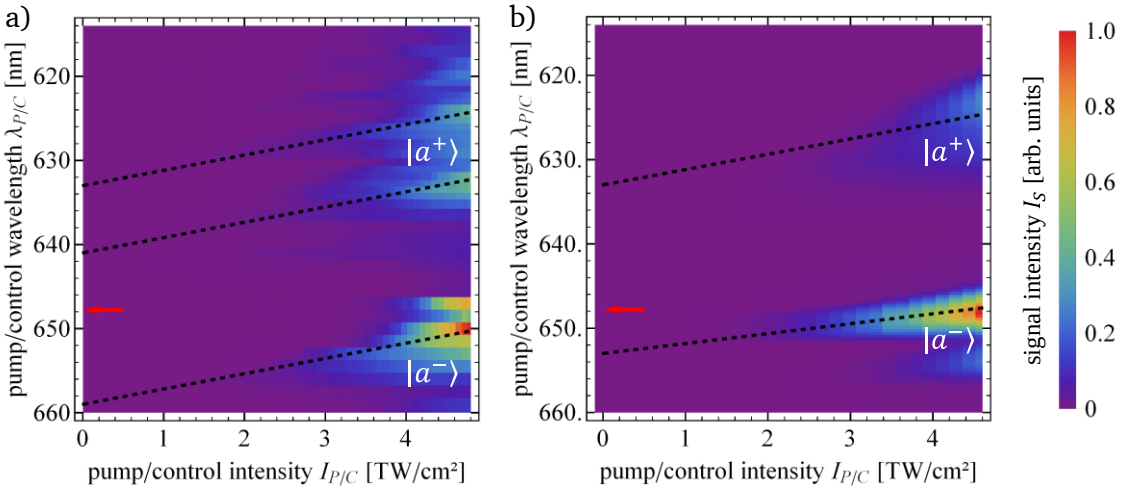

Figure 3.19: FHG signal intensity versus pump/control intensity and wavelength. The red arrow indicates the position of the bare state resonance. The black dashed lines indicate ac Stark shifts. a) Experimental data. b) Numerical simulation. For details on the simulation, see Appendix E.

The experimental data indicate the potential of the dressed state approach, also for setups with a single pump laser. Further, we see that a strong pump/control pulse modifies the atomic level structure strongly, which can reduce initial resonance enhancements via bare states and can induce new ones via dressed states.

To compare the experimental results with the theoretical expectation, we performed a numerical simulation, shown in Fig. 3.20 b). The simulation is based on a rather large number of states (nine-level system) in order to account for the more complicated coupling scheme and in order to describe the experimentally observed complicated structure at dressed state $|a^+\rangle$. Like in the experimental data, we observe in the simulation two dressed state structures $|a^+\rangle$ and $|a^-\rangle$, which appear above and below the bare state resonance (indicated by the red arrow). Both dressed states show a substructure emerging of the manifold of states $|3\rangle$. The relative strength of the dressed states is resembled well by the numerical simulation, meanwhile there are some small deviations regarding the exact energetic position (see for instance the slope of the black dashed lines of dressed state $|a^-\rangle$ in experiment and simulation and as well its distance at $I_{P/C} = 0$ to the unperturbed resonance, i.e., for the control laser turned off). Nevertheless, the simulation is in good agreement to the experimental data of the rather complicated level scheme. In conclusion, we see that the approach of using dressed state resonances with a single laser only is applicable and enables strong resonance enhancements far detuned from the bare state resonance (several ten THz).

Transfer to higher harmonic orders (7HG): We now investigate the enhancement of higher-order frequency conversion (here seventh-harmonic) for the single laser approach. As mentioned in subsection 3.5.1, the level scheme is more complicated due to further six- and seven-photon resonances. Hence, it is rather difficult to identify the origin of each peak in the spectrum of 7HG.

Figure 3.21 a)+b) shows the comparison of FHG and 7HG for an intensity up to $I_{P/C} = 4\,\mathrm{TW/cm^2}$. The data of the FHG are similar to Fig. 3.20 a) and show a large amount of peaks, which we identify as dressed states. The data of the 7HG show a similar amount of peaks, two rather strong ones at $\lambda_{P/C} = 640\,\mathrm{nm}$ and $\lambda_{P/C} = 665\,\mathrm{nm}$ at pump/control intensities of about $I_{P/C} \approx 4\,\mathrm{TW/cm^2}$, and three rather weak ones. We observe that the strongest structures of 7HG do not fit spectroscopically to the strongest peaks of FHG. Hence, in this case we cannot conclude a straightforward transfer of resonance enhancement from FHG to higher-order frequency conversion.

We now have a look at the experimental data for FHG and 7HG at higher pump/control intensities of up to $I_{P/C} = 7\,\mathrm{TW/cm^2}$ (Keldysh parameter $\gamma \approx 5$, Fig. 3.21 c)+d)). We see in both cases, that the peaks are Stark shifted to higher energies, roughly described by the increased ponderomotive energy. Further, the strength of the peaks is slightly changed and their width increases. We observe a substantial resonance enhancement via three peaks for FHG and 7HG.

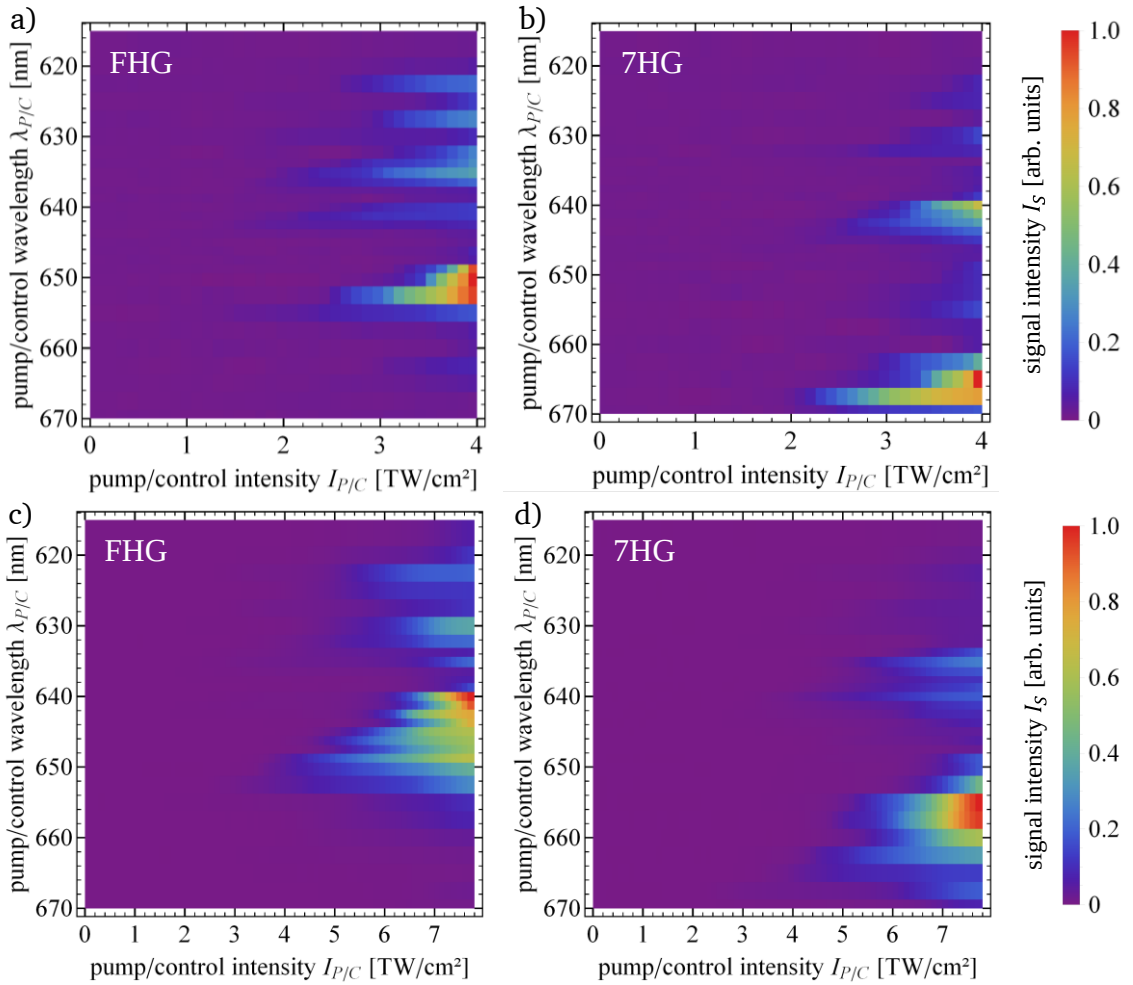

Figure 3.20: Signal intensity (harmonic intensities) versus pump/control intensity and wavelength. a) FHG signal intensity, similar to Fig. 3.20. b) 7HG signal intensity. c) FHG signal intensity at high pump/control intensity. d) 7HG signal intensity at high pump/control intensity.

However, we again do not observe a straightforward transfer of resonance enhancement from FHG to 7HG. The peaks look similar for FHG and 7HG, but are shifted in regard to each other. This phenomenon might indicate that we observe dressed states enhancements in the 7HG as well, but we cannot conclude that from the experimental data. Additional multi-photon couplings to autoionizing states become relevant, with unknown transition moments and resonantly-enhanced ionization cross sections. Hence, we could not perform accurate simulations in this case. We expect all these couplings to be strongly driven near resonance, which will lead to multiple dressed states and even modified continuum structure [90]. Nevertheless, the experimental data clearly reveal the effect of dressed states also upon 7HG at high intensities $I_{P/C} = 7$ TW/cm² and Keldysh parameters down to $\gamma \approx 5$.

3.6 Conclusion and outlook

In this chapter, we demonstrated the potential of dressed states and large Autler-Townes splittings to resonantly enhance harmonic generation of ultrashort laser pulses at high intensities (multiple TW/cm², Keldysh parameter $\gamma \approx 1$). In a first experiment, we implemented and spectroscopically investigated large Autler-Townes splittings up to $\bar{\Omega}/2\pi = 18$ THz at control laser intensities up to $I_C = 7$ TW/cm² in argon. The energetic position of the dressed states varies as expected with the control laser intensity. We observed a combination of Autler-Townes splitting and ac Stark shift. Via the induced dressed three-photon resonance, the THG signal intensity increased by more than a factor of $\eta = 80$ for off-resonant pump pulses. The data also indicated that otherwise perturbing ac Stark shifts are compensated by the Autler-Townes splitting. Moreover, we observed strong asymmetry of the frequency conversion efficiencies via different dressed states, which depends upon the control laser detuning. We investigated the inversion of the strength of the two dressed states for red and blue detuning, also describing the change in the energetic position of the dressed states. The results were confirmed by a numerical simulation. With the simulation, we also demonstrated that the compensation of ac Stark shifts by the control laser might permit larger resonance enhancements via dressed states compared to a conventional bare state resonance.

In a second experiment in xenon, we demonstrated the enhancement of THG and FHG for fixed-frequency pump pulses via a laser-controlled dressed state. In xenon, we implemented very large asymmetric Autler-Townes splittings of $\bar{\Omega}/2\pi = 100$ THz for high laser intensities (TW/cm^2). These permit applications of the dressed resonance concept in a broad wavelength range. Hence, also harmonic generation by broadband, ultrashort (fs) laser pulses benefits from such large Autler-Townes splittings, which may exceed the bandwidth of driving (fs) pulses. In systematic measurements, we observed enhancement factors of $\eta = 37$ for THG via a dressed state compared to the case without control laser. The energetic position varies as expected with the pump laser detuning and intensity. We also demonstrated higher enhancements for parallel polarized pump and control beams (in comparison to perpendicular polarization), although we observed strong sum and difference frequency mixing channels in the VUV. The dressed resonance enhancement occurs simultaneously for THG and FHG, i.e., a higher-order conversion process. For FHG we improved the signal intensity by a factor of $\eta = 43$. This indicates the potential of dressed resonance enhancements also for harmonic generation at higher orders.

We admit that the proposed approach requires a control laser pulse in addition to the pump pulse. This may increase the experimental effort and depending on the laser system reduce the available energy for the pump pulse. However, in appropriate level schemes the dressed state approach works also with a single pump laser only, which induces its own Autler-Townes splittings and shifts them into multi-photon resonance with itself. We checked this option for five-photon resonant FHG in xenon, and observed again dressed states with large Autler-Townes splittings. The dressed states showed a relatively complicated structure (multiple peaks) due to a manifold of strongly driven transitions. The data demonstrated

that the original bare state resonance enhancement vanishes. Hence, for resonantly enhanced harmonic generation at high intensities the coupling scheme has to be checked regarding excited state transitions with "small" detunings in the THz range. The investigations on the simultaneous enhancement for seventh-harmonic generation revealed that there are probably further six- and seven-photon resonances, so we cannot conclude a direct transfer of resonance enhancement for higher orders in this level scheme.

During this work we also tried to compensate ac Stark shifts in resonant FHG in xenon by a far-off-resonant Stark laser [57]. However, perturbing frequency mixing channels and population transfer opened by the Stark laser inhibited a rise of conversion efficiency for FHG. We only obtained small enhancements with a sophisticated combination with different orientations of circular and elliptic polarizations of the pump and Stark laser, which closed perturbing frequency mixing channels.

Future investigations on Autler-Townes splittings and dressed states for harmonic generation should address the question, up to which control intensities resonance enhancements via dressed states are possible (regime of Keldysh parameter $\gamma \leq 1$). In a recent theoretical study resonance enhancements via dressed states were observed up to several ten TW/cm² in helium (Keldysh parameter $\gamma = 3$) [29]. At even higher intensities and smaller Keldysh parameter, the Autler-Townes splitting "collapsed" and only one peak at the Stark shifted resonance position remained. For similar experimental investigations, we would need another power amplifier in our laser system to reach higher intensities and smaller Keldysh parameters. The investigation shall reveal the optimal intensity window for adiabatic quantum dynamics applied to nonlinear optics at higher orders.

With the current laser system, we can investigate Autler-Townes splittings in more detail, e.g., we can determine how much we can detune the pump laser in our application scheme in xenon and still benefit from the dressed state resonance. With a pump wavelength of $\lambda_P = 400.6$ nm we had a three-photon pump detuning of $\Delta_{\mathrm{P}}^{(3\mathrm{p})}/2\pi = -69$ THz. We can increase it to $\Delta_{\mathrm{P}}^{(3\mathrm{p})}/2\pi = -102$ THz with a pump wavelength of $\lambda_P = 406$ nm. Hence, this experiment shall push the limits for possible pump laser detunings even further. Another future experiment could demonstrate the applicability of the dressed state approach on two-photon resonances. This would enable better phase matching conditions for the pump and the third-harmonic while benefiting from the dressed state resonance.

4 Frequency conversion enhanced by coherent population return

In this chapter, we present experimental data on adiabatically driven frequency conversion with ultrashort (ps) laser pulses towards the VUV spectral regime, enhanced by coherent population return and preparation of maximal atomic coherences. We generate the sum frequency of an intense pump pulse and a probe pulse via a two-photon resonance in xenon. When we slightly detune the pump laser from two-photon resonance, the atomic populations are adiabatically driven forth and back from the atomic ground state to an excited state. This coherent population return (CPR) prepares the medium in a transient state of maximal atomic coherence, which enhances frequency mixing with a probe laser. We demonstrate the transfer of the adiabatic technique CPR to high intensities (TW/cm²) and Keldysh parameter down to $\gamma = 25$. The fundamental question is, whether the already large intensities still permit us to drive and exploit coherent-adiabatic dynamics for enhancement of frequency conversion efficiencies. Our experiments focus on the specific example of SFG, but the findings on CPR-enhancements are relevant for any frequency conversion process via resonances, e.g., also at higher-order nonlinear processes.

The research led to a manuscript, which is submitted to Physical Review A (authors: F. Cipura, P. Ackermann, and T. Halfmann).

4.1 Introduction to adiabatically driven frequency conversion

Two-photon resonant sum and difference frequency generation: Frequency conversion via atomic resonances is a straightforward approach to increase the output and the efficiency at the desired signal wavelength. The resonance enhancement can be orders of magnitude, as described in theory section 1.2 and demonstrated for dressed states in chapter 3. Neglecting phase mismatch, it seems obvious, that the strongest enhancement is achieved on resonance, i.e., for zero detuning. However, this does not hold true for strong couplings and respectively large pulse areas (Rabi frequency times pulse duration $\Omega\tau \gg 1$). That phenomenon can be explained by nonlinear optics in coherently-driven quantum systems (section 1.3) and paves the way to very efficient frequency conversion at maximal atomic coherence. In a typical approach for low-order frequency conversion, we tune the pump laser to a two-photon resonance in the nonlinear medium (xenon), and an off-resonant probe laser is mixed to drive sum frequency generation (SFG) or difference frequency generation (DFG) [5,12,91–93]. This yields short-wavelength photons at frequency $\omega_S = 2\omega_P \pm \omega_{Pr}$, where the indices indicate the pump (P), probe (Pr) and signal wave (S). Such four-wave mixing (FWM) schemes combine nonlinear resonance enhancement via the two-photon transition with low (linear) absorption of the pump and probe field, as the detunings to single photon resonances are large. If the probe laser is tunable, also the generated SFG and DFG field are tunable in the VUV.

If we consider frequency conversion in the context of coherent light-matter interaction, we note, that the FWM efficiency depends upon the atomic coherence

induced by the driving lasers. For the above FWM process, the atomic coherence on the two-photon transition, driven by the pump laser, is the relevant quantity. At large pump laser intensity (TW/cm² for (ps) pulses), fast Rabi oscillations of the probability amplitudes and, hence, the atomic coherence occur. Thus, in general the atomic coherence varies rapidly in time and (in average) does not provide the largest possible value, i.e., $|\rho_{12}| = 1/2$. Both the fast oscillations as well as the lower average value limit the efficiency of any conversion process via the resonance.

Frequency conversion at maximal atomic coherence: Frequency conversion at a temporally stable and maximal atomic coherence has been studied for several approaches, e.g., electromagnetically induced transparency (EIT) [17,30,31], Stark-chirped rapid adiabatic passage (SCRAP) [16,33] or CPR [16,18,94]. In contrast to EIT and SCRAP, the implementation of CPR is simple and requires only one pump field. Hence, we implement our experiments on frequency conversion at maximal atomic coherence with CPR. When a temporally sufficiently smooth laser pulse drives an atomic transition slightly detuned from resonance, the population is adiabatically (i.e., without fast Rabi oscillations) driven from the ground to the excited state (coherent superposition) and completely back again. No population remains in the excited state after the laser pulse - no matter how strong the driving pump pulse is, irrespective of the exact value of the detuning, and irrespective of the specific smooth pulse shape. This is the basic feature of CPR. Because of the adiabatic dynamics during CPR a temporally stable atomic coherence is established. For large pump intensity, the coherence reaches a temporally stable maximal value of $|\rho_{12}| = 1/2$ during the pump pulse. The smooth dynamics and large average atomic coherence enable efficient resonantly enhanced frequency conversion.

So far, CPR was experimentally demonstrated in frequency conversion with long (ns) pulses at moderate intensities in the regime of GW/cm² [16,18,94], yielding significant support for low-order, low-intensity frequency conversion. CPR was theoretically also proposed for high-order harmonic generation [95]. However, the applicability of adiabatic passage processes for high intensities and frequency conversion processes beyond low orders remains an open question. Typically, adiabatic passage processes are rather slow and require a combination of sufficient coupling strength via resonances (or near resonances) and interaction time. Thus, the product of Rabi frequency Ω and pulse duration τ should be large, i.e., $\Omega\tau \gg 1$. To use a simple term from the background of incoherent excitation, the latter condition defines saturation of the transition. This is difficult (or in most cases impossible) to achieve for interaction with ultrashort pulses. Moreover, intense, ultrafast laser pulses yield huge ac Stark shifts of atomic resonances, which significantly modify the atomic coupling schemes required for resonant (or near resonant) adiabatic interactions - and may reduce resonantly enhanced conversion efficiencies by orders of magnitude [22]. Hence, the transfer of adiabatic techniques such as CPR to the regime of high-intensity frequency conversion is no straightforward task. In this chapter, we want to transfer the adiabatic techniques CPR to the regime of high-intensity frequency conversion.

The chapter is structured as follows: After a basic discussion of CPR-enhanced frequency conversion, the numerical simulation and the experimental setup, we experimentally demonstrate that we achieve large pulse areas on a two-photon transition in xenon. Further, we investigate spectroscopically the enhancement of frequency conversion via CPR. We find that ac Stark shifts induce an asymmetry in the spectral characteristics of CPR, which nevertheless permits an enhancement above the resonant case. For the case of resonantly enhanced frequency conversion we show, that the atomic coherences are maintained for several ten picoseconds after the pump pulse, which permits time-delayed frequency conversion. Moreover, we analyze the pressure dependence of the atomic coherences lifetime and observe a free induction decay at the two-photon coherence with generation of a second-harmonic field. The findings may serve as a first step towards applications of adiabatic passage processes also for resonantly enhanced frequency conversion at high intensities and higher orders.

4.2 Basics of CPR-enhanced frequency conversion

For a basic understanding of CPR-enhanced frequency conversion we consider now a two-level system with the ground state $|1\rangle$ and the excited state $|2\rangle$, coupled by a pump laser. In the specific case of our experiment discussed below the pump laser drives a two-photon transition, though this does not matter for our basic discussion now. We are interested in the atomic coherence ρ_{12}, excited by the pump laser. The coherence can be probed, e.g., by sum frequency mixing with an additional probe laser pulse. This yields a signal wave, e.g., for the specific case in our experiment at the sum frequency $\omega_S = 2\omega_P + \omega_{Pr}$. As we saw in theory section 1.3, the induced (nonlinear) polarization in the medium is proportional to the generated atomic coherence. The generated SFG signal intensity I_S is a direct measure of the absolute value of the atomic coherence, i.e., $I_S \sim |\rho_{12}|^2$. Therefore, the SFG yield increases with the atomic coherence and also mirrors the dynamics of the latter. In other words, the frequency conversion process serves as a measure of the atomic coherence. In the following we discuss the dynamics of the atomic coherence, which we calculate from the Liouville-von Neumann equation (see eqn. 1.19):

$$\dot{\hat{\rho}}(t) = \frac{i}{\hbar}\left[\hat{\rho}(t), \hat{\mathrm{H}}(t)\right] - \hat{\Gamma} \tag{4.1}$$

with the density operator $\hat{\rho}$, the Hamiltonian $\hat{\mathrm{H}}$ and the loss operator $\hat{\Gamma}$, which may include ionization losses of the excited state, radiative population decay (which

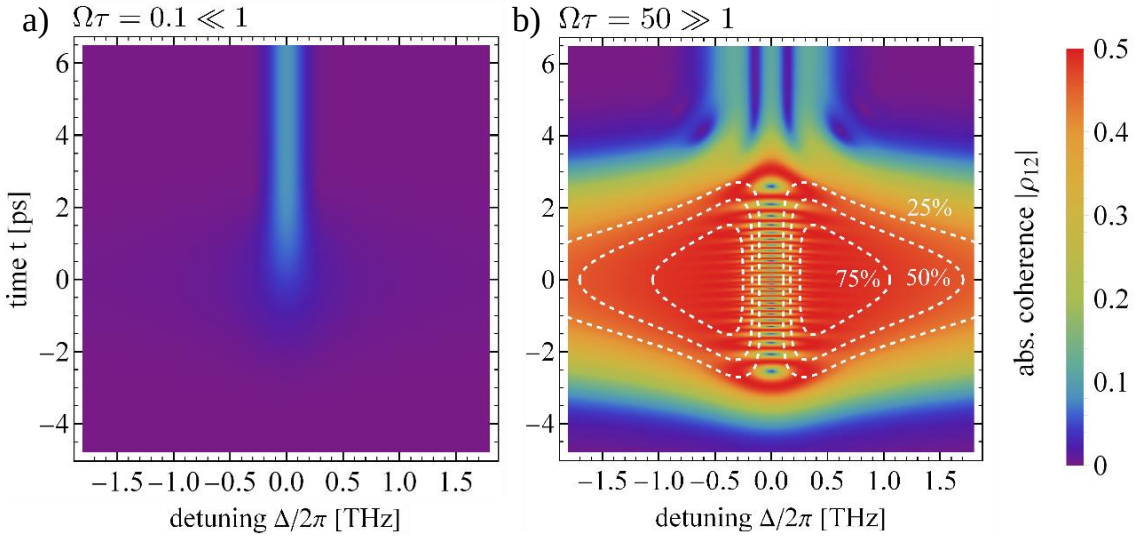

Figure 4.1: Numerical simulations of the absolute value $|\rho_{12}|$ of the atomic coherence vs. time and detuning for a pump pulse with Gaussian temporal profile centered at $t = 0$ and pulse duration (FWHM) $\tau = 2$ ps. a) Coherence for small pulse area $\Omega\tau = 0.1 \ll 1$. b) Coherence for large pulse area $\Omega\tau = 50 \gg 1$. The dashed lines indicate regions of large coherence, i.e., where for a pulse duration of $\tau = 2$ ps the time averaged coherence $|\rho_{12}|^2$ is 25 %, 50 % or 75 % larger than the resonant value. We did not apply spatial averaging.

typically does not play a role on the time-scale of ultrashort laser pulses) and dephasing processes, e.g., due to collisions and Doppler broadening. The Hamiltonian of the two-level system in interaction representation and rotating wave approximation reads [34]:

$$\widehat{H}(t) = \frac{\hbar}{2}\begin{pmatrix} -2\Delta & \Omega(t) \\ \Omega^*(t) & 0 \end{pmatrix} \tag{4.2}$$

with the Rabi frequency Ω and the detuning Δ of the pump laser from the resonance frequency ω_{12} between the two quantum states (an extended Hamiltonian for the two-photon transition, also including additional laser-induced ac Stark shifts is discussed in section 4.3).

Figure 4.1 a) shows the results of a numerical simulation of the coherence for a low intensity, i.e., small pulse area $\Omega\tau \ll 1$ and, hence, low excitation probability. The maximal temporally averaged coherence is generated, when the pump laser is tuned on resonance $\Delta = 0$, which seems an obvious choice. The coherence increases during the interaction and reaches its maximum after the pulse. For off-resonant excitation $\Delta \neq 0$ the excitation probability is lower, as we had also expected intuitively. However, the features change significantly for larger intensity, i.e., large pulse area $\Omega\tau \gg 1$ and, hence, strong excitation. As Fig. 4.1 b) shows in this case, on resonance $\Delta = 0$ we get fast, diabatic Rabi oscillations, which are well-known and expected for strong, coherent excitation. However, slightly off resonance the Rabi oscillations damp out, while the coherence remains on a high level (see areas indicated by dashed lines in Fig. 4.1 b)). We get a smooth (adiabatic) evolution of the coherence in time. Thus, the temporally averaged coherence is larger off resonance than on resonance. This seems, at least on the first glance, a quite surprising finding. We note that for such off-resonant excitation at large Rabi

frequency, the coherence evolves from zero to a maximal value and afterwards *returns back* to zero. Obviously, the quantum system is coherently driven from the ground state $|1\rangle$ up to the excited state $|2\rangle$ (coherent superposition) - and (completely) back to the ground state $|1\rangle$ again. This adiabatic evolution forth and back between the two states defines CPR [96]. In summary, at pulse area $\Omega\tau \gg 1$ we get a large and smooth atomic coherence, when the driving laser is slightly off resonance. Note that it is of course possible to achieve a maximal coherence on resonance with a pulse area of $\Omega\tau = \pi/2$ ($\pi/2$-pulse). However, this approach suffers strongly from intensity fluctuations and spatial averaging effects (Gaussian beam profile) in comparison to CPR.

We can easily understand the (on the first glance) surprising features of CPR, when we consider the atomic population dynamics in the basis of the dressed states:

$$|+\rangle = \cos\Theta\,|1\rangle + \sin\Theta\,|2\rangle \tag{4.3}$$

$$|-\rangle = -\sin\Theta\,|1\rangle + \cos\Theta\,|2\rangle \tag{4.4}$$

with the mixing angle $\Theta = 1/2\tan^{-1}(\Omega(t)/\Delta)$. For adiabatic evolution, we require the system to remain in one of the dressed states during the interaction. When the pulse duration is finite and the detuning Δ is assumed constant, we get $\Theta = 0$ well before and well after the interaction. Thus, at these times the dressed states are uniquely identified with the bare states:

$$|+\rangle\,(t \to \pm\infty) = |1\rangle \tag{4.5}$$

$$|-\rangle\,(t \to \pm\infty) = |2\rangle \tag{4.6}$$

Therefore, if the evolution is adiabatic, the system will end in the same state as it started (in our case in state $|1\rangle$ via the dressed state $|+\rangle$). When the Rabi frequency is sufficiently large, i.e., $\Omega \gg |\Delta|$ we get $\Theta = \pi/4$ and

$$|+\rangle = \sqrt{1/2}\,(|1\rangle + |2\rangle) \tag{4.7}$$

The system is now in a coherent superposition of the bare states with equal amplitudes, i.e., a maximal coherence $|\rho_{12}| = 1/2$.

The theoretical treatment for adiabatic evolution in CPR yields for sufficiently smooth laser pulses the simple adiabaticity condition $|\Delta|\tau \geq 1$, independent of the exact value of the Rabi frequency [96]. The condition for the detuning simply means, that the detuning must exceed the Fourier transform limited bandwidth $1/\tau$ of the driving pump pulse. From the condition for strong excitation $\Omega\tau \gg 1$ we can alternatively write $\Omega \gg \Delta$.

As we have seen from the above considerations, during CPR we get a smooth and maximal coherence. Hence, also any frequency conversion process via the resonance will yield maximal efficiency, when the driving laser is slightly off resonance (rather than tuned on resonance). A full theoretical treatment yields, that the temporally averaged coherences for CPR vs. resonant excitation differ by a factor of $\pi/2$. This leads to an enhancement of the SFG intensity under CPR conditions by a factor of two. Moreover, the temporal profile of the generated radiation

will follow the smooth variation of the coherence in the CPR case and, hence, exhibit no fast intensity fluctuations, as it would be the case for resonant excitation. Thus, CPR-assisted resonantly enhanced frequency conversion exhibits less intensity fluctuations compared to the conventional case [18]. These advantageous features of CPR are relevant for any frequency conversion process via a resonance, e.g., also at higher orders compared to our specific example of SFG (provided we operate in the perturbative regime of frequency conversion). Finally, we note that CPR generates a transient coherence during the interaction with the pump pulse, while there remains no residual coherence after the interaction. This is different in the resonant case, where there is (in general) always a residual coherence after the pump pulse. This leads to different features of CPR-assisted and conventional resonantly enhanced frequency conversion in a pump-probe experiment, e.g., when we delay a probe pulse with regard to the pump pulse and monitor the SFG yield vs. the delay. For resonant excitation we also get an SFG signal, when the probe pulse is delayed with respect to the pump pulse (as there is also a residual coherence after the pump pulse), while there is no SFG yield for delayed probe and pump in CPR (as there is no residual coherence left after the pump pulse in this case).

In the above, basic discussion of CPR and CPR-assisted frequency conversion we ignored ac Stark shifts, losses, or dephasing processes, e.g., due to radiative decay, collisions or Doppler broadening. The latter play a role and modify the coherent dynamics in the quantum system, when the laser pulse duration or delay exceeds the coherence time, e.g., determined by the timescale of collisions. In the full theoretical treatment of our experiments in xenon, we include these perturbing processes (see below).

4.3 Calculation of the generated sum frequency

4.3.1 Theory of SFG via atomic coherences

We follow the basic, conventional treatment of frequency conversion and quantum-mechanical calculation of nonlinear optical polarizations (see section 1.3 and textbooks, e.g., Boyd [14] or Shore [34,35]). The SFG signal field generated by nonlinear optical frequency conversion is given by a wave equation in SVEA approximation as (compare eqn. 1.7):

$$\frac{\partial}{\partial z} E_S = i \frac{\omega_S}{2c\varepsilon_0 n_S} P^{(3)} \tag{4.8}$$

with the electric field amplitude of SFG E_S, the macroscopic third-order polarization for SFG $P^{(3)}$, the SFG frequency ω_S and the index of refraction n_S. The polarization on the SFG transition between the ground state and the continuum state $|c\rangle$ (for our level scheme in Fig. 4.3 a)) can be calculated from the induced, microscopic dipole moment in the quantum system as:

$$P^{(3)} = N\langle\hat{\mu}\rangle = N\mu_{1c}\rho_{1c} \sim N\mu_{1c}\rho_{12} \tag{4.9}$$

with the atomic number density N, the expectation value of the electric dipole operator $\langle\hat{\mu}\rangle$, the effective transition dipole moment μ_{1c} of the SFG transition between the ground and the continuum state and the atomic coherence ρ_{1c} on the latter transition. The simple, linear relation between the coherences $\rho_{12} \sim \rho_{1c}$ is valid for small probe pulse area, i.e., weak excitation by the probe laser [35]. Neglecting constant prefactors, and assuming small conversion efficiencies (i.e., undepleted pump and probe field) from the SFG wave equation we get now the simple correspondence:

$$\frac{\partial E}{\partial z} E_S \sim N\rho_{12} \tag{4.10}$$

After integration over a propagation distance L we get for the SFG intensity:

$$I_S \sim (NL)^2 |\rho_{12}|^2 \tag{4.11}$$

Obviously, the SFG intensity grows quadratically with the induced atomic coherence. Also, the temporal dependence of the generated field will follow the dynamics of the atomic coherence. Hence, SFG serves as a measure for the atomic coherence.

4.3.2 Hamiltonian of the coupling system

The Hamiltonian of the two-level system (with the two-photon transition) in interaction representation and rotating wave approximation reads [34]:

$$\widehat{H}(t) = \frac{\hbar}{2}\begin{pmatrix} -2\Delta_P^{(2p)} - S(t) & \Omega_P^{(2p)}(t) \\ \Omega_P^{(2p)^*}(t) & 0 \end{pmatrix} \tag{4.12}$$

with the pump two-photon Rabi frequency $\Omega_P^{(2p)}$ and the pump detuning $\Delta_P^{(2p)} = 2\omega_P - \omega_{12}$ with respect to the two-photon transition frequency ω_{12}. For our experiment at high laser intensity, we have to add the time dependent ac Stark shift S in the Hamiltonian. For the numerical simulations, we approximate the ac Stark shift S again by the ponderomotive energy. We note that in our case the ac Stark shift induced by the pump laser dominates, while we neglect the experimentally much smaller shift induced by the probe laser [42]. However, as the experimental data in subsection 4.5.5 show, this assumption is only valid for moderate probe intensities and low wavelength, i.e., small ponderomotive energy, induced by the probe laser.

In Fig. 4.2 we show the results of a numerical simulation of the coherence for a high intensity, i.e., large pulse area $\Omega\tau \gg 1$, and with ac Stark shift. In comparison to Fig. 4.1 (calculation of the coherence without ac Stark shift), we observe a strong asymmetry induced by the ac Stark shift. The enhancement for detunings $\Delta < 0$ are smaller compared to the case without ac Stark shift. However, for detunings $\Delta > 0$ we observe a larger temporally stable maximal coherence. Hence, the CPR approach applies as well for moderate ac Stark shifts and can even benefit from it.

In our specific experiment, Rabi frequency and detuning refer to a two-photon transition. The two-photon Rabi frequency can be calculated via combination of

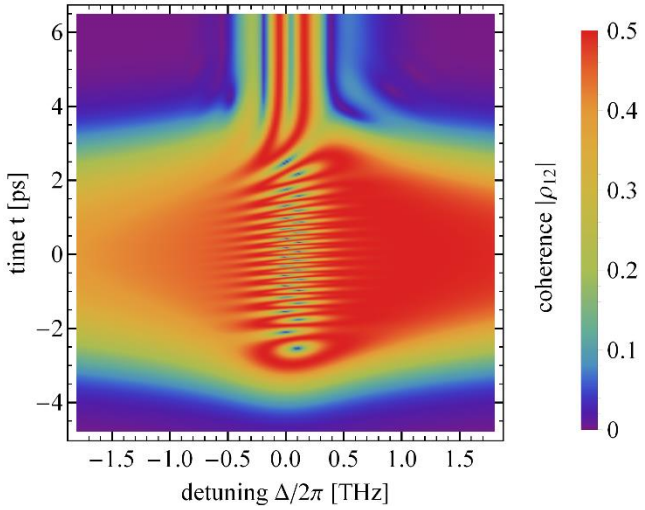

Figure 4.2: Numerical simulations of the absolute value $|\rho_{12}|$ of the atomic coherence vs. time and detuning for a pump pulse with Gaussian temporal profile centered at $t = 0$ and pulse duration (FWHM) $\tau = 2$ ps with an ac Stark shift equal to the ponderomotive energy. The coherence is calculated for large pulse area $\Omega\tau = 50 \gg 1$. We did not apply spatial averaging.

single-photon Rabi frequencies, taking all possible intermediate states $|i\rangle$ between the ground state $|1\rangle$ and the excited state $|2\rangle$ into account (compare eqn. 3.1):

$$\Omega_P^{(2p)} = \sum_i \frac{\mu_{1i}\mu_{i2}}{2\hbar^2\Delta_{1i}} E_P^2 = \sum_i \frac{\Omega_{1i}\Omega_{i2}}{2\Delta_{1i}} \tag{4.13}$$

with the transition dipole moments μ_{ij}, the single-photon detunings Δ_{ij}, the electric field amplitude of the pump laser E_P. For rare gases and excitation by UV radiation, the detuning Δ_{1i} between the atomic ground state and any intermediate state is in the order of the driving laser frequency, i.e., $\Delta_{1i} \approx 2\pi \cdot 10^3$ THz. That means, that for large pulse area $\Omega_P^{(2p)}\tau_P \gg 1$, with the pump pulse duration of $\tau_P = 2$ ps, we require single-photon Rabi frequencies $\Omega_{ij} \approx 2\pi \cdot 30$ THz. Assuming typical atomic transition dipole moments $\mu \approx 10^{-29}$ Cm, this corresponds to laser intensities in the TW/cm² regime.

4.3.3 Numerical simulation

The numerical simulations follow the theoretical treatment presented above. For both pump (P) and probe (Pr) pulse, we assume Gaussian spatial and temporal profiles, with a ratio of beam diameters $w_P/w_{Pr} = 1.25$ (slightly different from the experimental ratio of two to correct for different Rayleigh lengths and non-perfect overlap), and pulse durations $\tau_P = 2$ ps and $\tau_{Pr} = 3$ ps (equal to the experimental parameters). We estimate the ac Stark shift of the pump pulse by the ponderomotive energy $\phi = \hbar S$. For a pump intensity of $I_P = 1$ TW/cm² and a pump wavelength of $\lambda_P = 225$ nm, we get an ac Stark shift $S/2\pi = 1.14$ THz.

The most relevant losses in our coupling scheme are due to ionization of excited state $|2\rangle$, induced by the pump laser. When the ionization rate becomes large, it destroys the generated atomic coherence. From simple theoretical considerations we find, that the ionization rate must not exceed the Rabi frequency to permit coherent-adiabatic interaction. The ionization rate Γ is proportional to the pump intensity, similar to the two-photon Rabi frequency $\Omega_P^{(2p)}$. Hence, the ratio $\Omega_P^{(2p)}/\Gamma$ is a constant, given by the medium. In our level scheme in xenon, the Rabi frequency is at least three times larger compared to the ionization rate (provided we

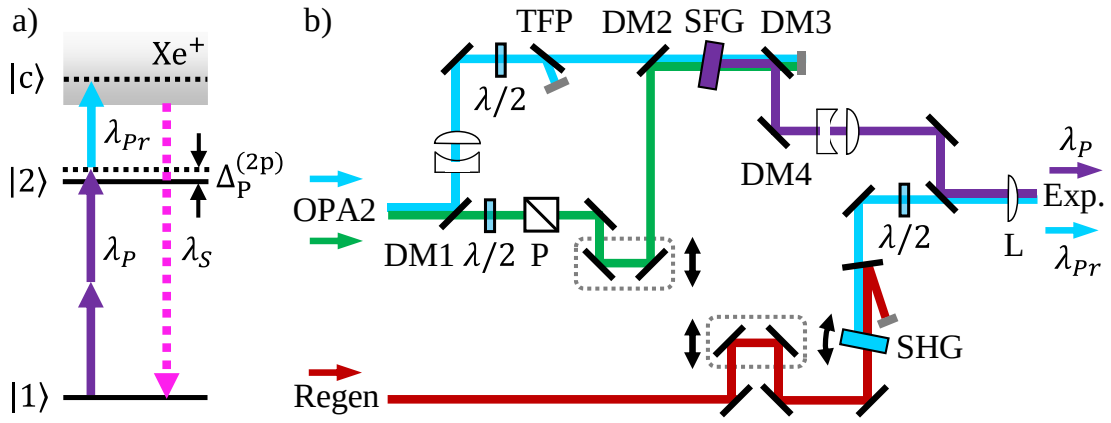

Figure 4.3: a) Coupling scheme for CPR-assisted SFG in xenon with relevant energy levels and transitions. The detuning $\Delta_P^{(2p)} = 2\omega_P - \omega_{12}$ is defined with respect to the two-photon transition at frequency ω_{12}. b) Schematic overview of the experimental setup, as relevant for the experiments discussed in section 4.4. For details on the laser setup see chapter 2 above. Beam guiding optics are neglected for simplicity. P: polarizer, L: lens.

do not saturate the ionization at very large laser intensity). Per TW/cm², we calculate a two-photon Rabi frequency $\Omega_P^{(2p)} = 2\pi \cdot 3$ THz and an ionization rate $\Gamma = 2\pi \cdot 1$ THz, using a theoretical prediction $\sigma = 0.8$ Mb for the ionization cross section [97]. However, from comparison of our SFG experiments with the numerical simulations we found, that the ionization rate should be even much smaller, in the range of $\Gamma = 2\pi \cdot 0.1$ THz per TW/cm² intensity. This fits also well with other experiments via the same excited state $5p^5\ 7p\ ^2[1/2]_0$ in xenon (although there the probe was close to the autoionizing states, which strongly modifies the ionization cross section) [18,94]. Hence, for intensities in the TW/cm² regime, coherent-adiabatic interactions are possible in our coupling scheme. We use the ionization loss rate in the loss operator of the Liouville-von Neumann equation (eqn. 4.1) to introduce a decay of the density matrix elements ρ_{12}, ρ_{21}, and ρ_{22}.

4.4 Level scheme and experimental setup

We conducted the experiments on frequency conversion enhanced by CPR in xenon. The medium offers sufficient transmission in the VUV regime, i.e., at the wavelength of the generated SFG signal. Moreover, xenon exhibits quite large nonlinear susceptibilities in the VUV compared to other gaseous media. The excited states of xenon are accessible via a two-photon transition with a pump laser in the UV, in our case between the ground state $|1\rangle = 5p^6\ ^1S_0$ and the excited states $|2\rangle = 5p^5\ 7p\ ^2[1/2]_0$ at a pump wavelength of $\lambda_P = 225$ nm (see Fig. 4.3 a)). Note that as well another level scheme via the excited state $|2\rangle = 5p^5\ 6p\ ^2[5/2]_2$ was implemented during a bachelor thesis project [98], but suffered from higher ionization rates. To probe the generated atomic coherence by SFG, we apply a probe laser pulse with a wavelength of $\lambda_{Pr} = 400$ nm, which induces a coupling to ionization continuum states $|c\rangle$. This yields an SFG signal at a wavelength of $\lambda_{SFG} = 88$ nm. At this choice of wavelengths there are no autoionizing Rydberg

states nearby, which could lead to additional couplings. Similar coupling schemes are also possible, e.g., in krypton [99–101]. Note that we generate in addition the third-harmonic of the pump pulses and the difference frequency $2\omega_P - \omega_{Pr}$. However, we mainly discuss sum frequency generation. The disadvantage of THG is the averaging over the whole pump beam profile (we choose the probe beam diameter smaller than the pump beam profile), the disadvantage of the DFG is the rather long VUV wavelength (156 nm) and hence the lower signal level at our VUV spectrometer due to a reduced sensitivity (especially the EMT).

The relevant part of the experimental setup is shown in Fig. 4.3 b). There are two beamlines to generate the pump and the probe pulse. The pump pulse with a wavelength tunable around $\lambda_P \approx 225$ nm is the sum frequency of the OPA output ($514 - 517$ nm, up to 100 μJ) and the second-harmonic of the regenerative amplifier (400 nm, up to 750 μJ). The figure shows the beam path after the two-stage OPA (see subsection 2.1.3). First, we split the OPA output and its pump in order to adjust temporal overlap, pulse energy, beam diameter ratio and polarization. The setup is a modified two-color Mach-Zehnder interferometer, with dichroic mirrors for the separation (DM1, DMLP425, Thorlabs) and recombination (DM2, DMSP425, Thorlabs) of the beams. The nonlinear crystal for SFG is a BBO (dimensions: 5 mm x 5mm x 2mm, cut angle 65°, polished). We generate pump pulses with a wavelength tunable around $\lambda_P \approx 225$ nm with an energy of $E_P = 30\,\mu$J, and a pulse duration of $\tau_P = 2$ ps (FWHM), corresponding to a bandwidth (FWHM) of $\delta\omega_P = 0.25$ THz. The full separation of the beams after SFG requires five dichroic mirrors (DM3, high reflective at 225 nm and following mirrors; just four depicted in Fig. 4.3b)).

The probe pulse at $\lambda_{Pr} = 400$ nm is the second-harmonic of the regenerative amplifier generated in a BBO (dimensions: 6 mm x 6 mm x 1.6 mm, cut angle 30°, protective coating) obtaining pulse energies of some μJ (typical probe pulse energy for the experiment: $E_{Pr} = 3\,\mu$J). The fundamental and the second-harmonic are separated by a dichroic mirror (DM4, high reflective 800 nm for 0°-11° angle of incidence, Laseroptik).

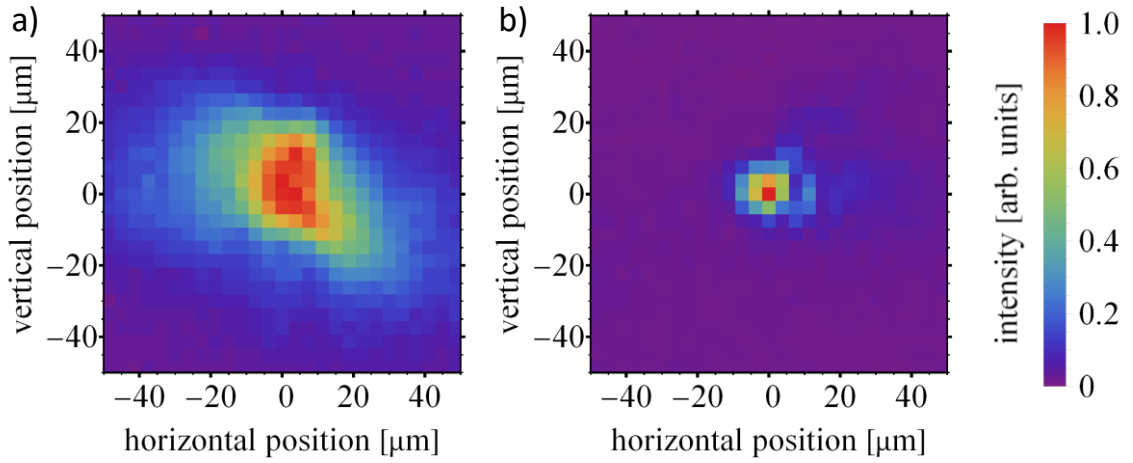

Figure 4.4: a) Pump beam intensity profile and b) probe beam intensity profile in the interaction region.

The pump and probe laser pulses are linearly polarized, overlapped in space by a dichroic mirror, and in time by an adjustable delay stage (traveling range 10 cm corresponding to 334 ps, Limes 122 linear stage , OWIS [23]). During our spectroscopic measurements, we control and optimize the spatial and temporal overlap for each wavelength tuning step. The pulse energies of the pump and the probe laser pulses are controlled individually by variable attenuators consisting of a half-wave plate and a polarizer. For the pump we attenuate the energy via the variable attenuator of the OPA output. The pump beam profile showed no significant changes for attenuated OPA output energies. A variable attenuator directly in the pump beam would reduce the maximal possible pulse energy by roughly 30 %, e.g., due to absorption in a Glan-Laser BBO polarizer. We focus both pulses into the vacuum setup by a single lens ($f = 125$ mm, fused silica, anti-reflection coated $210 - 400$ nm) , yielding beam diameters ($1/e^2$ intensity) in the range of $d_P = 30\,\mu$m for the pump and $d_{Pr} = 15\,\mu$m for the probe beam in the interaction region. The beam profiles were measured by a CCD camera (The Imaging Source, DMM 25G445-ML with removed cover glass, pixel size 3.75 μm x 3.75 μm) and are shown in Fig. 4.4. We choose a smaller probe diameter compared to the pump beam in order to reduce spatial averaging effects across the pump beam profile. The Rayleigh length of the pump beam is $z_{R,P} = 3$ mm and of the probe beam $z_{R,Pr} = 0.5$ mm. This is already in the range of the interaction length in the gas jet $L \approx 1$ mm [66]. Further reduction can perturb frequency conversion due to phase mismatch induced by the Gouy phase.

We utilize a variable telescope in the pump beam, with which we adjust the pump beam divergence, to align the longitudinal focus position of the probe vs. the pump beam. The vacuum setup is the same as described in section 2.2. For the gas nozzle, we apply stagnation pressures of $p = 200$ mbar xenon. The EMT supply voltage is relatively low with 3.5 kV (5 kV is the maximum). This is due to a higher noise level induced by scattered pump radiation, to which the EMT is sensitive.

4.5 Experimental results

4.5.1 Strong coupling and large areas

A prerequisite for the enhancement of frequency conversion via adiabatic processes are large pulse areas, i.e., strong couplings. Hence, pulse areas $\Omega_P^{(2p)}\tau_P \gg 1$ are required and theoretically achievable with intensities in the range of TW/cm² on two-photon transitions in xenon. We now demonstrate that we achieve the required pulse areas in the experiment. Figure 4.5 a) shows the SFG signal intensity versus the pump intensity and the corresponding pulse area on resonance. For low pulse areas ($\Omega_P^{(2p)}\tau_P < 1$) we observe a strong rise of the signal with increasing pump intensity. We checked that this rise fits with the expected quadratical pump intensity dependence ($I_S \sim I_P^2$). However, for larger pulse areas ($\Omega_P^{(2p)}\tau_P \approx 1$) we see a saturation of the signal intensity and hence, a strong discrepancy from the quadratical pump intensity dependence. For even larger pulse areas $\Omega_P^{(2p)}\tau_P = 10 - 60$ the signal intensity is almost constant, as we expect it for fast Rabi oscillations of the coherence. This clearly reveals that we achieve the necessary pulse areas required for adiabatically enhanced frequency conversion. The specific shape of the signal intensity versus the pulse area depends strongly on two parameters: the beam diameter ratio (between pump and probe) and the ionization rate. On the one hand, spatial averaging effects lead to an increased signal intensity. While we have in the center of the beam large pulse areas $\Omega_P^{(2p)}\tau_P \gg 1$ and hence saturation, we still have lower intensities in the outer regions with $\Omega_P^{(2p)}\tau_P \ll 1$ and hence still a rising signal intensity. On the other hand, a strong

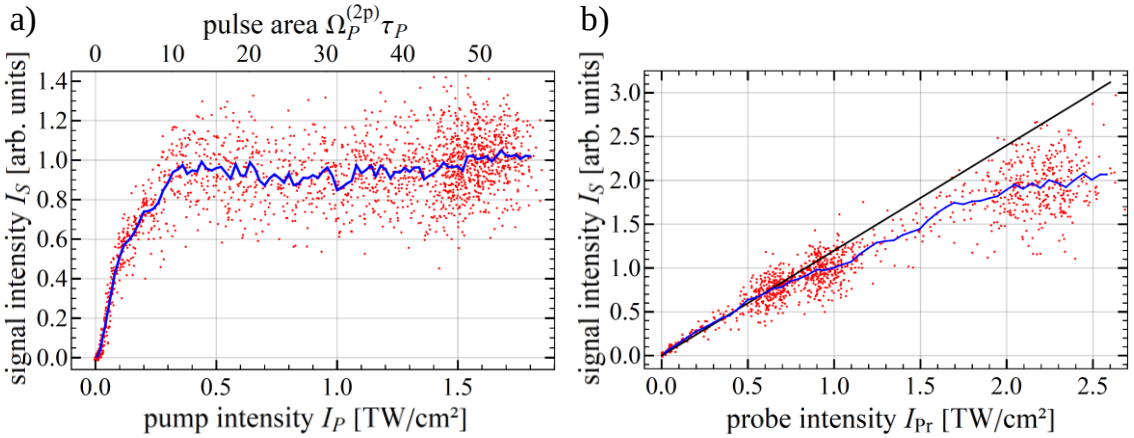

Figure 4.5: a) SFG signal intensity vs. pump intensity (bottom axis) or the corresponding pulse area (top axis) on resonance, i.e., $\Delta_P^{(2p)} = 0$. Probe intensity is $I_{Pr} = 1$ TW/cm². Data points red, moving average blue. b) SFG signal intensity vs. probe intensity on resonance. The pump intensity is $I_P = 1.7$ TW/cm², corresponding to a Keldysh parameter of $\gamma = 25$, which is relatively high for the intensity due to the short pump wavelength. Data points red, moving average blue. The black line shows a linear fit to the low probe intensity data ($I_{Pr} \leq 0.6$ TW/cm²).

ionization rate reduces the signal intensity drastically, as the time averaged coherence is reduced. Hence, in the experimental data in Fig. 4.5 a) we observe a trade-off between both effects.

Another requirement for a precise investigation of the two-photon coherence and the adiabatically enhanced frequency conversion is a low probe laser intensity, because it should not interfere with the adiabatic pump process. However, the signal to noise/background ratio of the signal intensity requires not too small probe laser intensities. Figure 4.5 b) shows the SFG signal intensity versus the probe intensity on resonance for a large pulse area. Up to a probe intensity of roughly $I_{Pr} \leq 1$ TW/cm², we observe a linear rise of the signal intensity. For higher probe intensities, we see a saturation of the signal intensity. Hence, we choose for the measurements a probe intensity of $I_{Pr} = 1$ TW/cm² as a trade-off between signal intensity and perturbing effects by the probe, e.g., ac Stark shifts, ionization and population transfer.

4.5.2 CPR-enhanced frequency conversion

Pump detuning dependency: In a first measurement, we monitored the SFG signal intensity versus the pump laser detuning from the two-photon resonance and compare it to a numerical simulation (see Fig. 4.6). Let us first consider the case of small pump pulse area (low intensity, weak excitation). SFG reaches a maximum, when the pump laser is tuned on resonance ($\Delta_P^{(2p)} = 0$). The SFG signal intensity is lower for off-resonant excitation ($\Delta_P^{(2p)} \neq 0$). We turn now our attention to the case of large pump pulse area (large intensity, strong excitation). The spectral shape of the SFG yield changes now significantly. We clearly identify two peaks of CPR-enhanced SFG (labeled A and B). The peaks show up, as expected for CPR, detuned from the Stark shifted atomic resonance (resonance position for large

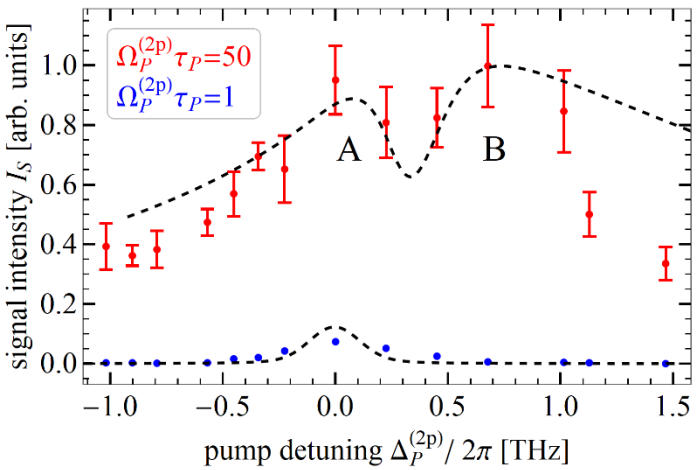

Figure 4.6: SFG signal intensity vs. pump detuning for small pulse area $\Omega_P^{(2p)}\tau_P = 1$, corresponding to a pump intensity of $I_P = 0.03$ TW/cm², and large pump pulse area $\Omega_P^{(2p)}\tau_P = 50$, corresponding to a pump intensity of $I_P = 1.7$ TW/cm². Error bars indicate standard deviation. Black dotted lines show numerical simulations. The two peaks labelled A and B indicate CPR-enhanced frequency conversion. For the parameters of the simulation see section 4.2. For the simulation at large pulse area we added a small detuning offset of 0.2 THz to compensate for additional ac Stark shifts in the experiment.

pulse area $\Delta_P^{(2p)}/2\pi = -0.3$ THz). In particular, on peak B, CPR yields a larger SFG signal compared to conventional, resonantly-enhanced conversion. On resonance, inbetween the CPR peaks, we get a dip in the conversion efficiency. The enhancements in the CPR regions A and B are different, i.e., we observe a pronounced asymmetry in the SFG profile of Fig. 4.6 - which is also confirmed by the simulation (see Fig. 4.2). This is due to the ac Stark shift, which breaks symmetry. We note some deviations of the numerical simulation compared to the experimental data, which are mainly due to residual detuning and averaging effects across the spatial profile of the pump laser, as the diameter of the probe laser is smaller, but not much smaller compared to the pump pulse.

SFG versus pump intensity and pump detuning: Figure 4.7 shows a comparison of a larger collection of measurements and simulations similar to Fig. 4.6, combined in a 2D plot of the SFG signal intensity both versus pump intensity (or pulse area) and pump detuning. In the plots, we clearly identify two regions of CPR-enhanced SFG. We discuss now some specific intensity dependent spectral features of the CPR profiles. The white dashed lines in Fig. 4.7 a) indicate the spectral bandwidth (FWHM) of the structures at fixed pump intensity. The spectral bandwidth broadens from 0.3 THz for low pump intensities up to 1.8 THz at the highest intensities. This is also a clear indicator for strong excitation, i.e., large pulse area - which is a prerequisite for CPR. When we follow the white dashed lines from low to higher pump intensity, up to an intensity of $I_P \leq 0.5$ TW/cm² we observe an asymmetric variation of the two spectral boundaries. Moreover, at these moderate intensities the center-of-mass of the spectrum (i.e., the region between the dashed lines) shifts to larger detunings. This is due to the ac Stark shift, induced by the pump laser.

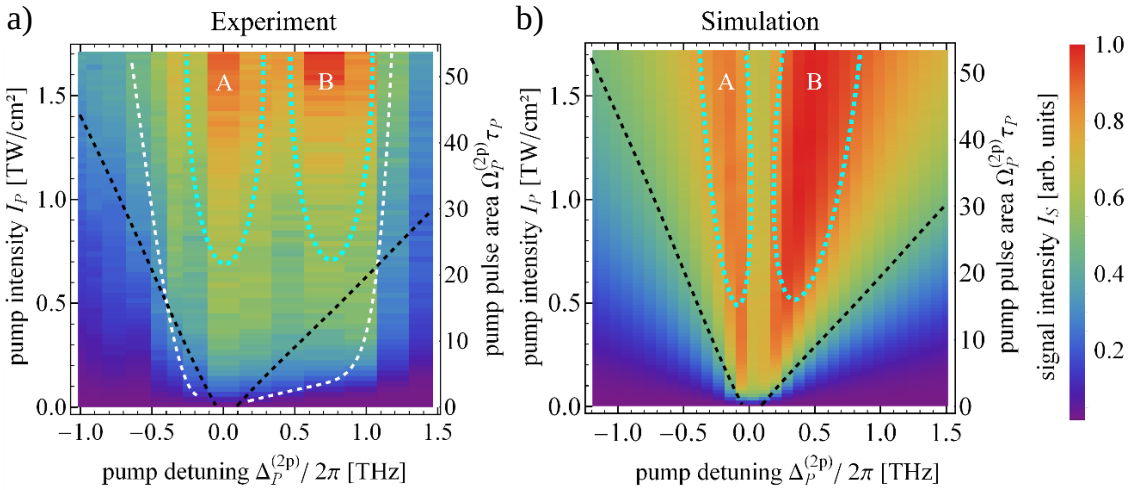

Figure 4.7: a) SFG signal intensity vs. pump intensity (left axis) or the corresponding pulse area (right axis) and the two-photon pump detuning. Pump and probe pulses are coincident. The probe intensity is kept fixed at $I_{Pr} = 1$ TW/cm². The white dashed line indicates the spectral bandwidth (FWHM) for the experimental data, the black dashed line the bandwidth obtained from a numerical simulation. The two areas labelled A and B (indicated by cyan dashed lines) show regions of CPR-enhanced frequency conversion. Stagnation pressure $p = 200$ mbar xenon. b) Numerical simulation of SFG signal intensity vs. pump intensity and two-photon pump detuning. For the parameters of the simulation see subsection 4.2.3.

For highly excited states the ac Stark shift can be well approximated by the ponderomotive energy of a free electron in a light field, which always leads to a blue shift. However, at higher pump intensities above $I_P \geq 0.5$ TW/cm² the spectral boundaries evolve quite parallel to each other in the plot of Fig. 4.7 a). The intensity dependent ac Stark shift seems to vanish in the experimental data for higher intensities, while it proceeds to grow in the numerical simulation (compare white and black lines in Figs. 4.7 a)+b)). This discrepancy is due to spatial variation effects: When in the center of the pump beam the intensity dependence of SFG saturates, the intensity dependence for large radial positions still grows. As the largest part of the available pulse energy is contained in areas with low intensities (i.e., for a Gaussian beam profile), the lower intensity regions dominate the SFG signal at higher intensities. As a result, the "effective" ac Stark shift (which we observe in the SFG signal) is much smaller than the peak value. The effect becomes even more pronounced for inhomogeneities in the beam profile. Moreover, we note that our calculation also neglects additional ac Stark shifts by the probe laser.

Pump intensity dependency: As the 2D plot mainly showed the CPR-enhanced regions A and B, we now have a closer look on the dependency of the SFG signal intensity versus the pump laser intensity for different selected pump detunings (see Fig. 4.8). Let us first consider the resonant case $\Delta_P^{(2p)} = 0$. For small pump intensities below $I_P = 0.05$ TW/cm² (corresponding to $\Omega_P^{(2p)}\tau_P \leq 1$), we observe a strong rise of the SFG signal with increasing pump intensity. This fits to the quadratic dependence $I_S \sim I_P^2 I_{Pr}$, expected from perturbative nonlinear optics. For higher pump intensities up to $I_P = 0.5$ TW/cm² (corresponding to $\Omega_P^{(2p)}\tau_P = 16 \gg 1$) we see a significant reduction in the slope of the dependence, which is caused by averaging over many Rabi oscillations. Increasing the pump intensity further only increases the number of Rabi cycles, but no more the average value of the atomic coherence, which already reached the maximal peak value $|\rho_{12}| = 1/2$. Thus, we

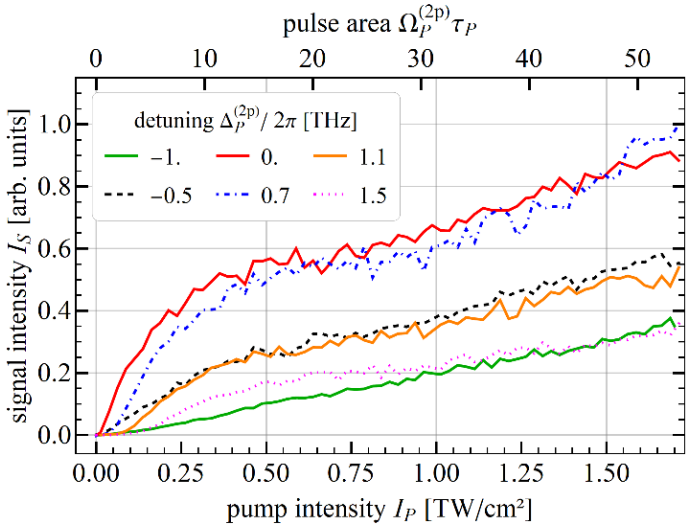

Figure 4.8: SFG signal intensity versus pump intensity (lower axis) or the corresponding pulse area (upper axis) for different two-photon detunings. The probe intensity is $I_{Pr} = 1$ TW/cm². We confirmed, that in this regime the SFG yield still depends linearly on the probe intensity. Thus, the probe laser is sufficiently weak and negligible with regard to the dynamics of the atomic coherence, strongly driven by the pump laser.

would expect the SFG signal to saturate as we observed it in Fig. 4.5. Due to contributions from the weaker wings of the spatial pump laser profile to the SFG yield, the saturation is washed out to a smaller slope in dependence of the signal yield vs. pump intensity.
We turn our attention now to the off-resonant case. When the pump laser is red detuned to $\Delta_P^{(2p)}/2\pi = -0.5$ THz and further on to $\Delta_P^{(2p)}/2\pi = -1$ THz, the SFG signal drops compared to the resonant case. The larger the absolute value of the detuning, the smaller the SFG intensity - as we would expect from simple considerations. For blue detunings $\Delta_P^{(2p)}/2\pi = 1.1$ THz or 1.5 THz we observe a similar behavior, i.e., the SFG yield drops with larger detuning. However, as a remarkable feature, for a detuning of $\Delta_P^{(2p)}/2\pi = 0.7$ THz and a pump intensity of $I_P = 1.7$ TW/cm², we get a larger SFG signal than in the resonant case. This reveals preparation of CPR by the strong, slightly off-resonant pump laser. We note that we do not get such a (large and spectrally well defined) enhancement for red detunings, as the ac Stark effect induces an asymmetry and broadening in the spectrum (compare Fig. 4.7).

4.5.3 CPR and delayed frequency conversion

The above results demonstrated enhanced conversion efficiency via a stable and maximal atomic coherence, driven by CPR. We turn our attention now to the dynamics of the coherence. As discussed in the basic introduction to CPR (section 4.2), there is a significant difference of CPR versus diabatic excitation also

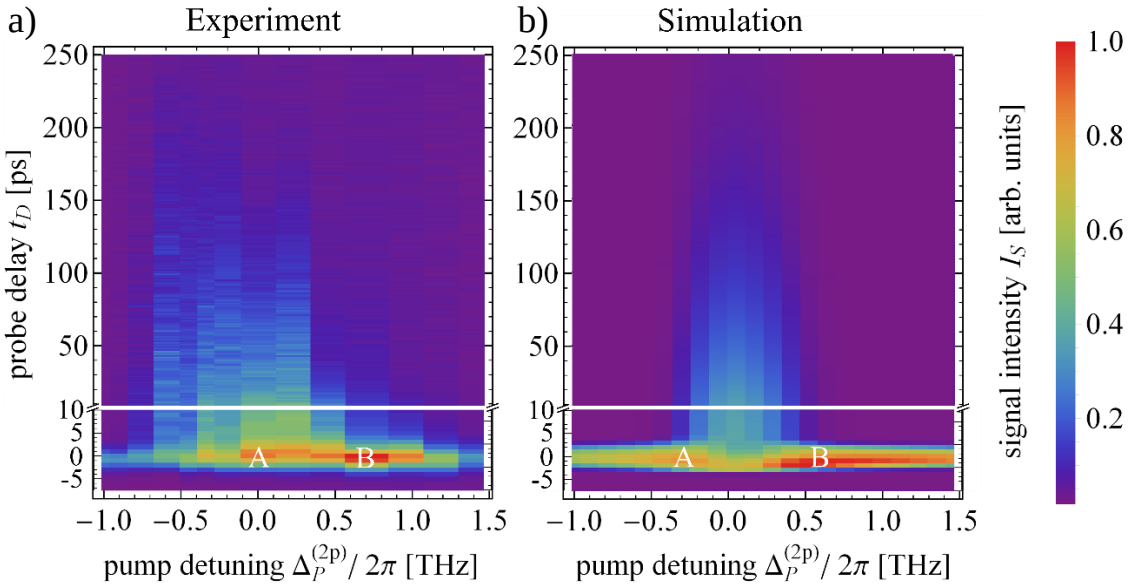

Figure 4.9: a) SFG intensity vs. probe delay and two-photon pump detuning. The pump intensity is $I_P = 1.6$ TW/cm² (corresponding to a pulse area $\Omega_P^{(2p)}\tau_P = 50$). The probe intensity is $I_{Pr} = 1$ TW/cm². Note the interrupted delay axes break for better visibility of data for short delays. Labels A and B show regions of CPR-enhanced frequency conversion (compare Fig. 4.7). Stagnation pressure $p = 200$ mbar xenon. b) Numerical simulation of SFG signal intensity vs. probe delay and two-photon pump detuning. Parameters as in Fig. 4.7, pump intensity $I_P = 1.6$ TW/cm², coherence lifetime fitted to the experimental data.

with regard to the residual atomic coherence after the excitation process. While (in general) there is always some residual coherence after diabatic excitation, in the case of CPR we expect the atomic coherence to return to zero after the process. We investigate these dynamics now by varying the delay between the probe with regard to the pump pulse. Figure 4.9 a) shows the SFG signal intensity versus pump detuning and probe pulse delay. For coincident pulses, we observe again two (off-resonant) regions A and B of enhanced frequency conversion by CPR, with an asymmetry of larger signal in region B. In the case of the CPR region B (blue detuned pump pulse), there is almost no SFG signal for a delayed probe pulse. Hence, the atomic coherence returns to zero after CPR, as expected. However, in CPR region A (red detuned probe pulse) we get quite some SFG signal also several ten picoseconds after the CPR process. Also, the numerical simulation confirms this experimental finding (see Fig. 4.9 b)). From the simulation we find, that the residual coherence in CPR region A is due to the ac Stark shift, induced by the pump laser, which pushes the two-photon resonance to a higher energy. The ac Stark shift perturbs the adiabatic evolution and, hence, CPR in region A exhibits residual diabatic couplings. This leads to residual atomic coherence after the process and frequency conversion also for a delayed probe pulse.

We determine now the coherence lifetimes (i.e., the time interval, which enables delayed frequency conversion) for different pump detunings. Figure 4.10 depicts the variation of the SFG signal intensity versus probe pulse delay for selected detunings (taken as vertical cuts from Fig. 4.9 a)). At pump detunings of $\Delta_P^{(2p)}/2\pi = -1$ THz or 1.5 THz (CPR case) we only observe a SFG signal, if the pump and probe pulses overlap, i.e., at very small pulse delay of a few picoseconds. Close to resonance at detunings $\Delta_P^{(2p)}/2\pi = -0.3$ THz and 0.2 THz (diabatic case), we observe an exponential decrease of the SFG intensity with probe delay. The "lifetime" (at 1/e of the maximal signal for coincident pulses) of the SFG process is roughly 50 ps. Note, that via the SFG intensity we observe the lifetime of $|\rho_{12}|^2$. Thus, the lifetime of $|\rho_{12}|$ corresponds to a value beyond 100 ps. For intermediate detunings of $\Delta_P^{(2p)}/2\pi = -0.8$ THz and 0.7 THz the shape of the variation of the

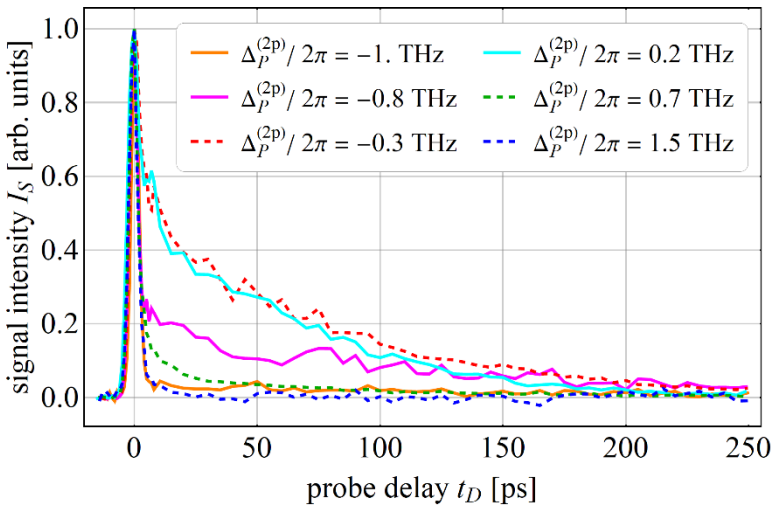

Figure 4.10: Normalized SFG signal intensity vs. probe delay for different two-photon pump detunings. The data are obtained as vertical cuts through Fig. 4.8 a).

SFG signal is inbetween the CPR and the diabatic case: For short delays below $t_D \leq 5$ ps we observe a fast drop of the SFG process, similar to the CPR case at off-resonant excitation. For longer delays beyond $t_D \geq 5$ ps we get an exponential decrease of the SFG process, similar to the diabatic case, and with a similar coherence lifetime as in the resonant case. The mixed shape mirrors the intermediate case between adiabatic (CPR) and diabatic excitation, and is also confirmed by the numerical simulation.

We discuss now the coherence lifetime, which is much shorter than the radiative lifetime of approximately 100 ns for the excited state $5p^5\,7p\,{}^2[1/2]_0$ in xenon [102]. Doppler broadening leads to dephasing of the atomic emitters in xenon at room temperature on a timescale of roughly 175 ps. Moreover, collisions lead to further dephasing. In contrast to the Doppler broadening, the collision lifetime is pressure dependent and, hence, variable in the experiment. The mean collision time T_C in a gas is given by [15]:

$$T_C \approx \frac{1}{N\sigma\bar{v}} \sim \frac{1}{p\sigma\bar{v}} \tag{4.14}$$

with the atomic number density N, the xenon-xenon collision cross section σ, the mean velocity $\bar{v}$ of the xenon atoms and the stagnation pressure p. In our atomic jet we have roughly $N \approx 10^{17}$ cm^{-3} [64]. The collision cross section for xenon is unknown, but we expect it slightly larger compared to krypton, where $\sigma = 2 \cdot 10^{-12}$ cm^2 [101]. This yields a collision-limited coherence lifetime $T_C \approx 150$ ps, which is in good agreement with the experimental data. For comparison, at normal parameters like 1 bar pressure in a gas cell, one would obtain particle densities of $N \approx 3 \cdot 10^{19}$ cm^{-3}, which would yield coherence lifetimes in the 1 ps domain.

To confirm the latter considerations on the expected coherence time, we measured the variation of the SFG intensity with the pulse delay for different stagnation pressures (see Fig. 4.11). For a stagnation pressure of $p = 100$ mbar, we determine a

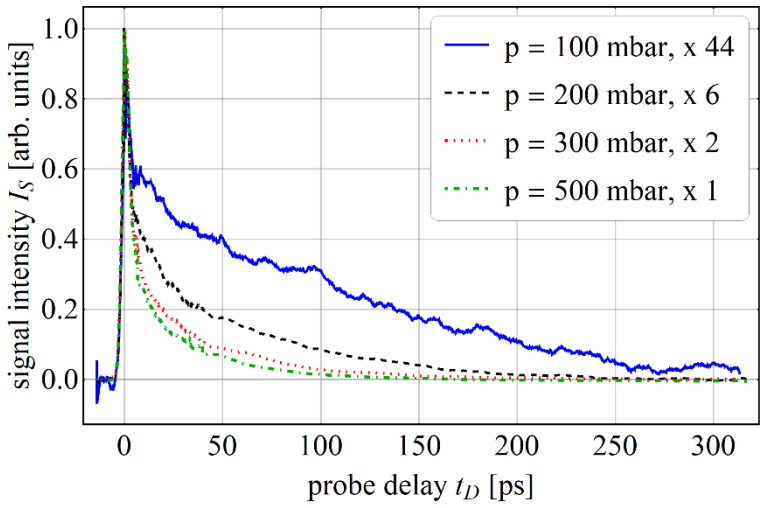

Figure 4.11: Normalized SFG signal intensity vs. probe delay for different stagnation pressures. The pump laser is tuned to resonance, i.e., $\Delta_P^{(2p)} = 0$, the pump intensity is $I_P = 1.6$ TW/cm², the probe intensity is $I_{Pr} = 1$ TW/cm².

"lifetime" (at 1/e of the maximal signal for coincident pulses) for the SFG process of roughly $T_C = 125$ ps. This is already quite close to the limit of $T_C = 175$ ps, given by the Doppler broadening. At even lower pressures, we expect a pressure-independent coherence lifetime. However, due to limited signal level we could not proceed below $p = 100$ mbar. For higher pressures, the lifetime deduced from Fig. 4.11 clearly decreases towards roughly 50 ps (at $p = 200$ mbar), 25 ps (at $p = 300$ mbar), and 15 ps (at $p = 500$ mbar). Given the error in the determination of the pressure in the interaction region, the variation fits with the expected behavior $T_c \sim 1/p$. We note that though larger pressures lead to faster decay of the atomic coherence, nevertheless operation at higher pressures is favorable for a large frequency conversion signal, even for a delayed probe pulse.

There are two further effects regarding the delay dependence, which we observed during the experimental analysis. First, if the probe laser is strong, the ac Stark shift of the probe laser can strongly change the resonance condition for coincident pulses. Second, the ac Stark shift of the probe laser can cause a dephasing of the coherences, which strongly effects the shape of the delayed frequency conversion. We discuss both effects for the case of a strong probe laser in subsection 4.5.6.

4.5.4 Free induction decay

During our experiments, we also observed a directed signal wave from our xenon gas jet at the second-harmonic frequency of the pump laser. We found, that the emitted pulse energy of the second-harmonic grows quadratically with the stagnation pressure (see Appendix F). This confirms the coherent nature of the emission. On the first glance this seems surprising, as SHG is forbidden in an isotropic medium, e.g., a gas of xenon atoms. Moreover, the SHG field also persisted after the pump pulse. Similar effects were studied before [103,104] and attributed to a symmetry breaking dc field [105,106]. Recently, control of free induction decay (FID) of the SHG signal has been investigated and proposed as a fast switch for an XUV

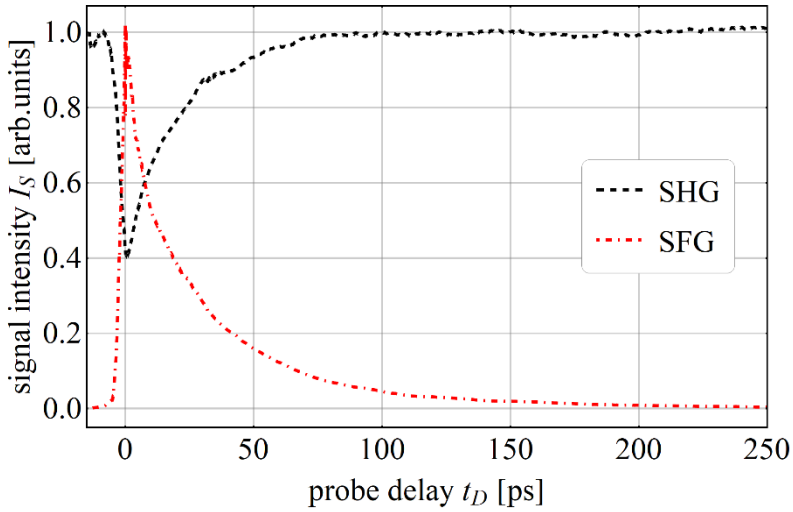

Figure 4.12: SHG and SFG signal intensity vs. probe delay. The pump laser was tuned to resonance. The pump intensity is $I_P = 1.6$ TW/cm², probe intensity $I_{Pr} = 1$ TW/cm², and stagnation pressure $p = 500$ mbar.

field [107]. In FID atomic coherences are prepared by a driving pulse in an ensemble of emitters. After the pump pulse is gone, the atomic emitters (respectively the atomic coherences prepared therein) oscillate to provide a collective emission, which decays with the coherence lifetime.

In our experiment, the ions generated by the strong pump pulse provide the symmetry breaking dc field and permit SHG. To investigate the FID nature of the SHG emission, we measured the SHG signal intensity vs. probe delay (see Fig. 4.12). The idea is that the additional probe laser reads out the atomic coherence to generate a SFG signal and, hence, reduces the SHG signal. As Fig. 4.12 shows, we get the largest SHG signal for negative probe delay, i.e., when the probe pulse precedes the pump pulse. This situation is equivalent to the probe laser switched off during the interaction with the pump pulse. In this case, the probe pulse does not affect the atomic coherences, which are fully available for intense SHG emission. For coincident pulses, the SHG yield strongly drops. Now, the probe laser reads out the coherences for SFG, and less coherence amplitude is left for SHG. For increasing probe delay the SHG signal grows again, as the probe laser reads out the atomic emitters at a late time, i.e., when more and more SHG was already emitted. Due to the competition of SHG and SFG for the atomic coherences, the SFG signal versus probe delay in Fig. 4.11 shows essentially an inverted version of the SHG signal. FID-SHG offers an interesting VUV source with an exponential pulse shape, which can be controlled rapidly by an additional Stark laser (by inducing phase shifts with the ac Stark shift) [107]. Implementation of FID-SHG with picosecond pulses is efficient, as the large pulse area (e.g., matched to provide a $\pi/2$-pulse) and still rather narrowband excitation of an atomic resonance enables preparation of maximal coherences for a strong FID-SHG signal.

Future experiments with FID-SHG shall address the question, how good the phase matching of FID-SHG is (modified refractive index for strong excitations) and whether the method works for longer interaction length (e.g., with the gas target, see Appendix B). Further, we will investigate other FID channels, like FID-THG (on a three-photon resonance, phase matching should be more demanding there), which we have not studied in detail so far. Also a combination of FID with the dressed state approach will yield some fundamental insight in coherent light-matter interaction.

4.5.5 ac Stark shift and delayed frequency conversion

In the above experiments investigating CPR and delayed frequency conversion, we did not observe a strong ac Stark shift by the probe laser, as the latter was still rather weak. We investigate now the effect of a high intensity, long wavelength probe laser and its effect on CPR and on delayed frequency conversion.

The level scheme for investigating the effect of ac Stark shifts on delayed frequency conversion for an intense probe laser is shown in Fig. 4.13 a). The two-photon pump transition between the ground state $|1\rangle = 5p^6\ {}^1S_0$ and the excited states $|2\rangle = 5p^5\ 7p\ {}^2[1/2]_0$ at a wavelength of $\lambda_P = 225$ nm is the same as in the above experiments. To probe the generated atomic coherence by SFG or DFG, we apply now a probe laser pulse with a wavelength of $\lambda_{Pr} = 800$ nm, which induces a coupling to the continuum state $|c\rangle$ for SFG and to the excited state

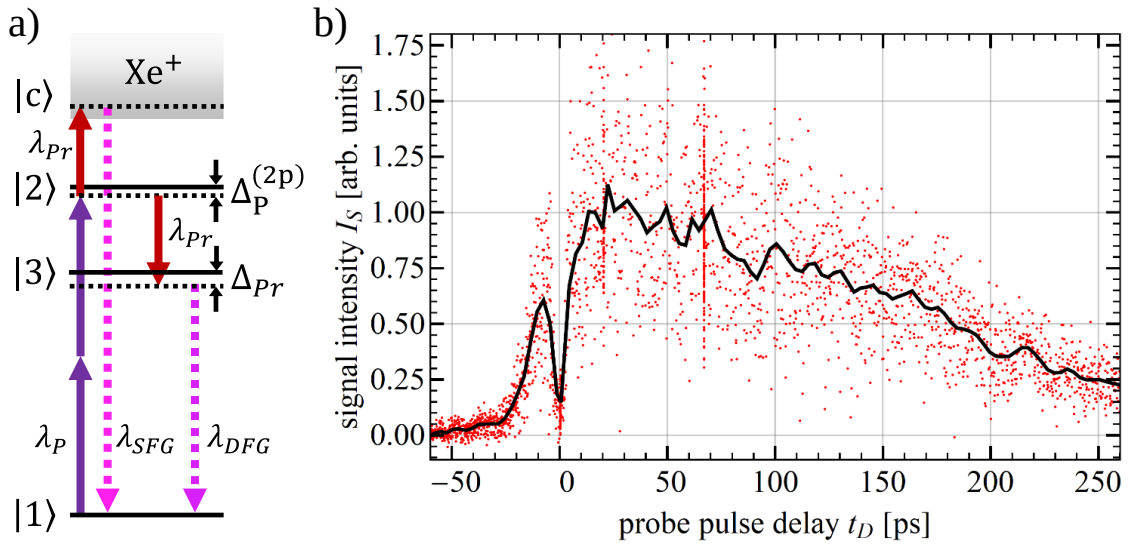

Figure 4.13: a) Coupling scheme for CPR-assisted SFG/DFG in xenon with relevant energy levels and transitions for a probe laser with a wavelength of $\lambda_{Pr} = 800$ nm. b) DFG signal intensity ($\lambda_{DFG} = 131$ nm) vs. probe delay for strong ac Stark shifts of the probe laser on resonance $\Delta_P^{(2p)} = 0$. The pump intensity is $I_P = 0.2$ TW/cm² ($\Omega_P^{(2p)}\tau_P \approx 1$), the probe laser intensity $I_C > 1$ TW/cm². The red data points are single shot data, the black line shows the moving average. The stagnation pressure is 200 mbar xenon.

$|3\rangle = 5p^5\,6s'\,{}^2[1/2]_1$ ($\lambda_{23} = 858$ nm) for DFG. The SFG signal wavelength is $\lambda_{SFG} = 99$ nm and the DFG signal wavelength is $\lambda_{DFG} = 131$ nm. We reached higher signal levels for DFG, therefore we focused our investigations on this frequency mixing channel.

Figure 4.13 b) shows the experimental results of the DFG signal intensity versus the probe pulse delay for a strong probe laser, causing large ac Stark shifts. In contrast to the above experiments, we do not observe the strongest signal intensity for coincident pulses (compare Fig. 4.10). Moreover, we see a dip, a reduced signal intensity in that case. In comparison to the maximal signal intensity for probe pulse delays of some tens of picoseconds, we see that the signal intensity for coincident pulses is roughly one fifth. For probe pulse delays above $t_D \leq 10$ ps, we observe a decrease of the signal intensity, similar to the above cases for SFG on resonance (compare Fig. 4.10). We further checked the variation of the signal intensity versus probe pulse delay for lower pump intensities and observed the same behavior. However, for lower probe intensities the dip vanishes as in the above cases. Hence, the dip for coincident pump and probe pulses is caused by the ac Stark shift of the probe laser. We reach the maximum signal intensity on the unperturbed resonance for delayed pulses. Hence, in this case delayed frequency conversion is advantageous. It is possible to shift the pump laser frequency to match with the Stark shifted resonance, but as we saw in subsection 1.2.1, the resonance enhancement will be reduced due to averaging effects in time and space.

These data show that delayed frequency conversion can be a powerful tool, if probe laser induced ac Stark shifts perturb the coincident frequency conversion strongly. In that case diabatic delayed frequency conversion can be much better than adiabatic coincident frequency conversion. However, it is possible to use the

ac Stark shift in the CPR method, to enable a temporally stable maximal coherence (Stark chirped coherent population return - SCCPR). Further, the technique of Stark chirped rapid adiabatic passage (SCRAP) [16] should work fine for the presented experimental parameters.

4.5.6 CPR with strong ac Stark shifts

Strong ac Stark shifts induced by the pump or the probe laser modify the energetic position of the two-photon resonance strongly (compare section 1.2 and the previous subsection). Figure 4.14 shows for four different ac Stark shifts the SFG signal intensity versus the two-photon pump detuning and the pump intensity. In the case without an ac Stark shift, we observe symmetric structures A and B (Fig. 4.14 a)). For an ac Stark shift equal to the ponderomotive energy of the pump laser, we obtain an asymmetric strength of the structures A and B (Fig. 4.14 b)), equivalent to the investigations in subsection 4.5.2. An important improvement in comparison to the case without the Stark laser is the increased width of structure B, enabling more stable and reliable frequency conversion at maximal coherence. Figure 4.14 c) shows the simulation for an ac Stark shift, which is four times the pump ponderomotive energy. Here, the strength of both structures, A and B, is similar,

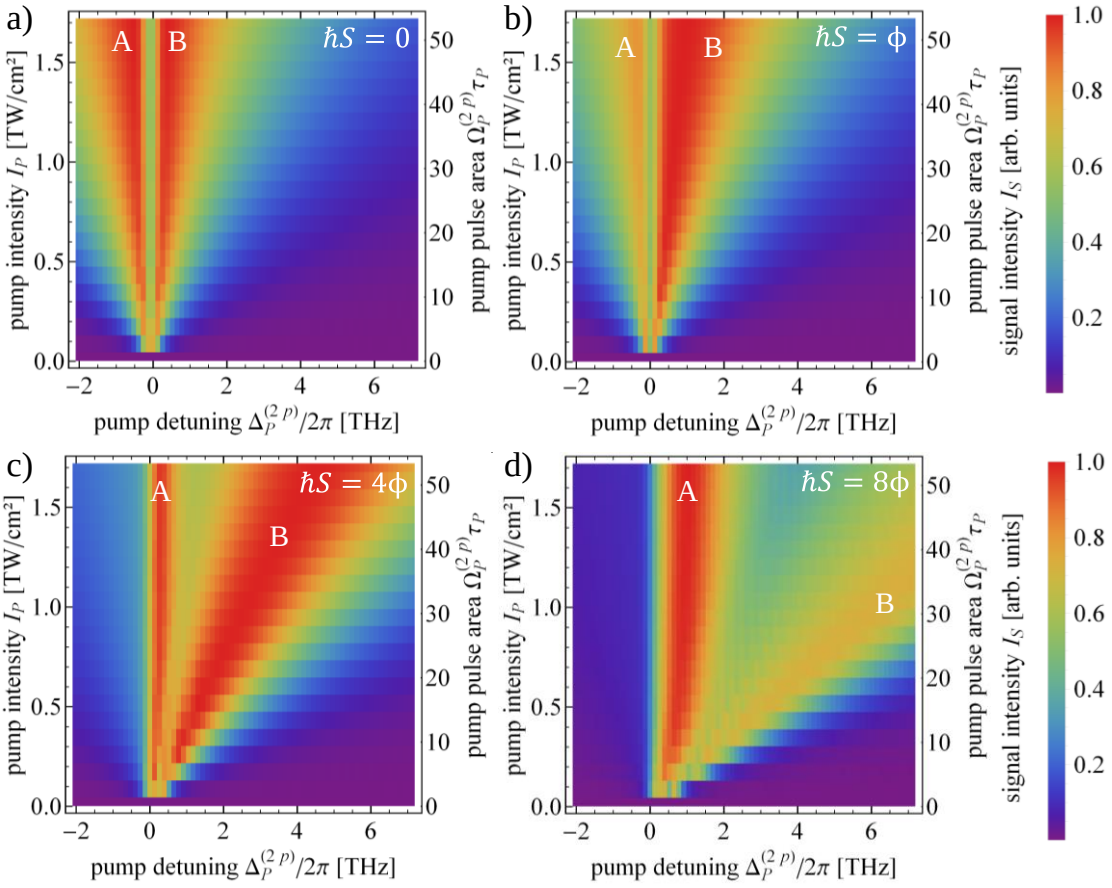

Figure 4.14: Comparison of numerical simulations of SFG signal intensity vs. pump detuning and intensity for different ac Stark shifts. a) No ac Stark shift, b) ac Stark shift is equal to the ponderomotive energy of the pump, c) ac Stark shift is four times the ponderomotive energy, d) ac Stark shift is eight times the ponderomotive energy. We did not apply spatial averaging.

although the shape is completely different. The strength of the two structures A and B can even be inverted for larger ac Stark shifts (see Fig. 4.13 d), ac Stark shift eight times the pump ponderomotive energy). Now, the structure A is stronger than structure B. This is caused by averaging effects of the strong ac Stark shift, which is time dependent. The ponderomotive energy of the pump at an intensity of $I_P = 1$ TW/cm² is $S/2\pi = 1.14$ THz. Hence, for an ac Stark shift eight times the ponderomotive energy we obtain an ac Stark shift $S/2\pi \approx 9$ THz, which exceeds the bandwidth of the CPR structures by far and lies outside of our plot region. As an interesting feature, the splitting between the two CPR structures A and B increases with a stronger ac Stark shift. Hence, the spectroscopic investigations should be easier than in the above case. However, experimentally the higher ionization rate induced by, e.g., an intense probe laser, might perturb the observation of enhanced adiabatically driven frequency conversion.

As this theoretical analysis shows, increasing the pump or probe intensity and therewith the ac Stark shift might change the spectroscopic features of CPR drastically. Further, ac Stark shifts can be used to increase the stability of CPR, so SCCPR is an improved version of CPR.

4.5.7 Combination of dressed states and CPR

So far, we investigated two methods to enhance frequency conversion via resonances. First, we showed in chapter 3, how to make use of laser controlled dressed state resonances to enhance harmonic generation and frequency conversion for an initially far detuned pump laser. Second, we showed in this chapter how to benefit optimal from the resonance applying adiabatically driven frequency conversion at maximal coherence via CPR. Now, we demonstrate with a simulation how both concepts can be combined. For the investigations on resonantly enhanced harmonic generation via dressed states we assumed small pulse areas for the pump pulse, i.e., $\Omega_P^{(3p)}\tau \ll 1$. Now we change the situation such that we have large pulse areas at the three-photon transition, i.e., $\Omega_P^{(3p)}\tau \gg 1$ (see the coupling scheme in Fig. 4.15).

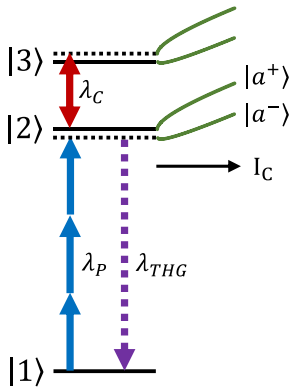

Figure 4.15: Coupling scheme for the combination of dressed states with CPR. Coupling scheme similar to section 3.3.

Figure 4.16 a) shows the results of the numerical simulations with a small pulse area (similar to our investigations in chapter 3). Without the control laser and a small pump pulse area, we observe only one peak at the Stark shifted resonance position. With the control laser, we observe again the two dressed states $|a^{\pm}\rangle$. However, both dressed states show only one peak, in contrast to CPR via a resonance. The situation changes drastically for large pump pulse areas depicted in Fig. 4.16 b). Without the control laser we observe the expected CPR enhanced double peak structure. The strength of the two peaks differs due to the pump laser induced ac Stark shift. Interestingly we see that the dip between the CPR structures is not exactly at the Stark shifted resonance position. This is due to the temporal averaging effects. With the control laser we observe two new features of the

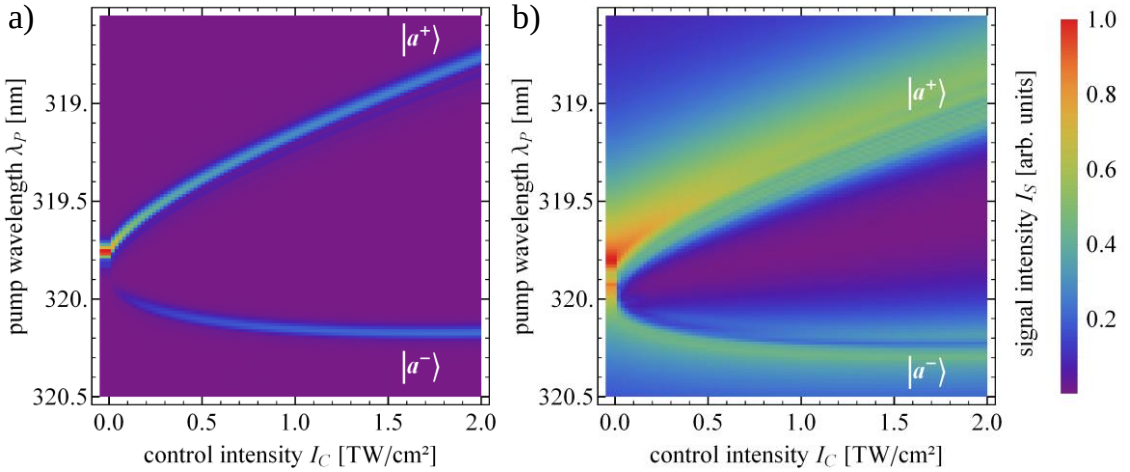

Figure 4.16: Comparison of the normalized THG signal intensity vs. control intensity and pump wavelength for a) small pump pulse area ($\Omega_P^{(3p)}\tau_P = 0.04 \ll 1$) and b) large pump pulse area ($\Omega_P^{(3p)}\tau_P = 60 \gg 1$) for a blue detuned control laser. The simulation neglects spatial averaging effects. We implemented the change of pulse areas by the change of the transition moment of the three-photon pump transition. This has the advantage that the change of the pulse area does not affect the pump intensity dependent ac Stark shift.

dressed states $|a^{\pm}\rangle$. First, they show some substructure, similar to our CPR experiments (especially dressed state $|a^-\rangle$). Second, the dressed states are strongly broadened and their energetic position or the energetic position of maximal SFG signal is shifted in regard to the case of small pump pulse areas. Nevertheless, we see that the combination of CPR and resonantly enhanced harmonic generation via dressed states works and shows some interesting features of coherent adiabatic quantum dynamics. Both techniques can be combined to obtain an optimal resonance enhancement at an almost arbitrary spectral position.

4.6 Conclusion and outlook

We demonstrated the application of coherent population return to enhance frequency conversion towards ultrashort VUV pulses at high intensities of TW/cm² and Keldysh parameters down to $\gamma = 25$. The strategic objective was to transfer a concept of adiabatic excitation, which is typically implemented at low laser intensities (MW/cm², GW/cm²) and for long pulses (μs, ns), now also to the regime of high intensities and short pulses.

In our particular experiment in xenon, we use sum frequency generation of an intense (ps) pump pulse at a wavelength of $\lambda_P = 225$ nm (with intensities in the regime of TW/cm²) on the two-photon transition and a weaker (ps) probe laser at $\lambda_{Pr} = 400$ nm to generate signal pulses in the VUV at $\lambda_S = 88$ nm. The latter serves as a simple measure for the atomic coherence in the medium. For sufficiently large pump pulse intensities and slight detuning from exact resonance, the experimentally observed SFG signal is adiabatically-enhanced compared to the case of conventional frequency conversion via the atomic resonance. We monitor the variation of the SFG signal intensity with laser intensities, detunings, and pulse delay between probe and pump pulse. The experimental data confirm the typical features

of adiabatic evolution by CPR, i.e., efficient operation off the atomic resonance, and preparation of an enhanced transient coherence during the excitation process. For CPR no residual coherence remains in the quantum system afterwards. Hence, delayed sum frequency generation is only possible by diabatic (resonant) excitation. In the latter case, we observe SFG mediated via atomic coherences with pulse delays beyond $t_D \geq 100$ ps, i.e., two orders of magnitude larger than the pulse durations. The lifetime of the macroscopic atomic coherence is mainly limited by collisions, which depend upon the gas pressure. As an important consequence of adiabatic passage at large laser intensity, the laser-induced ac Stark shifts lead to an asymmetry in the variation of the SFG yield with pump laser detuning. While for positive detuning we observe CPR, for negative detuning the adiabatic evolution is perturbed by diabatic couplings, which also enable delayed frequency conversion. Moreover, ionization losses and averaging effects across the spatial laser profiles also modify the behavior of CPR compared to simple expectations. We compare the experimental data to numerical simulations, taking ac Stark shifts and losses into account. The simulations agree very well with the experimental data. Thus, the theoretical description from the low intensity regime (MW/cm², GW/cm²) is successfully applied in the high intensity regime (TW/cm²).

As an interesting feature beyond CPR and SFG, we also observed free induction decay of the atomic coherence on the two-photon transition to generate a second-harmonic wave. This becomes possible, as the ions produced by the pump pulse induce a dc field in the otherwise isotropic medium, which breaks the symmetry. This FID-SHG is an interesting source of VUV radiation, as its emission direction can be controlled by a Stark laser [107].

Further, we showed for an intense probe laser with a wavelength of $\lambda_{Pr} = 800$ nm, how delayed frequency conversion can be beneficial for large Stark shifts induced by the probe laser in comparison to coincident SFG or DFG. Moreover, we investigated with our numerical simulation the effect of different Stark shifts onto the CPR enhancement and showed that a moderate Stark shift can increase the stability and spectral bandwidth of CPR. Finally, we presented successfully the theoretical combination of resonance enhancement via dressed states with CPR. Our findings serve to push applications of adiabatic interaction such as CPR now also towards high-intensity, ultrafast nonlinear optics.

In future experiments we will investigate circular polarization for the two-photon excitation, which closes the loss channel for THG. However, it is not completely clear how the ionization cross section will be affected by the change of polarization. Further, we will aim at higher-order frequency conversion enhanced by CPR either FHG, or two pump photons plus three probe photons, or we apply large pulse areas on three- or four-photon transitions.

Conclusion and future work

In this work, we thoroughly investigated frequency conversion towards ultrashort picosecond (ps) laser pulses in the vacuum ultraviolet (VUV) spectral regime via nonlinear optics in coherently-driven quantum systems at high intensities. We applied approaches of adiabatic quantum dynamics relying on coherent light-matter interactions, which modify the "bare" eigenstates of a quantum system to "dressed" states and exploit slow (i.e., adiabatic) population evolutions via such dressed states. This enables enhancement of typically low-order, low-intensity nonlinear optics (at MW/cm², GW/cm²), where the light field perturbs the atomic level structure only weakly. On the other hand, aiming at nonlinear optics at higher orders, e.g., high-harmonic generation, strong light fields are applied (100 TW/cm², PW/cm²), which modify the Coulomb potential of the atom strongly. In this case, resonances play no role anymore and adiabatic quantum dynamics via atomic resonances will not work. With this work, we demonstrated the implementation of adiabatic quantum dynamics and coherently prepared media for nonlinear optics in an intermediate intensity regime (TW/cm²), i.e., at Keldysh parameters approaching $\gamma \approx 1$. The fundamental question was, whether the high intensities still permit us to drive and exploit coherent-adiabatic dynamics via dressed states for enhancement of frequency conversion processes.

We investigated two approaches to enhance the frequency conversion yield applying nonlinear optics in coherently-driven quantum systems (rare gases). In the first approach, we resonantly enhanced harmonic generation via dressed states with large Autler-Townes splittings. With this approach, we demonstrated how to make atomic resonances available for an initially far detuned fixed-frequency pump laser and showed a compensation for inevitable, perturbing Stark shifts. In the second approach, we investigated frequency conversion, enhanced by coherent population return (CPR) and preparation of maximal atomic coherences at high intensities. With this approach, we showed how to maximally benefit from an atomic resonance via adiabatically driven frequency conversion, i.e., by detuning the strong pump laser slightly from the resonance.

Resonantly enhanced harmonic generation via dressed states with large Autler-Townes splittings: We demonstrated the potential of dressed states and large Autler-Townes splittings induced by a control laser to resonantly enhance harmonic generation by a pump laser. We tuned an intense control laser pulse in the vicinity of a resonance between excited states, thereby inducing dressed states. The energetic position of the dressed states varies with the control laser intensity and wavelength and is adjusted to provide a multi-photon resonance between the ground and the intermediate state for the fixed-frequency pump laser. This enhances any frequency conversion process via the dressed resonance, e.g., driven by typically high-intensity, fixed-frequency pump laser pulses. In our first coupling scheme in argon, we spectroscopically investigated the Autler-Townes splittings via third-harmonic generation (THG) of a tunable pump laser. We observed splittings of up to $\bar{\Omega}/2\pi = 18$ THz at control laser intensities up to $I_C = 7$ TW/cm² and Keldysh parameters down to $\gamma \approx 4$. Hence, Autler-Townes splittings are also applicable to

resonantly enhance harmonic generation in the high intensity regime. Via the induced dressed three-photon resonance, we increased the THG signal by more than a factor of $\eta = 80$ for off-resonant pump pulses, so almost two orders of magnitude. This enhancement is similar to directly tuning the pump laser on the bare multi-photon resonance. The energetic position of the dressed state showed a combination of Autler-Townes splittings and Stark shifts. For dressed state $|a^-\rangle$, we demonstrated that otherwise perturbing Stark shifts are compensated by the Autler-Townes splitting. Theoretically, we showed that this compensation allows an increase of the harmonic generation signal beyond the case without the control laser, so even an enhancement for tunable pump laser pulses.

In a second coupling scheme in xenon, we demonstrated the enhancement of THG and FHG for fixed-frequency pump pulses via a laser-controlled dressed state, where we adjusted the energetic position of the dressed state via the control laser detuning. We implemented very large asymmetric Autler-Townes splittings of $\bar{\Omega}/2\pi = 100$ THz for laser intensities of $I_C = 4$ TW/cm^2, corresponding to a Keldysh parameter of $\gamma \approx 7$. A huge fraction of the large Autler-Townes splitting was due to a large control laser detuning of roughly $\Delta_C = 70$ THz, which was roughly equal to the negative pump detuning of $\Delta_P^{(3p)} = -69$ THz. Hence, for each pump detuning we found a control detuning such that we obtained a dressed state resonance enhancement for THG driven by the pump laser ($\Delta_C = -\Delta_P^{(3p)}$). The large tuning range of the dressed state resonance permitted applications of the dressed resonance concept in a broad wavelength range. In systematic measurements, we observed substantial enhancement factors of $\eta \approx 40$ for THG and FHG via a dressed state resonance compared to the case without control laser. This indicates the potential of dressed resonance enhancements also for harmonic generation at higher orders and large pump laser detunings.

Further, also the pump laser alone (i.e., without the need for a second control laser pulse) induces Autler-Townes splittings and can shift the dressed states into multi-photon resonance with itself. We performed the experiment on the single laser approach on a five-photon resonance in xenon, generating the fifth-harmonic and seventh-harmonic. We observed again dressed states with large Autler-Townes splittings, so the spectrum varied drastically from the simple expectations of Stark shifted bare states.

Frequency conversion enhanced by coherent population return: With the second set of experiments, we demonstrated an approach of adiabatically driven frequency conversion via CPR at high intensities (TW/cm^2) and a Keldysh parameter down to $\gamma = 25$. CPR adiabatically drives the atomic medium to a state of maximal atomic coherence and hence, large nonlinear optical polarization on a multi-photon resonance. This supports any subsequent frequency conversion process via the resonance. In our particular experiment, we generate the sum frequency of our intense (ps) pump pulses tunable around a two-photon transition and a weaker (ps) probe laser to generate signal pulses in the VUV. For sufficiently large pump pulse areas/intensities and slight detuning from exact resonance ($\Delta_P^{(2p)} \geq 1/\tau_P$), the experimentally observed SFG is adiabatically-enhanced compared to the case

of conventional resonant frequency conversion ($\Delta_P^{(2p)} = 0$) via the atomic resonance. We investigated the variation of the SFG signal intensity with parameters like laser intensities, detunings, and pulse delay between probe and pump pulse. The experimental data demonstrate the typical features of adiabatic evolution by CPR, i.e., efficient operation off the atomic resonance, and preparation of an enhanced transient coherence during the excitation process. For CPR no residual coherence remains in the quantum system afterwards. Hence, delayed sum frequency generation is only possible by diabatic (resonant) excitation. In the latter case, we observed SFG mediated via atomic coherences with pulse delays beyond $t_D \geq 100$ ps, i.e., two orders of magnitude larger than the pulse durations. The lifetime of the macroscopic atomic coherence is mainly limited by Doppler broadening and collisions. As an important consequence of adiabatic passage at large laser intensity, the laser-induced ac Stark shifts lead to an asymmetry in the variation of the SFG yield with pump laser detuning.

Further, we showed for an intense probe laser with a wavelength of $\lambda_{Pr} = 800$ nm, how delayed frequency conversion can be beneficial for large Stark shifts induced by the probe laser in comparison to coincident frequency conversion. We investigated with our numerical simulation the effect of different Stark shifts onto the CPR enhancement and showed that a moderate Stark shift can increase the stability and spectral bandwidth of CPR. As an interesting feature beyond CPR and SFG, we also observed free induction decay of the atomic coherence on the two-photon transition to generate a second-harmonic wave (FID-SHG). Finally, we presented successfully the theoretical combination of CPR and dressed states. Our findings serve to push applications of adiabatic interaction such as CPR now also towards high-intensity, ultrafast nonlinear optics.

Outlook and future experiments: With the two sets of experiments, we demonstrated that a variety of adiabatic techniques should work with our experimental parameters, i.e., with ultrashort pulses (ps) and high-intensities (TW/cm²). Especially our coupling scheme for CPR in xenon is advantageous due to the high two-photon Rabi frequency and relatively low ionization. Hence, other adiabatic techniques, e.g., rapid adiabatic passage [33], which failed in other coupling schemes before [66], should now find appropriate experimental conditions to improve frequency conversion.

Future experiments will focus on resonance enhancements via autoionizing states (AIS), which offer high excitation energies and hence, short signal wavelengths. Advantageous for our (ps) laser pulses is that the spectral width of AIS is in the range of THz and fits consequently better (in comparison to, e.g., Doppler broadened bound state resonances) to our laser pulse bandwidth of $\delta\omega_P/2\pi = 1$ THz. After some basic nonlinear spectroscopic investigations on AIS, we will focus our research on artificial AIS induced by a control laser. This phenomenon is called laser induced continuum structure (LICS) [108], which strongly modifies the ionization cross section and the harmonic generation efficiency. A key advantage of LICS in comparison to AIS is that the energetic position of the enhancement is laser controlled (via the control wavelength) and offers in principle

a large tuning range. Further, the width of LICS is controlled by the control laser intensity dependent ionization rate.

Future research will also address the FID-SHG. This might be a promising VUV source, which is fast switchable by an external Stark shift [107]. (ps) laser pulses are a good choice for preparing the medium at a high (or even maximal) atomic coherence for FID. In comparison to (ns) laser pulses, which are too long in regard to the atomic coherence lifetime of some tens of picoseconds (due to collisions and Doppler broadening), or (fs) laser pulses, which are spectrally too broad to efficiently prepare a maximal atomic coherence on a single transition, (ps) laser pulses offer the best combination and excitation efficiencies.

With this work, we demonstrated the implementation of adiabatic quantum dynamics and coherently prepared media for nonlinear optics with ultrashort (ps) and intense (TW/cm^2) laser pulses. We showed how to exploit atomic resonances in initially far detuned cases via dressed states with large Autler-Townes splittings and how to benefit from the atomic resonance via adiabatically driven frequency conversion with the method of CPR. Future experiments will aim at higher-order processes and interactions with autoionizing states and the continuum and will pave the way for efficient higher-order frequency conversion.

Zusammenfassung

In dieser Arbeit wird die Frequenzkonversion von ultrakurzen Pikosekunden (ps) Laserpulsen in den vakuumultravioletten (VUV) Spektralbereich über nichtlineare Optik in kohärent getriebenen Quantensystemen bei hohen Intensitäten untersucht. Die dabei angewendeten Techniken der adiabatischen Quantendynamik beruhen auf der kohärenten Licht-Materie Wechselwirkung, die die sogenannten „bare states“ (diabatische Zustände) eines Quantensystems in die sogenannten „dressed states“ (adiabatische Zustände) überführt und die langsame Populationsentwicklung über die „dressed states“ ausnutzt. Dies ermöglicht typischerweise Überhöhungen für nichtlinear optische Prozesse niedriger Ordnung bei niedrigen Intensitäten (MW/cm², GW/cm²). In diesem Intensitätsbereich stört das Lichtfeld die atomare Energieniveaustruktur und das atomare elektrische Potential nur schwach. Andererseits werden für nichtlinear optische Prozesse höherer Ordnung, beispielsweise für die Erzeugung hoher Harmonischer, extrem hohe Intensitäten (100 TW/cm², PW/cm²) genutzt. Diese modifizieren das Coulomb Potential des Atoms stark, so dass in diesem Fall Resonanzen keine Rolle spielen und adiabatische Quantenmechanik über diese nicht funktioniert. In dieser Arbeit wird die Implementierung von adiabatischer Quantendynamik und kohärenter Präparation von Quantensystemen für nichtlineare Optik in einem Zwischenbereich mit hohen, aber nicht extremen Intensitäten (TW/cm²) demonstriert. Dies wird anschaulich über den Keldysh Parameter ausgedrückt, der ein Verhältnis zwischen dem Ionisationspotential des Atoms und der kinetischen Energie eines Elektrons im Laserfeld darstellt, ausgedrückt. In unseren Experimenten lag der Keldysh Parameter in der Nähe von $\gamma = 1$. Die Kernfrage dieser Arbeit ist nun, ob bei diesen hohen Intensitäten Techniken der kohärent adiabatischen Quantendynamik weiterhin anwendbar sind um Frequenzkonversionsprozesse zu überhöhen.

Es werden zwei Techniken zur Überhöhung von Frequenzkonversionsprozessen untersucht, die auf nichtlinearer Optik über kohärent getriebene Quantensysteme (in Edelgasen) basieren. Die erste Technik beruht auf der resonanten Überhöhung der Erzeugung Harmonischer über „dressed states“ mit großen Autler-Townes Aufspaltungen. Mit dieser Technik können atomare Resonanzen für weit verstimmte, festfrequente Pumplaser nutzbar gemacht werden und unvermeidliche, störende Stark-Verschiebungen kompensiert werden. Die zweite Technik verwendet die kohärente Populationsrückkehr (engl.: coherent population return, CPR) zur Überhöhung der Frequenzkonversion durch die Präparation maximaler atomarer Kohärenzen. Mit diesem Ansatz wird gezeigt, wie die Frequenzkonversion optimal durch eine atomare Resonanz bei starker Kopplung überhöht wird. Interessanterweise ist dies nicht auf der Resonanz der Fall, sondern für eine leichte Verstimmung, die eine adiabatische Wechselwirkung ermöglicht.

Resonant überhöhte Erzeugung Harmonischer über „dressed states“ mit großen Autler-Townes Aufspaltungen: Von einem Kontrolllaser induzierte „dressed states“ mit großen Autler-Townes Aufspaltungen haben das Potential Frequenzkonversionseffizienzen durch resonante Überhöhung deutlich zu verbessern. Ein intensiver Kontrolllaser wird auf eine Resonanz zwischen zwei angeregten Zuständen abgestimmt

und eingestrahlt. Dadurch werden zwei „dressed states“ induziert, deren energetische Position durch die Intensität und durch die Wellenlänge (Verstimmung) des Kontrolllasers bestimmt wird. Dadurch kann eine Mehrphotonen-Resonanz für einen festfrequenten Pumplaser zwischen dem Grundzustand und einem Zwischenzustand erzeugt werden, so dass jeder Frequenzkonversionsprozess über diesen „dressed state“ überhöht wird. Im ersten Kopplungsschema in Argon wird die Autler-Townes Aufspaltung über die Erzeugung der dritten Harmonischen (engl.: third-harmonic generation, THG) eines durchstimmbaren Pumplasers spektral untersucht. Bei Intensitäten des Kontrolllasers von bis zu $I_C = 7\,\mathrm{TW/cm^2}$ (entspricht einem Keldysh Parameter von $\gamma \approx 4$) erreichten wir Autler-Townes Aufspaltungen von bis zu $\bar{\Omega}/2\pi = 18\,\mathrm{THz}$. Über die induzierte „dressed state“ Dreiphotonen-Resonanz erreichten wir Überhöhungen der THG von bis zu einem Faktor $\eta = 80$ für nicht-resonante Pumplaserpulse, also fast eine Überhöhung um zwei Größenordnungen. Dies entspricht in etwa dem Fall, dass der Pumplaser direkt auf der „bare state“ Multiphotonen-Resonanz eingestrahlt wird. Somit sind „dressed state“ geeignet und anwendbar für resonant überhöhte Erzeugung Harmonischer im Bereich hoher Intensitäten. Die energetische Position der „dressed states“ zeigt eine Kombination aus Autler-Townes Aufspaltung und Stark-Verschiebungen. Für den „dressed state“ $|a^-\rangle$ wurde gezeigt, dass sonst störende Stark-Verschiebungen kompensiert werden können. Mit einer Simulation wurde zudem demonstriert, dass diese Kompensation unter geeigneten Bedingungen sogar die Erzeugung Harmonischer über den resonanten Fall ohne Kontrolllaser überhöhen kann.

Im zweiten Kopplungsschema (in Xenon) wurde die Überhöhung der THG und der fünften Harmonischen (FHG) für einen festfrequenten Pumplaser über Kontrolllaser induzierte „dressed states“ untersucht. Dabei wurde beobachtet, dass die energetische Position der „dressed states“ insbesondere von der Verstimmung des Kontrolllasers abhängig ist. Es wurden sehr große, asymmetrische Autler-Townes Aufspaltungen von bis zu $\bar{\Omega}/2\pi = 100\,\mathrm{THz}$ für Intensitäten des Kontrolllasers von bis zu $I_C = 4\,\mathrm{TW/cm^2}$ (Keldysh Parameter $\gamma \approx 7$) erzielt. Ein Großteil der Autler-Townes Aufspaltungen macht die große Verstimmung des Kontrolllasers aus, die mit $\Delta_C = 70\,\mathrm{THz}$ etwa der negativen Dreiphotonen-Verstimmung des Pumplasers entspricht ($\Delta_P^{(3p)} = -69\,\mathrm{THz}$). Somit kann für jede Verstimmung des Pumplasers, die Verstimmung des Kontrolllasers so eingestellt werden, dass durch eine „dressed states“ Resonanz die THG überhöht wird ($\Delta_\mathrm{P}^{(3\mathrm{p})} \approx -\Delta_C$). Der große, über den Kontrolllaser einstellbare Verstimmungsbereich der „dressed states“ Resonanz ermöglicht einen entsprechend großen Durchstimmbereich im VUV Spektralbereich. Weiter konnten in systematischen Messungen Überhöhungen von $\eta \approx 40$ für THG und FHG über die „dressed states“ erzielt werden (im Vergleich zum Fall ohne Kontrolllaser). Dies demonstriert das Potential von „dressed states“ Resonanzen auch für die Erzeugung höherer Harmonischer. Weiter wurde untersucht und gezeigt, dass auch der Pumplaser selbst Autler-Townes Aufspaltungen induzieren kann (ohne einen zusätzlichen Kontrolllaser) und diese Mehrphotonen-resonant treffen kann. Dabei wurde in einem Kopplungsschema in Xenon eine Überhöhung der FHG über eine Fünfphotonen-Resonanz erzielt. Das FHG Spektrum zeigt deutlich eine Autler-Townes Aufspaltung, die von der einfachen Erwartung einer Stark-verschobenen Resonanz abweicht.

Frequenzkonversion überhöht durch kohärente Besetzungsrückkehr (CPR): Mit einer zweiten Experimentreihe wurde CPR zur Überhöhung kohärent adiabatischer Frequenzkonversion bei hohen Intensitäten (TW/cm²) und niedrigem Keldysh Parameter $\gamma = 25$ untersucht und demonstriert. Mit CPR wird das atomare Medium adiabatisch in einem Zustand transienter, maximaler atomarer Kohärenz präpariert. Somit ist es möglich, große nichtlineare Polarisationen auf Mehrphotonen-Resonanzen zu erzeugen, so dass alle Frequenzkonversionsprozesse darüber überhöht werden. In dem hier gezeigten Experiment wird die Summenfrequenz eines Pumplasers, der um eine Zweiphotonen-Resonanz durchstimmbar ist, und eines schwächeren Probelasers erzeugt, um Signalpulse im VUV Spektralbereich zu erhalten. Für genügend große Pumppulsflächen/-intensitäten und leichte Verstimmungen von der exakten Resonanz ($\Delta_P^{(2p)} \geq 1/\tau_P$) wird die Erzeugung der Summenfrequenz (engl.: sum frequency generation, SFG) adiabatisch überhöht im Vergleich zur gewöhnlichen, resonanten Frequenzkonversion ($\Delta_P^{(2p)} = 0$). Untersucht wurde die Variation der SFG von Parametern wie der Intensität des Pumplasers, der Verstimmung des Pumplasers und der Verzögerung zwischen dem Pump- und Probelaserpuls. Die experimentellen Daten demonstrieren typische Eigenschaften adiabatischer Anregung eines Quantensystems mittels CPR. Das heißt, dass die Präparation einer maximalen transienten atomaren Kohärenz leicht verstimmt von der Resonanz stattfindet. Für CPR verbleibt keine atomare Kohärenz im Quantensystem nach dem „Ausschalten“ des Pumppulses. Somit ist eine verzögerte Erzeugung der Summenfrequenz nur für eine diabatische (resonante) Anregung möglich. In diesem Fall wurde SFG über atomare Kohärenzen mit Pulsverzögerungen von über $t_D \geq 100$ ps beobachtet. Das heißt, dass die Lebensdauer der atomaren Kohärenz circa zwei Größenordnungen über der Dauer der Laserpulse liegt. Die Lebensdauer der atomaren Kohärenz hängt hauptsächlich von der Dopplerverbreiterung und Stößen (abhängig vom Druck) ab. Eine wichtige Beobachtung in Bezug auf die Anwendung adiabatischer Techniken bei hohen Intensitäten war, dass die laserinduzierten Stark-Verschiebungen zu einer Asymmetrie in der Variation des SFG Signals über der Verstimmung des Pumplasers führt.

Weiter wurde für einen intensiven Probelaser mit einer Wellenlänge von $\lambda_{Pr} = 800$ nm gezeigt, dass die verzögerte Frequenzkonversion vorteilhaft sein kann, wenn große Stark-Verschiebungen durch den Probelaser die koinzidente Frequenzkonversion stören. Mit einer Simulation wurde der Effekt verschiedener Stark-Verschiebungen auf die CPR Überhöhung untersucht und es wurde gezeigt, dass diese die Stabilität hinsichtlich Intensitäts- und Frequenzschwankungen erhöhen und die spektrale Bandbreite der CPR Überhöhung vergrößern können. Jenseits von CPR und SFG wurde im Experiment der freie Induktionszerfall der atomaren Kohärenz des Zwei-Photonen Übergangs beobachtet, bei dem ein Feld entsteht, dass mit der doppelten Frequenz des Pumplasers oszilliert (Erzeugung der zweiten Harmonischen, engl.: second-harmonic generation, SHG). Schließlich wurde erfolgreich die Kombination von CPR mit der resonanten Frequenzkonversion über „dressed states“ demonstriert. Die gezeigten Ergebnisse werden dazu beitragen, dass zukünftig weitere Anwendungen von adiabatischen Wechselwirkungen in den Bereich der hochintensiven, ultraschnellen nichtlinearen Optik übertragen werden.

Appendix

A ac Stark shift and ponderomotive energy

In this Appendix, we derive ac Stark shifts and discuss their relation to the ponderomotive energy. The calculations and approximations based on a paper by Pan, Armstrong and Eberly [40]. In comparison, we neglect here for simplicity the terms in the Hamiltonian, which describe the nucleus and the multi-electron system of the atom. Hence, we start with the following Hamiltonian (note that bold letters represent vectors):

$$\hat{\mathrm{H}} = \frac{1}{2m_e}\left(\hat{\mathbf{p}} - e\hat{\mathbf{A}}\right)^2 + V(r) = \frac{1}{2m_e}\left(\hat{\mathbf{p}}^2 - 2e\hat{\mathbf{p}}\hat{\mathbf{A}} + e^2\hat{\mathbf{A}}^2\right) + V(r) \qquad \text{(A.1)}$$

with the electron mass m_e, the electron charge e, the momentum operator $\hat{\mathbf{p}}$ and the vector potential for the radiation field $\hat{\mathbf{A}}$, and the potential V. Note that $\hat{\mathbf{p}}$ and $\hat{\mathbf{A}}$ commute for classical fields, i.e., $\hat{\mathbf{p}}\hat{\mathbf{A}} + \hat{\mathbf{A}}\hat{\mathbf{p}} = 2\hat{\mathbf{p}}\hat{\mathbf{A}}$. There are two terms in the Hamiltonian depending on the vector potential $\hat{\mathbf{A}}$, which describe the light-matter interaction and will be discussed now in detail. Note that we approximate the reduced mass in the calculations by Pan, Armstrong and Eberly with the electron mass m_e.

Term ~ $\hat{\mathbf{A}}^2$: From the definition of the electric field via the electric potential Φ and the vector potential, we obtain by integration and without charges, i.e., $\Phi = 0$:

$$\hat{\mathbf{E}} = -\boldsymbol{\nabla}\Phi - \dot{\hat{\mathbf{A}}} \;\Rightarrow\; \hat{\mathbf{A}} = -\int \hat{\mathbf{E}}\, dt \qquad \text{(A.2)}$$

For an electric field given by $E(t) = E_0 \sin(\omega t)$ (dipole approximation), we get $A(t) = E_0/\omega \cos(\omega t)$. Thus, we obtain for the term in the Hamiltonian:

$$\frac{e^2\hat{\mathbf{A}}^2}{2m_e} = \frac{e^2\hat{\mathbf{E}}_0^2}{2m\omega^2}\cos^2(\omega t) \qquad \text{(A.3)}$$

Time averaging yields that the cosine squared is $1/2$, so we obtain a result, which is exactly equal to the ponderomotive energy ϕ (eqn. 1.14). Note that this shift happens for all levels simultaneously. Hence, it is just an energy offset and is not observable in the experiment.

Term ~ $\hat{\mathbf{p}}\hat{\mathbf{A}}$: We now consider the term proportional to $\hat{\mathbf{p}}\hat{\mathbf{A}} = \hat{\mathbf{p}}\hat{\mathbf{E}}_0 \cos(\omega t)/\omega$. Second order perturbation theory yields the following energy shift for level $|n\rangle$ via all other states $|m\rangle$:

$$\Delta W_n = \frac{\hbar}{2}\frac{E_0^2}{\hbar^2\omega^2}\sum_m |\mu_{nm}|^2 \frac{\omega_{nm}^3}{\omega_{nm}^2 - \omega^2} \qquad \text{(A.4)}$$

with the transition frequency $\omega_{nm} = E_n - E_m$. Now we discuss different approximations for the laser frequency, i.e., a low frequency $\omega \ll \omega_{nm}$, a high frequency $\omega \gg \omega_{nm}$ and a near resonance frequency $\omega \approx \omega_{nm}$.

Low frequency approximation ($\omega \ll \omega_{nm}$): This approximation is of interest for our level schemes in rare gases, because for the ground state $|g\rangle$ all excited states $|e\rangle$ are far off-resonant. First, we rewrite the following expression:

$$\frac{\omega_{nm}^3}{\omega_{nm}^2 - \omega^2} = \omega_{nm} \frac{1}{1 - (\omega/\omega_{nm})^2} \tag{A.5}$$

We now apply a Taylor series expansion of the fraction around zero, i.e., $\omega/\omega_{nm} \to 0$, and only take into account the first two orders. We obtain:

$$\Delta W_n \approx \frac{\hbar}{2} \frac{E_0^2}{\hbar^2 \omega^2} \sum_m |\mu_{nm}|^2 \left(\omega_{nm} + \frac{\omega^2}{\omega_{nm}} \right) \tag{A.6}$$

For the first term ($\sim \omega_{nm}$) we apply the Thomas-Reiche-Kuhn sum rule:

$$\sum_m |\mu_{nm}|^2 \omega_{nm} = -\frac{e^2 \hbar}{2m_e} \tag{A.7}$$

Thus, the first term yields:

$$-\frac{\hbar}{2} \frac{E_0^2}{\hbar\omega^2} \frac{e^2\hbar}{2m_e} = -\frac{e^2 E_0^2}{4m\omega^2} = -\phi \tag{A.8}$$

This term cancels the shift of the quadratically dependence on $\widehat{\mathbf{A}}$, present for all atomic states. The second term of eqn. A.6 gives:

$$\frac{\hbar}{2} \frac{E_0^2}{\hbar^2 \omega^2} \sum_m |\mu_{nm}|^2 \frac{\omega^2}{\omega_{nm}} = \frac{\hbar}{2} \frac{E_0^2}{\hbar^2} \sum_m \frac{|\mu_{nm}|^2}{\omega_{nm}} = \hbar \sum_m \frac{|\Omega_{nm}|^2}{2\omega_{nm}} \tag{A.9}$$

With the detuning $\Delta_{nm} = \omega - \omega_{nm} \approx -\omega_{nm}$ (for $\omega \ll \omega_{nm}$) we obtain:

$$\hbar \sum_m \frac{|\Omega_{nm}|^2}{2\omega_{nm}} \approx -\hbar \sum_m \frac{|\Omega_{nm}|^2}{2\Delta_{nm}} \tag{A.10}$$

with the Rabi frequency $\Omega_{nm} = \mu_{nm} E_0/\hbar$. This result resembles the expected ac Stark shift from the low intensity regime [37–39].

High frequency approximation ($\omega \gg \omega_{nm}$): For optical frequencies, this approximation applies for highly excited states, e.g., Rydberg states, with small energy gaps to the neighbor states. We approximate for the level shift:

$$\Delta W_n = \frac{\hbar}{2} \frac{E_0^2}{\hbar^2 \omega^2} \sum_m |\mu_{nm}|^2 \frac{\omega_{nm}^3}{\omega_{nm}^2 - \omega^2} \approx -\frac{\hbar}{2} \frac{E_0^2}{\hbar^2 \omega^2} \sum_m |\mu_{nm}|^2 \frac{\omega_{nm}^3}{\omega^2} \tag{A.11}$$

$$= -\frac{\hbar}{2} \sum_m \frac{E_0^2 |\mu_{nm}|^2}{\hbar^2 \omega^2} \omega_{nm} \frac{\omega_{nm}^2}{\omega^2} = -\frac{\hbar}{2} \sum_m \frac{|\Omega_{nm}|^2}{\omega^2} \omega_{nm} \frac{\omega_{nm}^2}{\omega^2} \tag{A.12}$$

For $\Omega \ll \omega$ (compare rotating wave approximation), we get $|\Omega_{nm}|^2/\omega^2 \to 0$ and for $\omega_{nm} \ll \omega$, we get $\omega_{nm}^2/\omega^2 \to 0$. Hence, the shift of the state $|n\rangle$ will only be a tiny fraction of the transition frequency ω_{nm}. We conclude that the total shift between

the ground state $|g\rangle$ and highly excited states $|e\rangle$ is equal to the ponderomotive energy ϕ.

Near resonance frequency approximation ($\omega \approx \omega_{nm}$): First, we approximate the possible transitions only by one dominant (near resonant) transition with transition frequency $\omega_{nm} = \omega_0$. This approximation allows us to neglect the sum over all states $|m\rangle$. Hence, we obtain:

$$\Delta W_n = \frac{\hbar}{2}\frac{E_0^2|\mu_0|^2}{\hbar^2\omega^2}\frac{\omega_0^3}{\omega_0^2-\omega^2} = \frac{\hbar}{2}\frac{E_0^2|\mu_0|^2}{\hbar^2\omega^2}\frac{\omega_0^3}{(\omega_0-\omega)(\omega_0+\omega)} \tag{A.13}$$

We approximate $\omega_0 + \omega \approx 2\omega \approx 2\omega_0$. Thus, we obtain:

$$\Delta W_n \approx \frac{\hbar}{2}\frac{E_0^2\,|\mu_0|^2}{\hbar^2}\frac{1}{2(\omega_0-\omega)} = -\frac{\hbar}{2}\frac{|\Omega_0|^2}{2\Delta} \tag{A.14}$$

Note that this is the shift for the state $|n\rangle$. The other state of the near resonant transition will experience a shift with the same magnitude, but with the opposite sign. Thus, we obtain the total ac Stark shift:

$$\mathrm{S} = \hbar\frac{|\Omega_0|^2}{2\Delta} \tag{A.15}$$

This is the ac Stark shift, which is expected from theory at low intensities [37–39].

We conclude that our approximation of the ac Stark shift by the ponderomotive energy is valid for the excited states in rare gases. However, it is a rough estimation because we fully neglect the atomic level structure.

B Modification of the gas jet

The modification of the gas jet shall increase the NL product (particle density N and interaction length L) and hence, the conversion efficiency. One approach is to confine the gas in such a way, that it overlaps better with the laser beam [109,110]. That has also be done in this work, where we built a modified gas target, which we put behind the nozzle (see Fig. A a)+b)) [111]. This yielded higher particle densities and interaction length, showing clearly the relevance of phase matching in that geometry (see Fig. A c)). For low pressures and NL products, we clearly observe a strong resonance enhancement. At a pressure of about $p = 110$ mbar, THG on resonance reaches the maximum, followed by a minimum at $p = 225$ mbar. In the following, we observe oscillations, which are typical for a phase mismatch. We checked the change of the oscillation period for different detunings, i.e., the closer we are to the resonance, the higher is the oscillation period. Off resonance, we observe a nearly quadratic rise. Thus, we obtain higher signal levels than on resonance above $p \geq 300$ mbar. Although the modified gas jet increases the NL product, we performed the measurements in chapters 3 and 4 with the simple gas jet, because the signal levels were sufficient with the lower NL product and we did not want perturbing phase-matching effects (compare Fig. A c)).

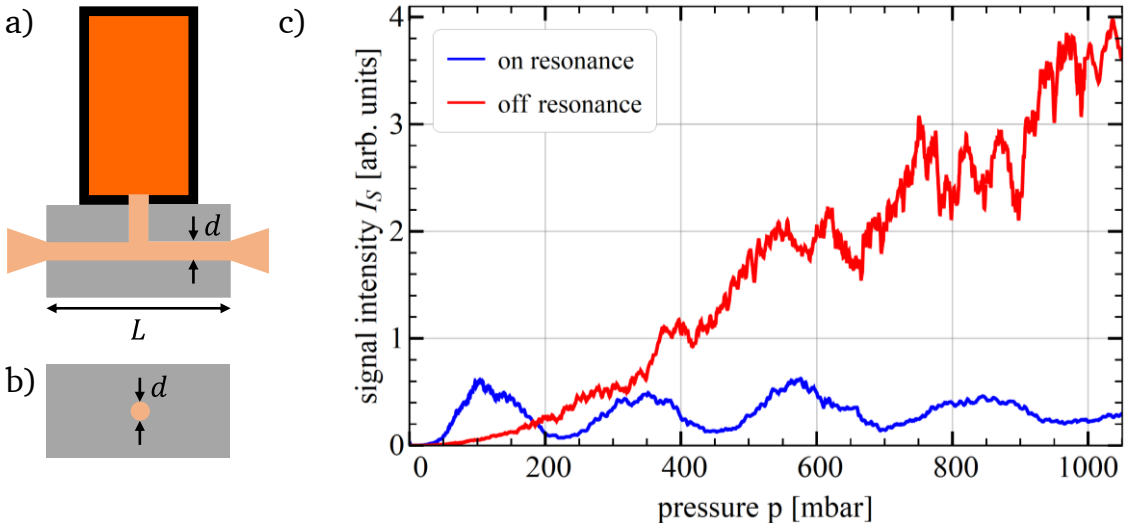

Figure A: a) Pulsed nozzle with modified gas jet. The core diameter is $d = 300$ µm, the interaction length is $L = 1.6$ mm. b) Front view of the modified gas jet. The confinement is in two dimensions. c) THG signal intensity versus stagnation pressure for different detunings to a three-photon resonance in argon (with the excited state $3p^5 4s\ ^2[3/2]_1$, compare section 3.3) with the modified target behind the nozzle.

C Simulation of THG for a far-off-resonant control laser

For the numerical simulations in section 3.4, we utilized the simple Hamiltonian for the three-level system, shown in eqn. 3.1. This is sufficient to describe the main enhancement via dressed state $|a_A^-\rangle$, but cannot describe the small enhancement of dressed state $|a_B^-\rangle$. However, we decided to neglect further couplings for simplicity.

In the simulation, we use the following measured laser pulse parameters: pulse durations $\tau_P = 3$ ps, $\tau_C = 2$ ps, beam diameters $d_P = 50\,\mu$m and $d_C = 50\,\mu$m ($1/e^2$ of intensity). The Hamiltonian involves a larger number of parameters, e.g., transition moments, which occur in Rabi frequencies, which are only partly available from literature. Hence, we required some reasonable estimations and fits of parameters. The three-photon pump Rabi frequency is again expected to be very small, i.e., we estimated $\Omega_P^{(3p)}\tau_P \ll 1$, due to the huge detunings of the pump laser from any single-photon resonance between the ground state and excited states. Thus, exact choice of $\Omega_P^{(3p)}$ only changes the peak value of the THG signal, but does not effect the line shapes obtained from the simulation (compare subsection 3.3.4). However, the pump laser intensity is relevant for the ac Stark shift.

For the control Rabi frequency, we fitted the transition dipole moment to match with the experimentally observed Autler-Townes splitting. We found $\mu_C = 7 \cdot 10^{-30}$ Cm. Unfortunately, there are no literature values for comparison. However, the order of magnitude is typical and is therefore a good estimation. We set the control transition wavelength to $\lambda_{23} = 728$ nm and the pump transition wavelength to $\lambda_P = 388.7/3$ nm. The ac Stark shift S varies proportional to the pump and the control intensity, with a peak value approximated by the ponderomotive energy ϕ. For the total ac Stark shift, we add the ponderomotive energy induced by the pump and the control laser. We used the approximation $\hbar S = \phi$ for the pump- and control-induced shifts. As exception, by comparison of the experimental data with our simulation, we added an additional small offset of 1/5 of the ponderomotive shift at state $|3\rangle$ to the total control detuning.

D VUV output spectrum for the dressed state concept

Besides the emission of THG and FHG, we observed also other frequency conversion channels, driven by the pump and control laser (experiments in section 3.4.). Figure B shows the emission spectrum of the VUV output without and with the control field (for parallel and perpendicular polarization of the control laser in regard to the pump laser). Without the control field there are only two peaks corresponding to THG and FHG of the pump laser. With the control field both peaks are much higher, meanwhile the enhancement is larger for parallel polarization (compare Fig. 3.11). However, also other frequency mixing channels open, i.e., sum and difference frequency generation of multiple pump and control photons. For an isotropic medium like xenon, we expect those mixing channels only, if we do not have perfect perpendicular polarizations. Hence, the polarization in the perpendicular case is almost, but not perfectly perpendicular, due to the polarizers and the beam combination with the dichroic mirror. Nevertheless, we see a reduction of the frequency mixing channels for perpendicular polarizations by about one order of magnitude. In general, the frequency mixing channels are loss channels, which perturb harmonic generation by the reduction of the coherence. Interestingly here, if we try to suppress the frequency mixing channels by perpendicular polarizations, we do not observe a larger enhancement of the THG and FHG. On the contrary, we observe a decrease of the desired harmonic signals. Thus, the loss channels of frequency mixing do not seem to be the major issue here, although we observed the perturbing character of the frequency mixing channels during this work for an ac Stark shift compensation experiment not shown here (for details see [57]).

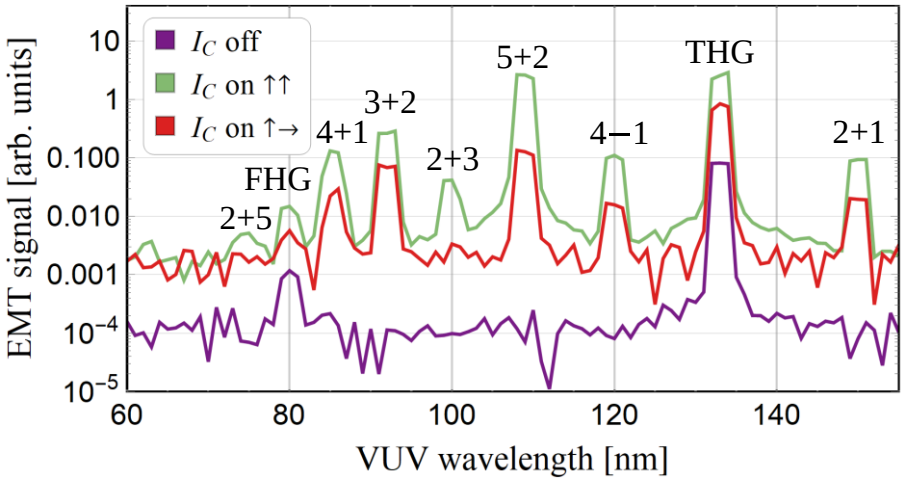

Figure B: VUV spectra without and with control laser (parallel and perpendicular polarization). Note the logarithmic scale for the signal. The noise level varies due to different supply voltages at the EMT and rescaling. Labels $N_P + N_C$ indicate mixing of N_P pump photons with N_C control photons. The intensities are $I_P = 1.4\ TW/cm^2$ and $I_C = 2\ TW/cm^2$. The width of the peaks is due to the width of the adjustable exit slit of the VUV spectrometer (see section 2.3). The EMT signal is not calibrated regarding different VUV wavelengths, so the relative peak heights should not be compared (an estimation for the detection efficiency can be found in [23]*).*

E Simulation of FHG in the single laser scheme

The basic concept of the numerical simulation of FHG via dressed states is the same as for THG, and requires in principle only a Hamiltonian for a three-level system (with a five-photon Rabi frequency between the ground state and the first excited state). However, we include in our simulation six more excited states to account for the more complicated couplings to the manifold of states $|3\rangle$ (see section 3.5.). The Hamiltonian for the nine-level system in Dirac representation with dipole and rotating wave approximation reads [34]:

$$\widehat{\mathrm{H}}(t) = \frac{\hbar}{2}\begin{pmatrix} -2\Delta_P^{(5p)} - 2S(t) & \Omega_P^{(5p)}(t) & 0 & 0 & \\ \Omega_P^{(5p)^*}(t) & 0 & \Omega_{C1}(t) & \Omega_{C2}(t) & \cdots \\ 0 & \Omega_{C1}^*(t) & 2\Delta_{C1} & 0 & \\ 0 & \Omega_{C2}^*(t) & 0 & 2\Delta_{C2} & \\ & \vdots & & & \ddots \end{pmatrix} \tag{E.1}$$

We skipped the entries up to Rabi frequency Ω_{C7} and detuning Δ_{C7}, describing the seventh control transition. The Hamiltonian is given with the five-photon pump Rabi frequency $\Omega_P^{(5p)}$, the single-photon control Rabi frequency Ω_{Ci} (i is an iterator for the seven control transitions), the five-photon pump detuning $\Delta_P^{(5p)}$, the single-photon control detuning Δ_{Ci}, and the time dependent ac Stark shift S.

In the simulations, we use the following measured laser pulse parameters: pulse duration (FWHM) $\tau_{P/C} = 2$ ps and beam diameter $d_{P/C} = 32\ \mu$m ($1/e^2$ of intensity). The Hamiltonian involves a larger number of parameters, e.g., transition moments, which occur in Rabi frequencies, which are only partly available from literature. Hence, we required some reasonable estimations and fits of parameters. The five-photon pump Rabi frequency is expected to be very small, i.e., we estimated $\Omega_P^{(5p)}/2\pi \ll 1$ THz, due to the huge detunings of the pump laser from any single-photon resonance between the ground state and excited states. Hence, exact choice of $\Omega_P^{(5p)}$ only changes the peak value of the FHG signal, but does not affect the line shapes obtained from the simulation. For the control Rabi frequencies, we fitted transition dipole moments to match with the experimentally observed Autler-Townes splittings. We used the values shown in table D. Note that there are no literature values to compare with, but the order of magnitude of the transition moments is typical. The ac Stark shift S varies proportional to the pump/control intensity, with a peak value approximated by the ponderomotive energy. We used the approximation $\hbar S = \phi$ for the pump-/control-induced shifts. We did not include ionization losses.

Table D: Parameters of the simulation for the seven control transitions.

transition	C1	C2	C3	C4	C5	C6	C7
wavelength [nm]	569.6	590.7	617.8	650.4	658.3	667.9	728
μ_{Ci} [10^{-30} Cm]	2	2	12	2	2	2	4

F Particle density/pressure dependence of frequency conversion

This appendix describes the particle density/pressure dependence of the frequency conversion signals in chapter 4 (CPR experiment) and shall demonstrate their coherent nature ($I_S \sim N^2 \sim p^2$). Note that we adjust in our experiments the stagnation pressure of the gas nozzle (section 2.2), which increases the particle density in the interaction region linearly [64]. The pressure dependence of the THG/SFG/FID-SHG signals is shown in Fig. F. We observe similar shapes for all three signals, which demonstrates the coherent properties of the FID-SHG. Up to a stagnation pressure of 200 mbar the signal intensity rises quadratically. For higher pressures, the signal intensity starts to saturate. This effect happens simultaneously for all three signals (and different signal wavelength), which indicates that this saturation is not due to phase mismatch.

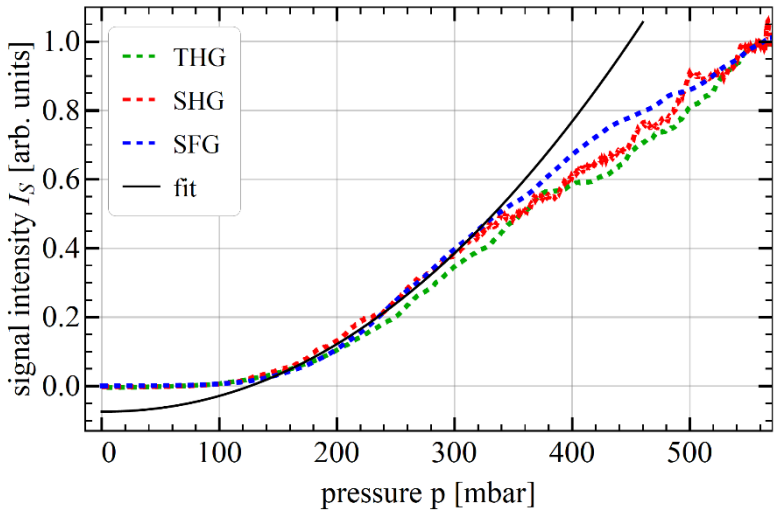

Figure F: Frequency conversion signal intensities versus stagnation pressure (experiments of chapter 4). We allowed a negative offset for the fit because of the threshold of the VUV detection.

Bibliography

1. C. Wagner and N. Harned, "EUV lithography: Lithography gets extreme," Nat. Photonics **4**, 24–26 (2010).
2. H. J. Eichler and J. Eichler, *Laser* (Springer, 2015).
3. F. Krausz and M. Ivanov, "Attosecond physics," Rev. Mod. Phys. **81**, 163–234 (2009).
4. T. Brabec and F. Krausz, "Intense few-cycle laser fields : Frontiers of nonlinear optics," Rev. Sci. Instrum. **72**, 545–591 (2000).
5. P. Rupper and F. Merkt, "Intense narrow-bandwidth extreme ultraviolet laser system tunable up to 20 eV," Rev. Sci. Instrum. **75**, 613–622 (2004).
6. C.-Y. Ng, "Vacuum ultraviolet spectroscopy and chemistry by photoionization and photoelectron methods," Annu. Rev. Phys. Chem. **53**, 101–140 (2002).
7. C.-Y. Ng, "State-to-state spectroscopy and dynamics of ions and neutrals by photoionization and photoelectron methods," Annu. Rev. Phys. Chem. **65**, 197–224 (2014).
8. S. Svanberg, *Atomic and Molecular Spectroscopy*, Springer Series on Atomic, Optical, and Plasma Physics (Springer, 2001).
9. U. Becker and D. A. Shirley, eds., *VUV and Soft X-Ray Photoionization* (Plenum Press, 1996).
10. E. L. Saldin, E. A. Schneidmiller, and M. V. Yurkov, *The Physics of Free Electron Lasers*, Advanced Texts in Physics (Springer, 2000).
11. P. Schmüser, M. Dohlus, and J. Rossbach, *Ultraviolet and Soft X-Ray Free-Electron Lasers*, Springer Tracts in Modern Physics (Springer, 2009).
12. W. Jamroz and B. P. Stoicheff, "Generation of tunable coherent vacuum-ultraviolet radiation," in *Progress in Optics*, E. Wolf, ed. (Elsevier, 1983).
13. J. F. Reintjes, *Nonlinear Optical Parametric Processes in Liquids and Gases* (Academic Press, 1984).
14. R. W. Boyd, *Nonlinear Optics* (Academic Press, 2008).
15. W. Demtröder, *Laser Spectroscopy 1: Basic Principles* (Springer, 2014).
16. T. Rickes, J. P. Marangos, and T. Halfmann, "Enhancement of third-harmonic generation by Stark-chirped rapid adiabatic passage," Opt. Commun. **227**, 133–142 (2003).
17. M. Fleischhauer, A. Imamoglu, and J. P. Marangos, "Electromagnetically induced transparency: Optics in coherent media," Rev. Mod. Phys. **77**, 633–673 (2005).
18. S. Chakrabarti, H. Münch, and T. Halfmann, "Adiabatically driven frequency conversion towards short extreme-ultraviolet radiation pulses," Phys. Rev. A **82**, 063817 (2010).
19. K. Midorikawa, "High-order harmonic generation and attosecond science," Jpn. J. Appl. Phys. **50**, 090001 (2011).
20. L. V. Keldysh, "Ionization in the field of a strong electromagnetic wave," Sov. Phys. JETP **20**, 1307–1314 (1965).
21. M. Wegener, *Extreme Nonlinear Optics* (Springer, 2005).

22. P. Ackermann, H. Münch, and T. Halfmann, "Resonantly-enhanced harmonic generation in argon," Opt. Express **20**, 13824 (2012).
23. P. Ackermann, "Efficient frequency conversion towards ultrashort VUV pulses using coherent control and multi-photon resonances," Ph.D. thesis, Technische Universität Darmstadt (2019).
24. P. Ackermann, A. Scharf, and T. Halfmann, "Strong quantum interferences in frequency up-conversion towards short vacuum-ultraviolet radiation pulses," Phys. Rev. A - At. Mol. Opt. Phys. **89**, (2014).
25. M. Förster, T. Paschen, M. Krüger, C. Lemell, G. Wachter, F. Libisch, T. Madlener, J. Burgdörfer, and P. Hommelhoff, "Two-color coherent control of femtosecond above-threshold photoemission from a Tungsten nanotip," Phys. Rev. Lett. **117**, 1–6 (2016).
26. S. H. Autler and C. H. Townes, "Stark effect in rapidly varying fields," Phys. Rev. **100**, 703–722 (1955).
27. S. P. Tewari and G. S. Agarwal, "Control of phase matching and nonlinear generation in dense media by resonant fields," Phys. Rev. Lett. **56**, 1811–1814 (1986).
28. J. C. Miller, R. N. Compton, and C. D. Cooper, "Vacuum ultraviolet spectroscopy of molecules using third-harmonic generation in rare gases," J. Chem. Phys. **76**, 3967–3973 (1982).
29. S. Camp, K. J. Schafer, and M. B. Gaarde, "Interplay between resonant enhancement and quantum path dynamics in harmonic generation in helium," Phys. Rev. A **92**, 1–8 (2015).
30. J. P. Marangos and T. Halfmann, "Electromagnetically induced transparency," in *Handbook of Optics*, E. W. Van Stryland and McGraw-Hill, eds. (OSA, 2009).
31. M. Jain, H. Xia, G. Y. Yin, A. J. Merriam, and S. E. Harris, "Efficient nonlinear frequency conversion with maximal atomic coherence," Phys. Rev. Lett. **77**, 4326–4329 (1996).
32. S. E. Harris, G. Y. Yin, M. Jain, H. Xia, and A. J. Merriam, "Nonlinear optics at maximum coherence," Philos. Trans. R. Soc. London A **355**, 2291–2304 (1997).
33. T. Halfmann, "Enhanced frequency conversion in coherently prepared media," in *Recent Research Activities in Chemical Physics: From Atomic Scale to Macroscale*, A. F. Terzis and E. Paspalakis, eds. (Research Signpost, 2009).
34. B. W. Shore, *The Theory of Coherent Atomic Excitation* (Wiley, 1990).
35. B. Shore, "Atoms affecting fields," in *Manipulating Quantum Structures Using Laser Pulses* (Cambridge University Press, 2011), pp. 387–418.
36. V. G. Arkhipkin and A. K. Popov, "Reviews of topical problems: Nonlinear optics and transformation of light in gases," Sov. Phys. Uspekhi **30**, 952–976 (1987).
37. A. Bonch-Bruevich and V. Khodovoi, "Current Methods for the Study of the Stark Effect in Atoms," Sov. Phys. Uspekhi **10**, 637–657 (1968).
38. P. F. Liao and J. E. Bjorkholm, "Direct observation of atomic energy level shifts in two-photon absorption," Phys. Rev. Lett. **34**, 1–4 (1975).

39. N. B. Delone and V. P. Krainov, "AC Stark shift of atomic energy levels," Physics-Uspekhi **42**, 669 (1999).
40. L. Pan, L. Armstrong, and J. H. Eberly, "Comments on the effect of the ponderomotive potential in the above-threshold ionization processes," J. Opt. Soc. Am. B **3**, 1319 (1986).
41. P. Ackermann, X. Laforgue, M. Hilbig, M. Schilder, and T. Halfmann, "Phase-matched harmonic generation in gas-filled waveguides in the vicinity of a multiphoton resonance," J. Opt. Soc. Am. B **35**, 468 (2018).
42. F. Cipura and T. Halfmann, "Resonantly enhanced harmonic generation via dressed states with large Autler–Townes splittings," J. Opt. Soc. Am. B **36**, 2777 (2019).
43. T. M. Albrecht, "Development of a three-channel autocorrelator for ps laserpulses," Bachelor thesis, Technische Universität Darmstadt (2014).
44. F. Cipura, "Regenerative amplification of chirped picosecond laser pulses," Master thesis, Technische Universität Darmstadt (2016).
45. D. Strickland and G. Mourou, "Compression of amplified chirped optical pulses," Opt. Commun. **55**, 447–449 (1985).
46. S. Backus, C. G. Durfee, M. M. Murnane, and H. C. Kapteyn, "High power ultrafast lasers," Rev. Sci. Instrum. **69**, 1207 (1998).
47. G. Cerullo and S. De Silvestri, "Ultrafast optical parametric amplifiers," Rev. Sci. Instrum. **74**, 1–18 (2003).
48. A. Vaupel, N. Bodnar, B. Webb, L. Shah, and M. Richardson, "Concepts, performance review, and prospects of table-top, few-cycle optical parametric chirped-pulse amplification," Opt. Eng. **53**, 051507 (2013).
49. P. Wnuk, Y. Stepanenko, and C. Radzewicz, "Multi-terawatt chirped pulse optical parametric amplifier with a time-shear power amplification stage," Opt. Express **17**, 15264 (2009).
50. P. Wnuk, Y. Stepanenko, and C. Radzewicz, "High gain broadband amplification of ultraviolet pulses in optical parametric chirped pulse amplifier," Opt. Express **18**, 7911 (2010).
51. L. Glebov, V. Smirnov, E. Rotari, I. Cohanoschi, L. Glebova, O. Smolski, J. Lumeau, C. Lantigua, and A. Glebov, "Volume-chirped Bragg gratings: monolithic components for stretching and compression of ultrashort laser pulses," Opt. Eng. **53**, 051514 (2014).
52. K. H. Liao, M. Y. Cheng, E. Flecher, V. I. Smirnov, L. B. Glebov, and A. Galvanauskas, "Large-aperture chirped volume Bragg grating based fiber CPA system," Opt. Express **15**, 4876–4882 (2007).
53. K.-H. Hong, A. Siddiqui, J. Moses, J. Gopinath, J. Hybl, F. Ö. Ilday, T. Y. Fan, and F. X. Kärtner, "Generation of 287 W, 5.5 ps pulses at 78 MHz repetition rate from a cryogenically cooled Yb:YAG amplifier seeded by a fiber chirped-pulse amplification system," Opt. Lett. **33**, 2473 (2008).
54. C. P. João, F. Wagner, J. Körner, J. Hein, T. Gottschall, J. Limpert, and V. Bagnoud, "A 10-mJ-level compact CPA system based on Yb:KGW for ultrafast optical parametric amplifier pumping," Appl. Phys. B **118**, 401–407 (2015).

55. M. Hemmer, D. Sánchez, M. Jelínek, V. Smirnov, H. Jelinkova, V. Kubecek, and J. Biegert, "2-μm wavelength, high-energy Ho:YLF chirped-pulse amplifier for mid-infrared OPCPA," Opt. Lett. **40**, 451–454 (2015).
56. P. Ackermann, "High order harmonic generation by laser pulses in the green spectral regime," Master thesis, Technische Universität Darmstadt (2011).
57. S. Reinisch, "Compensation of AC Stark shifts for resonant frequency conversion in rare gases," Master thesis, Technische Universität Darmstadt (2018).
58. B. P. Schallmo, "Optical parametric amplification of picosecond laser pulses in the visible spectrum," Bachelor thesis, Technische Universität Darmstadt (2017).
59. G. Cerullo and S. De Silvestri, "Ultrafast optical parametric amplifiers," Rev. Sci. Instrum. **74**, 1–18 (2003).
60. R. Trebino, K. W. DeLong, D. N. Fittinghoff, J. N. Sweetser, M. A. Krumbügel, B. A. Richman, and D. J. Kane, "Measuring ultrashort laser pulses in the time-frequency domain using frequency-resolved optical gating," Rev. Sci. Instrum. **68**, 3277 (1997).
61. R. Trebino, *Frequency-Resolved Optical Gating: The Measurement of Ultrashort Laser Pulses* (2000).
62. J. Bachmann, "Setup of a pulse chirper for ultra-fast coherent excitations," Master thesis, Technische Universität Darmstadt (2013).
63. S. Link, "Characterisation of picosecond laser pulses by means of a FROG-Algorithm," Bachelor thesis, Technische Universität Darmstadt (2015).
64. T. Adachi, K. Kondo, and S. Watanabe, "Gas density measurement of pulsed gas jets using XeF four-photon fluorescence induced by a KrF laser," Appl. Phys. B **55**, 323–326 (1992).
65. T. Ditmire, T. Donnelly, A. M. Rubenchik, R. W. Falcone, and M. D. Perry, "Interaction of intense laser pulses with atomic clusters," Phys. Rev. A **53**, 3379–3402 (1996).
66. N. Neumann, "Investigations on adiabatic frequency conversion towards the XUV spectral regime," Master thesis, Technische Universität Darmstadt (2014).
67. T. Namioka, "Theory of the concave grating III Seya-Namioka monochromator," J. Opt. Soc. Am. **49**, 951 (1959).
68. R. R. Freeman, P. H. Bucksbaum, H. Milchberg, S. Darack, D. Schumacher, and M. E. Geusic, "Above-threshold ionization with subpicosecond laser pulses," Phys. Rev. Lett. **59**, 1092–1095 (1987).
69. P. Agostini, A. Antonetti, P. Breger, M. Crance, A. Migus, H. G. Muller, and G. Petite, "Resonant multiphoton ionisation of xenon with high-intensity femtosecond pulses," J. Phys. B **22**, 1971–1977 (1989).
70. P. Agostini, P. Breger, A. L'Huillier, H. G. Muller, G. Petite, A. Antonetti, and A. Migus, "Giant Stark shifts in multiphoton ionization," Phys. Rev. Lett. **63**, 2208–2211 (1989).
71. M. B. Gaarde and K. J. Schafer, "Enhancement of many high-order harmonics via a single multiphoton resonance," Phys. Rev. A **64**, 013820 (2001).

72. C. F. de Morisson Faria, R. Kopold, W. Becker, and J. M. Rost, "Resonant enhancements of high-order harmonic generation," Phys. Rev. A **65**, 023404 (2002).
73. R. Taïeb, V. Véniard, J. Wassaf, and A. Maquet, "Roles of resonances and recollisions in strong-field atomic phenomena. II. High-order harmonic generation," Phys. Rev. A **68**, 033403 (2003).
74. E. S. Toma, P. Antoine, A. de Bohan, and H. G. Muller, "Resonance-enhanced high-harmonic generation," J. Phys. B At. Mol. Opt. Phys. **32**, 5843–5852 (1999).
75. M. Barkauskas, F. Brandi, F. Giammanco, D. Neshev, A. Pirri, and W. Ubachs, "A novel-type tunable and narrowband extreme ultraviolet radiation source based on high-harmonic conversion of picosecond laser pulses," J. Electron Spectros. Relat. Phenomena **144–147**, 1151–1155 (2005).
76. J. Rothhardt, S. Hädrich, S. Demmler, M. Krebs, S. Fritzsche, J. Limpert, and A. Tünnermann, "Enhancing the macroscopic yield of narrow-band high-order harmonic generation by Fano resonances," Phys. Rev. Lett. **112**, 233002 (2014).
77. V. Strelkov, "Role of autoionizing state in resonant high-order harmonic generation and attosecond pulse production," Phys. Rev. Lett. **104**, 123901 (2010).
78. M. A. Fareed, V. V. Strelkov, N. Thiré, S. Mondal, B. E. Schmidt, F. Légaré, and T. Ozaki, "High-order harmonic generation from the dressed autoionizing states," Nat. Commun. **8**, 16061 (2017).
79. V. V. Strelkov, "Attosecond-pulse production using resonantly enhanced high-order harmonics," Phys. Rev. A (2016).
80. M. A. Fareed, V. V. Strelkov, M. Singh, N. Thiré, S. Mondal, B. E. Schmidt, F. Légaré, and T. Ozaki, "Harmonic generation from neutral manganese atoms in the vicinity of the giant autoionization resonance," Phys. Rev. Lett. **121**, 023201 (2018).
81. R. A. Ganeev, M. Suzuki, M. Baba, H. Kuroda, and T. Ozaki, "Strong resonance enhancement of a single harmonic generated in the extreme ultraviolet range," Opt. Lett. **31**, 1699–1701 (2006).
82. R. A. Ganeev, *Resonance Enhancement in Laser-Produced Plasmas* (Wiley, 2018).
83. H. Wang, M. Chini, S. Chen, C. H. Zhang, F. He, Y. Cheng, Y. Wu, U. Thumm, and Z. Chang, "Attosecond time-resolved autoionization of argon," Phys. Rev. Lett. **105**, 3–6 (2010).
84. M. Wu, S. Chen, M. B. Gaarde, and K. J. Schafer, "Time-domain perspective on Autler-Townes splitting in attosecond transient absorption of laser-dressed helium atoms," Phys. Rev. A **88**, 043416 (2013).
85. M. Wu, S. Chen, S. Camp, K. J. Schafer, and M. B. Gaarde, "Theory of strong-field attosecond transient absorption," J. Phys. B At. Mol. Opt. Phys. **49**, (2016).
86. R. M. Whitley and C. R. Stroud, Jr., "Double optical resonance," Phys. Rev. A **14**, 1498 (1976).

87. N. V Vitanov, T. Halfmann, B. W. Shore, and K. Bergmann, "Laser-induced population transfer by adiabatic passage techniques," Annu. Rev. Phys. Chem. **52**, 763–809 (2001).
88. C. Wei, D. Suter, A. S. M. Windsor, and N. B. Manson, "ac Stark effect in a doubly driven three-level atom," Phys. Rev. A **58**, 2310–2318 (1998).
89. A. Kramida, Y. Ralchenko, J. Reader, and N. A. T. (2018), "NIST Atomic Spectra Database (version 5.6.1)," https://physics.nist.gov/asd [2019, April 23].
90. L. P. Yatsenko, T. Halfmann, B. W. Shore, and K. Bergmann, "Photoionization suppression by continuum coherence: Experiment and theory," Phys. Rev. A **59**, 2926–2947 (1999).
91. C. R. Vidal, "Coherent VUV sources for high resolution spectroscopy," Appl. Opt. **19**, 3897 (1980).
92. R. Hilbig, G. Hilber, A. Lago, B. Wolff, and R. Wallenstein, "Tunable coherent VUV radiation generated by nonlinear optical frequency conversion in gases," in *Nonlinear Optics and Applications*, P. Yeh, ed. (1986).
93. U. Hollenstein, H. Palm, and F. Merkt, "A broadly tunable extreme ultraviolet laser source with a 0.008/cm bandwidth," Rev. Sci. Instrum. **71**, 4023–4028 (2000).
94. H. Münch, "Coherent frequency conversion of ultra short laser pulses towards the VUV spectral range," Ph.D. thesis, Technische Universität Darmstadt (2010).
95. A. Chacón, M. F. Ciappina, and A. P. Conde, "High-order harmonic generation enhanced by coherent population return," Eur. Phys. J. D **69**, (2015).
96. N. V. Vitanov, B. W. Shore, L. Yatsenko, K. Böhmer, T. Halfmann, T. Rickes, and K. Bergmann, "Power broadening revisited: Theory and experiment," Opt. Commun. **199**, 117–126 (2001).
97. T. N. Chang and Y. S. Kim, "Photoionization from the excited p states of the rare-gas atoms," Phys. Rev. A **26**, 2728–2732 (1982).
98. O. Ernst, "Delayed frequency conversion via two-photon resonances in xenon," Bachelor thesis, Technische Universität Darmstadt (2019).
99. O. Kittelmann, J. Ringling, G. Korn, A. Nazarkin, and I. V. Hertel, "Generation of broadly tunable femtosecond vacuum-ultraviolet pulses," Opt. Lett. **21**, 1159 (1996).
100. G. Korn, O. Kittelmann, J. Ringling, A. Nazarkin, and I. V. Hertel, "Direct observation of coherent medium response under the condition of two-photon excitation of krypton by femtosecond UV-laser pulses," Springer Ser. Chem. Phys. **62**, 107–108 (1996).
101. A. Nazarkin, G. Korn, O. Kittelmann, J. Ringling, and I. V. Hertel, "Femtosecond-pulse two-photon resonant difference-frequency mixing in gases: A technique for tunable vacuum-ultraviolet femtosecond-pulse generation and a spectroscopic tool for studying atoms in strong laser fields," Phys. Rev. A **56**, 671–684 (1997).

102. R. O. Jung, J. B. Boffard, L. W. Anderson, and C. C. Lin, "Branching fractions and transition probabilities for levels of the 5p5 7p configuration of xenon," J. Quant. Spectrosc. Radiat. Transf. **110**, 1057–1065 (2009).
103. R. G. Brewer and R. L. Shoemaker, "Optical free induction decay," Phys. Rev. A **6**, 2001–2007 (1972).
104. F. A. Hopf, R. F. Shea, and M. O. Scully, "Theory of optical free-induction decay and two-photon superradiance," Phys. Rev. A **7**, 2105–2110 (1973).
105. J. H. Brownell, X. Lu, and S. R. Hartmann, "Time-delayed second harmonic generation," Phys. Rev. Lett. **75**, 3657–3660 (1995).
106. D. Kim, C. S. Mullin, and Y. R. Shen, "Second-harmonic generation in potassium vapor with picosecond laser pulses," J. Opt. Soc. Am. B **14**, 2530 (1997).
107. S. Bengtsson, E. W. Larsen, D. Kroon, S. Camp, M. Miranda, C. L. Arnold, A. L'Huillier, K. J. Schafer, M. B. Gaarde, L. Rippe, and J. Mauritsson, "Space-time control of free induction decay in the extreme ultraviolet," Nat. Photonics **11**, 252–258 (2017).
108. P. L. Knight, M. A. Lauder, and B. J. Dalton, "Laser-induced continuum structure," Phys. Rep. (1990).
109. A. Heinrich, M. Bruck, C. P. Hauri, W. Kornelis, J. W. G. Tisch, J. Biegert, and U. Keller, "Gas target for efficient high-harmonic generation," Conf. Lasers Electro-Optics/International Quantum Electron. Conf. Photonic Appl. Syst. Technol. **97**, 479–480 (2004).
110. C. P. Hauri, G. Sansone, E. Benedetti, and M. Nisoli, "Novel gas targets for efficient high-harmonic generation and more energetic attosecond pulse generation," Conf. Lasers Electro-Optics/Quantum Electron. Laser Sci. Conf. Photonic Appl. Syst. Technol. 9–10 (2008).
111. R. Zeißler, "Modifcation of a gas jet for efficient harmonic generation of ultra short light pulses," Bachelor thesis, Technische Universität Darmstadt (2018).

Publications and contributions to conferences

Publications in peer-reviewed journals

- F. Cipura, T. Halfmann:
  Resonantly enhanced harmonic generation via dressed states with large Autler-Townes splittings
  Journal of the Optical Society of America B 36 (10), 2777-2784 (2019)

Manuscripts in preperation

- F. Cipura, P.Ackermann, T. Halfmann:
  Frequency upconversion of intense, ultrashort laser pulses at maximal atomic coherence
  Submitted to Physical Review A

- F. Cipura, P.Ackermann, T. Halfmann:
  Compact, tunable amplifier for picosecond laser pulses at 800 nm with a chirped volume Bragg grating based stretcher and compressor

Talks at international conferences

- F. Cipura, T. Halfmann:
  Resonantly enhanced harmonic generation via dressed states with large Autler-Townes splittings
  15th International Workshop on Control of Quantum Dynamics of Atoms, Molecules and Ensembles by Light (CAMEL XV) – Nessebar, Bulgaria, June 2019

- F. Cipura, T. Halfmann:
  Resonantly enhanced harmonic generation via dressed states with large Autler-Townes splittings
  HICONO 2019 – ICFO, Castelldefels (Barcelona), Spain, September 2019

Supervisions and contributions to teaching

Master's thesis

- Simon Reinisch, Kompensation dynamischer Stark-Verschiebungen bei der resonanten Frequenzkonversion in Edelgasen, TU Darmstadt, 2018

Bachelor's thesis

- Benedikt Schallmo, Optisch parametrische Verstärkung von ps-Laserpulsen im sichtbaren Spektralbereich, TU Darmstadt, 2017

- Rolf Zeißler, Modifikation einer Gasdüse zur effizienten Frequenzkonversion ultrakurzer Lichtpulse, TU Darmstadt, 2018

- Oskar Ernst, Verzögerte Frequenzkonversion über Zwei-Photonen Resonanzen in Xenon, TU Darmstadt, 2019

Internships and laboratory courses

- Supervision of laboratory internship „Miniforschung“
    - Marietta Coelle, Aufbau und Charakterisierung eines Autokorrelators zur Messung von Pikosekunden-Laserpulsen, TU Darmstadt, 2019
- Supervision of the basic lab course in optics, “Diffraction”, “Polarization and birefringence”, “Michelson interferometer” and “Optical spectral analysis” (04/2017 - 7/2019)

Contributions to teaching

- Supervision of the talk “Injection seeding” in the seminar “Laserphysik & Lasertechnologie”, SS2020
- Labtours 2016-2020

Erklärung gemäß §9 Promotionsordnung

Hiermit versichere ich, dass ich die vorliegende Dissertation selbstständig angefertigt und keine anderen als die angegebenen Quellen und Hilfsmittel verwendet habe. Alle wörtlichen und paraphrasierten Zitate wurden angemessen kenntlich gemacht. Die Arbeit hat bisher noch nicht zu Prüfungszwecken gedient.

Darmstadt, den 15. Juni 2020

_____
(Fabian Cipura)